

Master Thesis, Department of Geosciences

# High resolution glacier dynamics from GNSS measurements on Holtedahlfonna, NW Svalbard

Kenneth Bahr



**UNIVERSITY OF OSLO**

**FACULTY OF MATHEMATICS AND NATURAL SCIENCES**



# High resolution glacier dynamics from GNSS measurements on Holtedahlfonna, NW Svalbard

Kenneth Bahr



Master Thesis in Geosciences

Discipline: Physical Geography, Hydrology and Geomatics

Department of Geosciences

Faculty of Mathematics and Natural Sciences

University of Oslo

December 1, 2015

© **Kenneth Bahr, 2015**

Supervisors: Christopher Nuth (UiO), Thomas V. Schuler (UiO), Halfdan Kierulf (UiO/Statens Kartverk), Jack Kohler (NPI)

This work is published digitally through DUO – Digitale Utgivelser ved UiO

<http://www.duo.uio.no>

It is also catalogued in BIBSYS (<http://www.bibsys.no/english>)

All rights reserved. No part of this publication may be reproduced or transmitted, in any form or by any means, without permission.

Cover picture: GNSS station on Høltedahlfonna, taken in spring 2015.

## Acknowledgements

I would like to thank my supervisors Christopher Nuth, Halfdan Kierulf, Jack Kohler and Thomas Schuler for all your support! You have all been more than helpful!

I also need to thank Jack Kohler and Ward Van Pelt for providing data for this thesis. I am also grateful for the Arctic Field Grant from the Research Council of Norway.

Thank you for introducing me to Ny-Ålesund, Chris! The fieldwork on Holtedahlfonna was never boring, and I hope I will go back one day! With you, Ankit, Ward, Halfdan and Jack as field companions, it was a pleasure!

To all my friends at the geoscience department, thanks for the good memories! A special thanks to you Amund for helping me with proofreading!

To the rest of you, thank you!

## Abstract

The motion of temperate and polythermal glaciers is influenced by the seasonal input of meltwater to the basal hydrological system. Spatial differences in the bed sliding velocities lead to stress and strain in the glacier ice, and the related changes can be measured on the glacier surface. This study analyzes the motion of three Global Navigation Satellite System (GNSS) stations installed on the glacier surface of Høltedalsfonna over the period September 1<sup>st</sup> 2014 – August 31<sup>st</sup> 2015. In order to detect the small-scale changes on the glacier surface, the error sources affecting the GNSS positioning need to be reduced or eliminated. By comparing precise point positioning (PPP) and different setups of relative positioning, this study finds that a network setup with kinematic relative positioning has the best combination of precision and ability to capture the short-term changes of the glacier. The approximated uncertainties for each estimated position on the glacier was  $\pm 18$  mm and  $\pm 69$  mm (95% confidence level) in the horizontal and vertical directions, respectively.

The observations during winter reveals surface velocities in the range of 0.12 - 0.28 m/day. By estimating the runoff with a surface mass balance model, the influence of meltwater on the glacier motion is evaluated during the summer season. Two major events of increasing horizontal and vertical motion is evident at all three stations, and coincides with significant increases in the estimated runoff. A prominent supraglacial lake is identified on optical satellite images and its volume is estimated from a digital elevation model (DEM). The drainage of the lake occurs in the same period as rapid uplift, increasing surface velocities and horizontal translation can be observed at all three stations. The middle and lower GNSS station sustains elevated vertical positions over a two-week period after the first major event, and this indicates local storage of water at the glacier bed. During the two major events, significant variations in the longitudinal strain was observed, with both compression and extension between the three stations. Changes in elevation due to vertical strain and rates of bed separation are estimated, but the absolute magnitude of these values are uncertain. Although the complexity of glacier dynamics gives a range of uncertainties, this study has shown the potential of high resolution GNSS for these applications.

## Table of Contents

<b>Acknowledgements .....</b>	<b>v</b>
<b>Abstract.....</b>	<b>vi</b>
<b>List of Figures.....</b>	<b>ix</b>
<b>List of Tables .....</b>	<b>xi</b>
<b>Abbreviations .....</b>	<b>xii</b>
<b>1 Introduction .....</b>	<b>1</b>
1.1 Objectives.....	3
<b>2 Study area.....</b>	<b>4</b>
<b>3 Background and theory .....</b>	<b>8</b>
3.1 GNSS.....	8
3.1.1 Error sources .....	9
3.1.2 Precise point positioning .....	10
3.1.3 Relative positioning .....	12
3.1.4 Satellite constellation and coverage.....	13
3.2 Glacier motion and dynamics .....	15
3.3 Glacier hydrology and surface mass balance .....	18
<b>4 Methods .....</b>	<b>20</b>
4.1 Fieldwork .....	20
4.2 GNSS post-processing .....	22
4.2.1 Software.....	23
4.2.2 Static positioning.....	24
4.2.3 Pseudo-static positioning.....	24
4.2.4 Kinematic positioning.....	25
4.2.5 Reference frames and coordinate system conversion.....	27
4.3 Glaciological computations .....	28
4.3.1 Deformation and bed sliding velocity.....	29
4.3.2 Strain rate .....	31

4.3.3	Bed separation .....	32
4.3.4	Glacier runoff.....	33
4.3.5	Identification and quantification of supraglacial lake.....	34
4.4	Statistics and uncertainty .....	35
5	Results.....	37
5.1	Comparison of GPS/GNSS post-processing methods and software .....	37
5.1.1	Pseudo-static.....	38
5.1.2	Kinematic .....	40
5.2	Glacier motion.....	43
5.2.1	Winter and summer season 2015 .....	45
5.2.2	Summer season 2015.....	47
5.2.3	Phase 1 .....	51
5.2.4	Phase 2.....	53
5.2.5	Supraglacial meltwater and lake drainage .....	55
6	Discussion.....	58
6.1	GNSS setup and post-processing results .....	58
6.2	Glaciological interpretation.....	61
7	Conclusions.....	67
8	References.....	69
9	Appendices.....	I
9.1	Runoff calculation .....	I
9.2	Coordinate of HAGN base station with static processing.....	I
9.3	Kinematic field survey.....	II



## List of Figures

Figure 2.1. Overview of the study area.....	4
Figure 2.2. Holtedahlfonna and Kronebreen.....	5
Figure 2.3. Daily average air temperature from HDF2 AWS.....	7
Figure 3.1. Point positioning of a single receiver using carrier phase measurements.....	11
Figure 3.2. Illustration of relative positioning.....	13
Figure 3.3. Skyplot of the available GPS and GLONASS satellites.....	14
Figure 3.4. Combined plot of the number of available satellites and GDOP .....	15
Figure 4.1. Overview of the general setup of all the GNSS stations.....	20
Figure 4.2. Pictures of setup of GNSS stations.....	21
Figure 4.3. Vertical profile of lateral transect at HDF2 .....	30
Figure 4.4. Elevations above HDF1 on Holtedahlfonna (DEM) .....	34
Figure 5.1. Combined plot of the pseudo-static positions.....	39
Figure 5.2. Running standard deviation and mean running standard deviation .....	40
Figure 5.3. Combined plot of kinematic positions.....	41
Figure 5.4. HAGN kinematic solution .....	42
Figure 5.5. Standard deviations for discrete intervals.....	43
Figure 5.6. Vertical positions for TRACK and RTKLIB .....	44
Figure 5.7. Sensitivity analysis for deformation velocities at HDF2 .....	45
Figure 5.8. Combined plot of the glacier motion, temperature, precipitation and estimated cumulative runoff, between September 2014 – September 2015. ....	46
Figure 5.9. A combined plot for the summer season data.....	48
Figure 5.10. Original bed separation .....	50
Figure 5.11. Phase 1 .....	52
Figure 5.12. Phase 2.....	54
Figure 5.13. Landsat 8 scenes.....	55

Figure 5.14. Histograms of elevation values along the lake outlines.....	56
Figure 5.15. Bed topography of Holtedahlfonna .....	57
Figure 9.1. Horizontal track of the kinematic field survey .....	II
Figure 9.2. Snow depth measurements .....	II

## List of Tables

Table 2.1. Linear trends in temperature and precipitation over the period 1975-2011, for Ny-Ålesund (Førland et al., 2012).....	6
Table 3.1. Overview of the most common error sources for GNSS positioning. The table is based on Hofmann-Wellenhof et al. (2008).....	10
Table 4.1. GNSS stations in the period September 1 <sup>st</sup> 2014 – August 31 <sup>st</sup> 2015. NYAL and NYA1 are the official IGS names for these two stations. The GNSS stations on the glacier were limited to two hours of daily observations between September 2014-April 2015.....	22
Table 4.2. The different combinations of relative positioning conducted in TRACK.....	26
Table 5.1. Cartesian coordinates of HAGN .....	37
Table 5.2. The estimated uncertainties for running average filtered position time-series at given time intervals. ....	43
Table 5.3. Estimates of the volume of the supraglacial lake on July 9 <sup>th</sup> and 10 <sup>th</sup> . The different volume estimates relate to the different elevation values from the DEM along the lake outlines. ....	56

## Abbreviations

AWS	Automatic weather station
CSRS PPP	The Canadian Spatial Reference System Precise Point Positioning
DEM	Digital elevation model
DOP	Dilution of precision
DOY	Day of year
ELA	Equilibrium line altitude
GAMIT	GPS post-processing software package for relative static positioning
GDOP	Geometric dilution of precision
GIS	Geographic information system
GLIMS	Global Land Ice Measurements from Space
GLONASS	Global'naya Navigatsionnaya Sputnikovaya Sistema
GNSS	Global navigation satellite system
GPR	Ground-penetrating radar
GPS	Global positioning system
HAGN	GNSS station located on a nunatak at the glacier Kongsvegen
HDF1/2/3	GNSS stations located on the glacier Holtedahlfonna
IGS	The International GNSS service
ITRF	The International Terrestrial Reference Frame
L1+L2	L1 and L2 frequency bands treated as independent observables
LC	Linear combination of the L1 and L2 frequency bands
NPI	Norwegian Polar Institute
NYA1	Permanent GNSS station located in Ny-Ålesund
NYAL	Permanent GNSS station located in Ny-Ålesund
NEU	Northing, easting, up
OTL	Ocean tide loading
PPP	Precise point positioning
RTKLIB	GNSS post-processing software

SNR	Signal-to-noise ratio
TRACK	GPS post-processing software package for relative kinematic positioning
UTM	Universal Transverse Mercator
XYZ	Cartesian coordinates

# 1 Introduction

Since the introduction of the Global Positioning System (GPS) during the 1980s (Hofmann-Wellenhof et al., 2008), the technology has gradually been implemented as one of the most important tools within the world of surveying. Over the last decades, the number of GPS satellites have increased, new satellite systems have been introduced and the technical equipment has developed and improved significantly. The current fully operational global satellite-based positioning systems, defined by the collective term global navigation satellite system (GNSS), include the American and Russian systems GPS and GLONASS, respectively (Hofmann-Wellenhof et al., 2008). With the support of current and future GNSS, the latest satellite receivers can utilize a large number of available satellites almost anywhere on the globe.

There are several sources of errors and biases that can degrade the precision of the estimated positions from a GNSS system. However, by applying techniques that reduce or eliminate the effect of these errors, the uncertainties can be significantly reduced down to the cm- and mm-level (Hofmann-Wellenhof et al., 2008). These techniques include relative positioning, using at least one base station at a fixed location as reference, and precise point positioning (PPP) of a single receiver. While relative positioning requires a minimum of two receivers with simultaneous observations to the same satellites, PPP only requires a single station, which can be a large logistical advantage and is sometimes the only option in remote areas and for certain applications (e.g. Kohler et al., 2013).

The use of GNSS positioning in glacier studies was incorporated shortly after the GPS technology was available to the public (e.g. Hinze and Seeber, 1988), and has replaced many of the traditional surveying techniques that were previously used (Battle, 1951; Iken et al., 1983; Hooke et al., 1989). While the traditional surveying techniques, e.g. using theodolites and geodimeters, offer high achievable accuracies, they are effortful when covering large areas over short time-intervals. The use of automatic theodolites reduces the need for human intervention and enables surveys of high temporal resolution, as seen in Sugiyama et al. (2008) and Anderson et al. (2004). However, with the current GNSS positioning techniques, it is possible to perform continuous observations of horizontal and vertical motion on large glaciers and ice sheets in remote areas with high temporal resolution and precision.

Field-based studies of glacier motion are often conducted by installing metal poles into the ice at certain locations on the glacier, and by surveying their positions at given time intervals (Cuffey and Paterson, 2010). These surveys can include the mass balance stakes along the center line of a

glacier, often performed in relation to the bi-annual mass balance measurements of a glacier, which yields the displacements of each stake over the course of the respective mass balance season (e.g. Van Pelt and Kohler, 2015). But in order to gain a deeper understanding of the dynamics related to the relative motion of different parts of the glacier during over shorter time scales, e.g. at daily, hourly or sub-hourly intervals during the summer melt season, simultaneous measurements at several locations with a higher temporal resolution is necessary.

Several studies have focused on glacier dynamics during the summer melt season, in regard to the horizontal and vertical displacements at different locations on a glacier, and their relation to each other. The link between changes in the glacier surface hydrology, basal lubrication and bed sliding is well documented (e.g. Willis, 1995; Zwally et al., 2002; Shepherd et al., 2009) and the effect of hydraulic jacking causing uplift has been observed at several glaciers (Iken et al., 1983; Anderson et al., 2004; Bartholomew et al., 2010). Changes in the surface elevation have not only been assigned to bed separation caused by the hydraulic jacking, but also to the effect of dynamic strain due to spatial differences in flow velocities (Anderson et al., 2004; Harper et al., 2007; Hoffman et al., 2011).

The meltwater production on the glacier surface during the summer season causes water to flow in supraglacial river networks, form supraglacial lakes or percolate into the surface firn layer where this is present (Cuffey and Paterson, 2010). Most of the surface water gets transported into the glacier through crevasses and moulins, and down to the basal hydrological system at warm-based glaciers (Cuffey and Paterson, 2010). The formation of supraglacial lakes leads to temporary storage of water that would otherwise continue to flow on the surface and later drain into the glacier. When these supraglacial lakes continue to grow in size, they can reach a point where lake starts draining supraglacially or down into the glacier through cracks and conduits and affect the glacier motion when the water reaches the subglacial hydrologic system, as seen in Das et al. (2008). The effect of these lake drainage events on the glacier motion is probably related to the size of the lakes and the condition of the subglacial drainage system, as indicated by Hoffman et al. (2011).

Many of the recent field-based studies of glacier dynamics use GNSS stations on the glacier to observe horizontal and vertical displacements on the glacier surface. Depending on the magnitude of the glacier motion, it is necessary to achieve a precision in the estimated position from the post-processing of the GNSS observations so that the displacements can be detected with statistical significance. If analyzing the horizontal surface velocity of a glacier flowing at 10 m/year, a high precision is necessary when measuring daily displacements, whereas a glacier

flowing at 1 m/day requires a less precision. King (2004) studied GPS post-processing strategies for glaciological applications, and compared the methods of kinematic and short-segment static processing for GPS observations on a moving glacier. The study found that systematic errors in the estimated positions under certain conditions have far greater magnitude than the error estimates given by the post-processing software, and emphasized how these biases can lead to erroneous estimates of horizontal surface velocities and elevation changes on a glacier.

## 1.1 Objectives

On the background of previous studies of glacier dynamics from GNSS observations and GNSS post-processing methods for glaciological applications, this thesis aims to apply these techniques for a study of the glacier dynamics on the Arctic glacier Høltedahlfonna in northwest Svalbard, with high temporal resolution and precision. The main objectives of this thesis are to:

- Find the optimal positioning technique for the GNSS observations gathered on the Arctic glacier Høltedahlfonna during 2014-2015. By comparing PPP and different setups of relative positioning, this thesis aims to find the positioning technique that can capture the small-scale variations of the moving glacier, both during the winter season and summer melt season, with the highest possible precision.
- Analyze the glacier dynamics of Høltedahlfonna using the observations from three GNSS stations on the glacier during 2014-2015 by applying the optimal post-processing technique. With continuous measurements from three GNSS stations during the summer season, the project aims to analyze the horizontal and vertical motion of each individual station, and the relative changes between the stations. Since the GNSS stations are located along the same flow line, the dynamics related to longitudinal strain will be analyzed. By using a surface mass balance model to estimate the melt-water production during summer, together with manual inspection of Landsat 8 satellite images, this study aims to analyze the influence of melt-water input on the glacier dynamics. The GNSS stations measure the motion of the glacier surface, but an important objective is to relate the observed surface motion to bed-parallel sliding and vertical bed separation.



## 2 Study area

The archipelago of Svalbard comprises four major islands, where Spitsbergen is the largest. Due to its location in the Arctic, with most of the land masses at latitudes ranging from 76.5-80.5°N, the archipelago has a climate favorable for the existence of glaciers and ice caps. While Nordaustlandet, the second largest island of the archipelago, is covered by the two large ice caps Austfonna and Vestfonna, Spitsbergen has several smaller marine- and land terminating glaciers. The glaciers and ice caps cover approximately 60% of Svalbard (König et al., 2014), and are thus dominating features in the landscape of this Arctic archipelago.

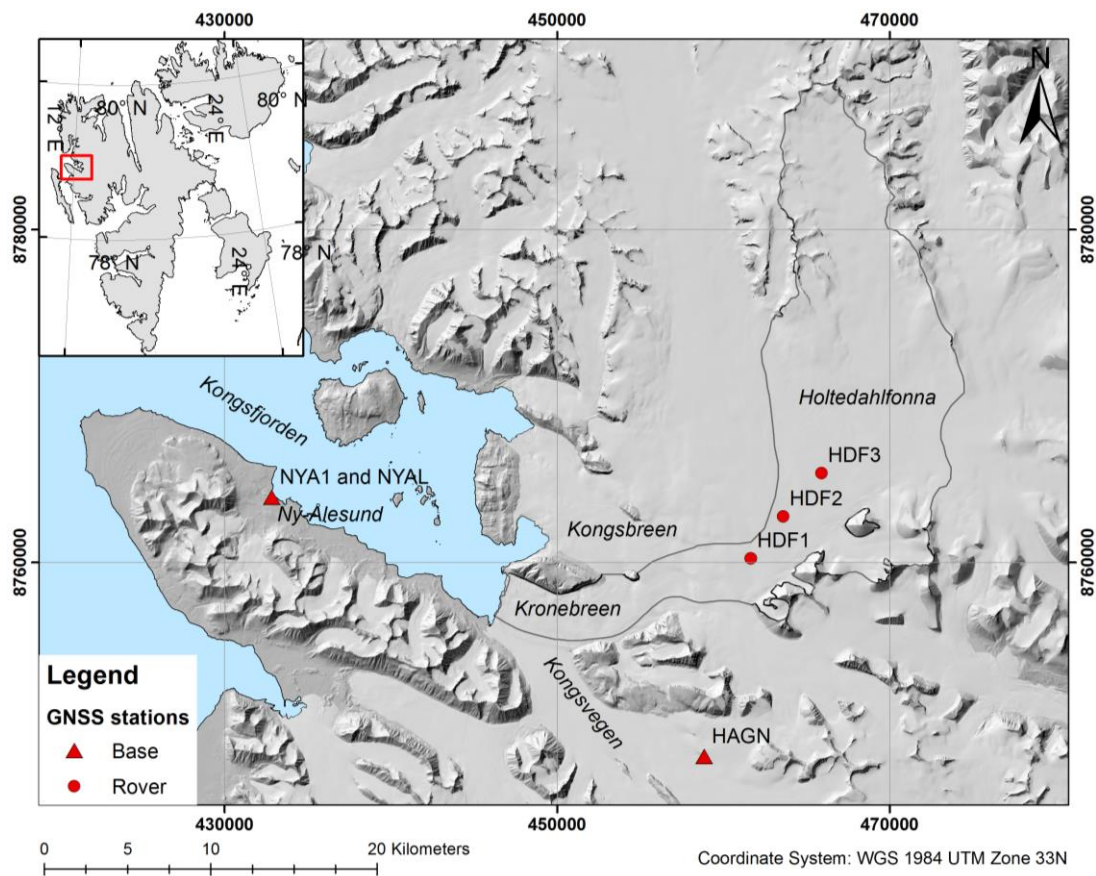


Figure 2.1. Overview of the study area. Holtedahlfonna is outlined in black, and the GNSS stations on the glacier (rovers) are marked with the red circles. An automatic weather station (AWS) is located at the middle station HDF2. The three GNSS base stations are marked with the red triangles. The HAGN station is located in a nunatak at Kongsvegen.

Holtedahlfonna is located on the northwest coast of Spitsbergen and lies within the drainage basin to Kongsfjorden (Svendsen et al., 2002) (Figure 2.1). Holtedahlfonna drains into Kronebreen, a highly crevassed, fast-flowing glacier terminating into Kongsfjorden, but the boundary between these two glaciers are (to the authors knowledge) not accurately defined. Although different naming and boundary definitions of the glacier can be observed in some of the previous studies from the area (Liestøl, 1988; Kääb et al., 2005; Nuth et al., 2012), this study

defines the boundaries of Høltedahlfonna/Kronebreen glacier system from the Global Land Ice Measurements from Space (GLIMS) glacier outline dataset (König et al., 2014), as seen in Nuth et al. (2012) and Van Pelt and Kohler (2015). The midpoint of Høltedahlfonna is located approximately 35 km and 100 km from Ny-Ålesund and Longyerbyen, respectively.

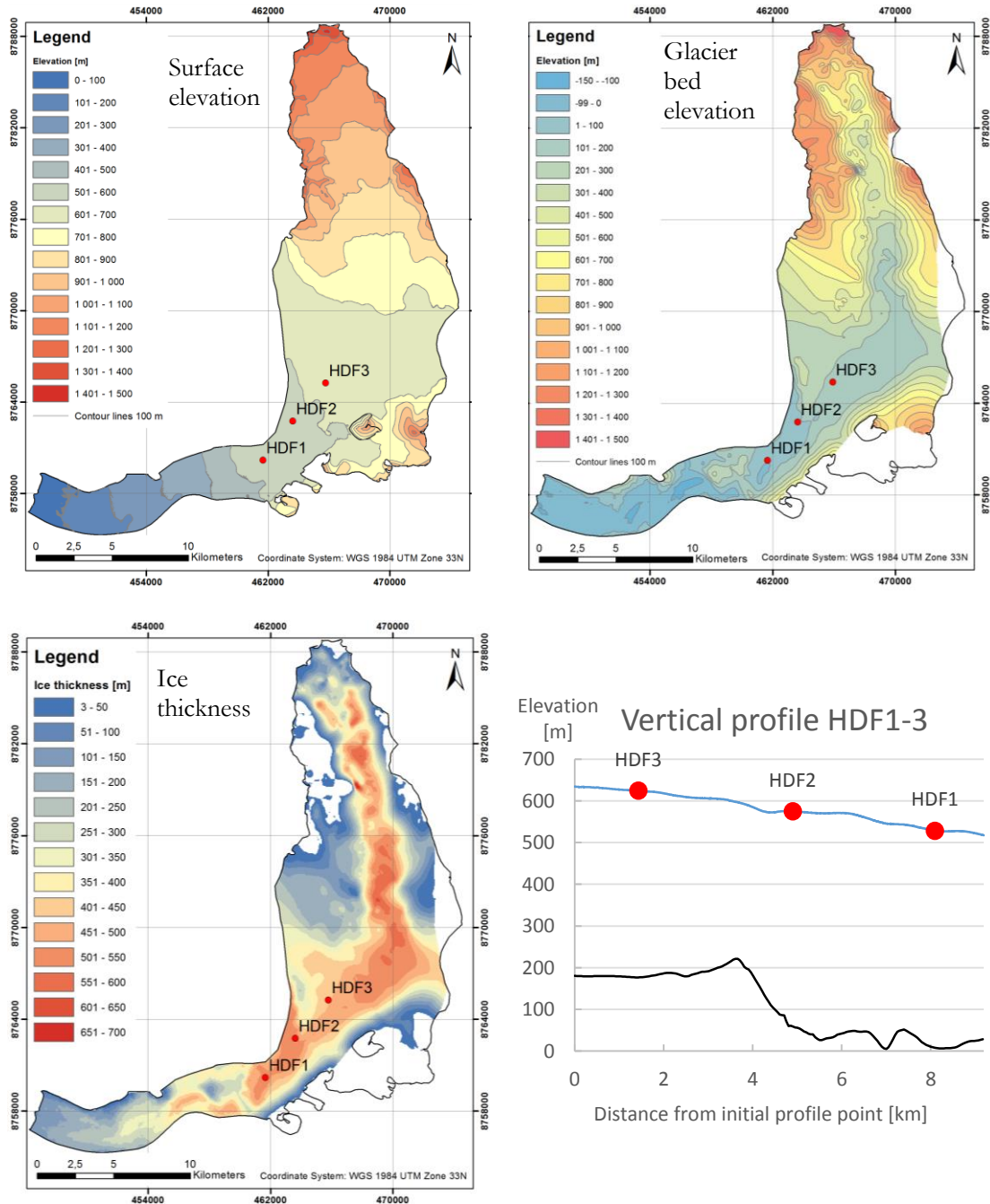


Figure 2.2. Høltedahlfonna and Kronebreen. **Upper left:** Elevation of the glacier surface, from DEM (NPI, 2009). **Upper right:** Elevation of the glacier bed topography, from ground penetrating radar (GPR) measurements (J. Kohler, unpublished data). **Lower left:** Ice thickness derived from glacier surface and bed topography. The areas in white are either missing data or have been masked if the elevation of the bed topography is higher than the glacier surface. The latter is probably due to sparse data and/or interpolation artifacts, and must be considered when evaluating the bed topography map. **Lower right:** Vertical profile of a transect between the stations HDF1-3. The glacier surface and bed topography are given with the blue and black, respectively.

Holtedahlfonna is classified as a sub-polar or polythermal glacier (Svendsen et al., 2002; Christianson et al., 2015) and covers an area of  $\sim 300 \text{ km}^2$  distributed over an elevation range of 0-1441 m a.s.l. (König et al., 2014; NPI, 2014). From ground penetrating radar (GPR) measurements (J. Kohler, unpublished data) and a digital elevation model (DEM) over the area (NPI, 2014), realistic thicknesses of up to  $\sim 650 \text{ m}$  can be derived (Figure 2.2). Kronebreen is a well-studied glacier, characterized by surface flow velocities of up to several meters per day (e.g. Lefauconnier et al., 1994; Kääb et al., 2005), large calving rates (Rolstad and Norland, 2009; Nuth et al., 2012) and significant retreat of the glacier front (Liestøl, 1988; Luckman et al., 2015). Less studies have been published on the motion of the upper parts of the glacier system, but the surface velocities of Holtedahlfonna have been analyzed using radar satellite images (Lefauconnier et al., 2001). The Norwegian Polar Institute (NPI) has conducted seasonal mass-balance observations on Holtedahlfonna since 2003 and on Kronebreen since 2008 (Van Pelt and Kohler, 2015), and bi-annual surface velocities have thus been derived at the locations of the mass balance stakes (J. Kohler, personal communication, 2015).

Table 2.1. Linear trends in temperature and precipitation over the period 1975-2011, for Ny-Ålesund (Førland et al., 2012).

Type	Annual	Winter	Spring	Summer	Autumn
Temperature [ $^{\circ}\text{C}/\text{decade}$ ]	0.73	1.36	0.60	0.33	0.53
Precipitation [ $\%/\text{decade}$ ]	5.4	15.6	-2.7	-5.1	10.9

Observations of temperature and precipitation have been conducted from the same meteorological station in Ny-Ålesund since 1975, and time series of temperature at separate sites go back to 1934 (Førland et al., 2012). For the periods 1961-1990 and 1981-2010, Førland et al. (2012) presents a mean annual air temperature for Ny-Ålesund of  $-6.3 \text{ }^{\circ}\text{C}$  and  $-5.2 \text{ }^{\circ}\text{C}$ , respectively. For the same periods, the mean annual precipitation was 385 mm and 427 mm, respectively. The largest increases in both temperature and precipitation were observed for the winter season, as illustrated by the linear trends for the period 1975-2011 in Table 2.1. The observed warming in Ny-Ålesund was not unique on the archipelago, and temperature series from all stations on Svalbard show similar values of increasing temperatures during the last decades (Førland et al., 2012).

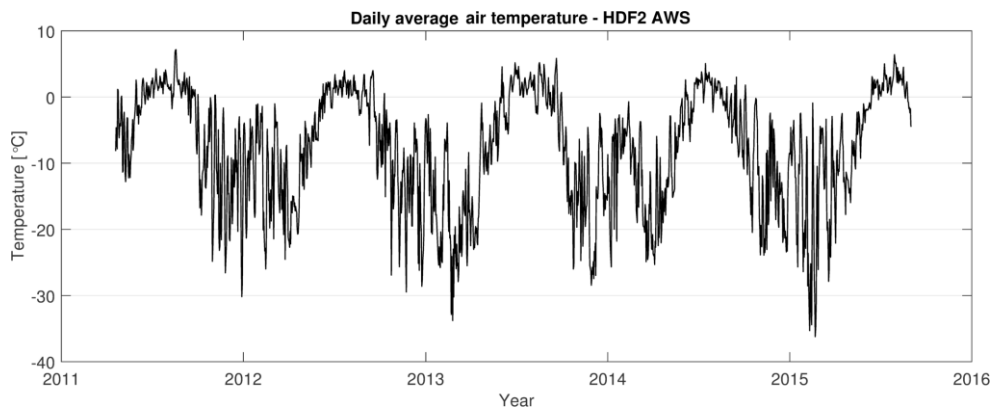


Figure 2.3. Daily average air temperature from an automatic weather station (AWS) located at stake HDF2 on Holtedahlfonna (J. Kohler, unpublished data). The plot illustrates large temperature fluctuations during winter, while the conditions during summer are more stable.

Since April 2011, an automatic weather station (AWS) have gathered a continuous record of meteorological observations at stake 2 (HDF2 in Figure 2.1) on Holtedahlfonna. The daily average air temperatures for the period 2011-2015 show significant variation in the winter temperatures, while the summer temperatures are more stable. This is similar to what is observed and discussed by Hanssen-Bauer et al. (1990) and Svendsen et al. (2002). The mentioned studies assign these fluctuations to the large differences in temperature between air masses of Arctic and Atlantic origin.

### 3 Background and theory

This chapter will go through some of the fundamentals of GNSS positioning, glacier dynamics and glacier hydrology, and will include relevant studies of these topics. Several studies, including this one, combine these three disciplines in their analyses, and it is thus advantageous to introduce some key principles, definitions and background theory of each individual discipline.

#### 3.1 GNSS

The complete theory behind satellite-based positioning is complex and thoroughly described in the literature, and it is beyond the scope of this thesis to cover all areas of the field. This section will go through some brief history and basic principles of GNSS positioning, error sources and how some of the related biases can be reduced or eliminated, as well as some key procedures and iterative routines for how post-processing software estimate the distance to each satellite.

The first launches of developmental GPS satellites began in 1978, but it was not until 1995 that full operational capability was declared (Hofmann-Wellenhof et al., 2008). The system was initially intended for the US military, but free civilian access was offered in 1983 (Hofmann-Wellenhof et al., 2008). The Russian counterpart to the American GPS system, “Global’naya Navigatsionnaya Sputnikovaya Sistema” (GLONASS), was introduced with the first launches of satellites in 1982 and was officially declared operational in 1993 (Hofmann-Wellenhof et al., 2008). GLONASS is operated by the Russian Military forces, but the navigation signals were offered to the public as early as 1988 (Hofmann-Wellenhof et al., 2008).

GNSS positioning is based on the general concept of trilateration, where location of an unknown point can be determined by simultaneous range measurements from three known sites (Manolakis, 1996). Since the positions of the GNSS satellites are known from orbital parameters, the time-dependent geometric distance  $\varrho_r^s(t)$  between each satellite  $s$  and the GNSS receiver  $r$  with an unknown position can be stated as

$$\varrho_r^s(t) = \sqrt{(X^s(t) - X_r)^2 + (Y^s(t) - Y_r)^2 + (Z^s(t) - Z_r)^2} \quad (3.1)$$

representing the earth-centered Cartesian coordinates of the satellites  $(X^s(t), Y^s(t), Z^s(t))$  and the receiver  $(X_r, Y_r, Z_r)$  (Hofmann-Wellenhof et al., 2008). Thus, with the true geometric distances, a total of three satellites would be sufficient for determining the position of a receiver. However, since clock biases affect the estimated distances, a minimum of four satellites is necessary, depending on the positioning method.

The transmitted navigation satellite signals are phase modulated electromagnetic waves consisting of a data-link-, ranging code- and physical layer (Hofmann-Wellenhof et al., 2008). The data-link layer contains e.g. the time of transmission and satellite ephemerides, while the ranging code layer describes a correlation technique for measuring the propagation time (Hofmann-Wellenhof et al., 2008). The distance between a satellite and a receiver can either be determined by using the code-based signal, simply by using the time of transmission, the propagation time and the speed of light, or by using the carrier phase signal. The latter technique estimates the total number of cycles of the carrier signal between the satellite and the receiver, and uses the known wavelength to convert this into distance. An integer number of cycles, called the phase ambiguity  $N$ , remains time-independent as the receivers make consecutive observations to the satellite (Figure 3.1). The integer ambiguity can be estimated through an iterative procedure during post-processing in order to estimate the range to the satellite. As we will see in the next section, several error sources bias these measured distances, and they are thus called code- and phase pseudoranges (Awange, 2012).

The satellites transmit carrier signals of different frequencies, and these are different for GPS and GLONASS. The GPS satellites transmit the navigation signals on the L1, L2 and L5 frequency bands with wavelengths of 19.0 cm, 24.4 cm and 25.5 cm, respectively, with individual ranging codes modulated on the different carrier frequencies (Hofmann-Wellenhof et al., 2008). GLONASS satellites transmit the navigation signals on the L1, L2 and L3 bands, but with non-constant frequencies for each band, yielding various wavelengths. Since each satellite is identified by the unique frequencies, common ranging codes are modulated on all the carrier frequencies, opposite to the GPS satellites (Hofmann-Wellenhof et al., 2008).

### **3.1.1 Error sources**

There are several error sources that cause range biases between a satellite and the receiver, and these can thus lead to significant uncertainties in the estimated positions (Table 3.1). The internal receiver clocks are less precise than the atomic clocks in the satellites, and their combined errors cause a time offset (Awange, 2012). Orbital errors lead to incorrect positions of the satellites, which are fundamental in the trilateration technique (3.1). When the signal propagates through the charged particles in ionosphere and the water vapor in the troposphere, it gets refracted and does not follow the straight-line path to the receiver, leading to a combined atmospheric delay of the signal (Awange, 2012).

Table 3.1. Overview of the most common error sources for GNSS positioning. The table is based on Hofmann-Wellenhof et al. (2008).

Source	Effect
Satellite	Clock bias
	Orbital errors
Signal propagation	Ionospheric refraction
	Tropospheric refraction
Receiver	Antenna phase center variation
	Clock bias
	Multipath

The electrical phase center of a GNSS antenna relates to the point of where the incoming signals are measured, and varies with several factors, including the frequency of the signal (Hofmann-Wellenhof et al., 2008). The mean position of these points is normally determined by the manufacturer and other agencies, and the estimated offsets can be corrected during GNSS post-processing. Multipath is the effect of the signal getting reflected at nearby objects and surfaces and thus following an indirect path to the receiver. This leads to incorrect ranges between the satellites and the receiver, and can cause significant errors in the estimated positions.

Ground stations track the positions and clock parameters of the satellites continuously, and precise orbital data and clock corrections are released by several agencies in the following hours or days, depending on the precision. With the final ephemerides, the accuracy of the orbital data is reduced from  $\sim 100$  cm to  $\sim 2.5$  cm for GPS satellites and  $\sim 3.0$  cm for GLONASS satellites (IGS, 2009).

### 3.1.2 Precise point positioning

When performing point positioning of a single receiver with carrier phase measurements, the geometric time-dependent distance  $\varrho_r^s(t)$  between the receiver  $r$  and a satellite  $s$  at a given epoch  $t$  can be stated by

$$\varrho_r^s(t) = N_r^s \lambda^s + \Delta\varphi_r^s(t) \lambda^s + c\Delta\delta_r^s(t) \quad (3.2)$$

representing the initial time-independent integer ambiguity expressed in cycles ( $N_r^s$ ), the fractional phase at epoch  $t$  expressed in cycles ( $\Delta\varphi_r^s(t)$ ), the wavelength of the carrier signal ( $\lambda^s$ ), the speed of light ( $c$ ) and combined satellite- and receiver clock bias  $\Delta\delta_r^s(t)$  (Figure 3.1) (Hofmann-Wellenhof et al., 2008).

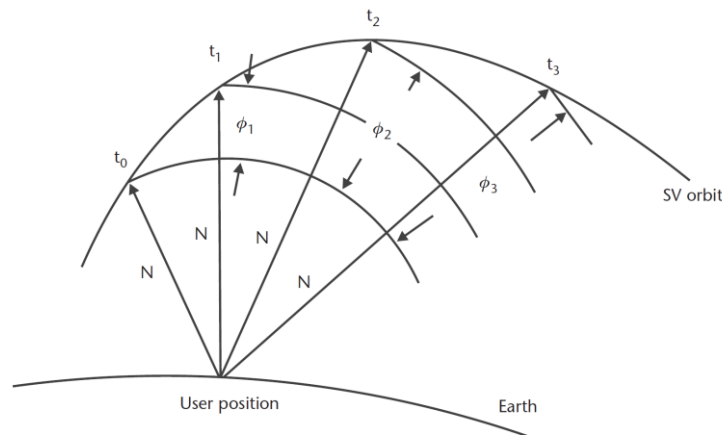


Figure 3.1. Point positioning of a single receiver using carrier phase measurements. The phase ambiguity  $N$  remains constant while the receiver makes observations to the satellite at following epochs. Figure from Kaplan and Hegarty (2005).

A single receiver performing point positioning with carrier phases, as seen in Figure 3.1, is subject to the error sources mentioned in the previous section. In order to reduce the uncertainty of the estimated position, these errors need to be reduced. PPP is a method that uses precise orbital data and clock corrections to reduce the biases related to orbital errors and imprecise satellite clocks. The ionospheric refraction is solved by using a linear combination of the frequency bands from the GPS and/or GLONASS satellites, and the tropospheric refraction can be estimated by the receiver or from meteorological models (Kaplan and Hegarty, 2005; Hofmann-Wellenhof et al., 2008; Mireault et al., 2008). By using the linear combination (LC) of the frequency bands to estimate the tropospheric delay, the position of the receiver can be estimated by determining the receiver clock bias and the ambiguities. These two unknowns can be solved with several methods, including sequential least-squares adjustment and sequential filtering like the Kalman filtering technique (Kaplan and Hegarty, 2005; Hofmann-Wellenhof et al., 2008). PPP can be used both for static and kinematic positioning, meaning that the position of a receiver can be estimated for a stationary position or on an epoch-to-epoch basis as the receiver (or more precisely, the antenna) moves.

While the error sources mentioned in the previous section can degrade the uncertainty of an estimated position, there are also other cyclic processes that can affect the position of a GNSS station, including ocean tide loading, solid earth tides and crustal motion. These effects, together with the bias from antenna phase center variation, can be accounted for by applying respective corrections.



### 3.1.3 Relative positioning

Instead of using only one GNSS receiver, as the example of PPP, relative positioning is based on a principle where the position of a receiver at an unknown location is determined relative to the known position of a second stationary receiver. With simultaneous observations to the same satellites, the baseline vector between the two stations can be determined (Figure 3.2). Relative positioning uses a differencing technique that cancels out the clock biases. By calculating single-differences, i.e. the difference between the observations from the two stations  $A$  and  $B$  to the same satellite  $j$ , the satellite clock bias gets eliminated:

$$\begin{aligned}\Phi_A^j(t) + f^j \delta^j(t) &= \frac{1}{\lambda^j} \varrho_A^j(t) + N_A^j + f^j \delta_A(t) \\ \Phi_B^j(t) + f^j \delta^j(t) &= \frac{1}{\lambda^j} \varrho_B^j(t) + N_B^j + f^j \delta_B(t)\end{aligned}\tag{3.3}$$

representing the geometric time-dependent distance between the receivers and the satellite ( $\varrho_{A/B}^j(t)$ ), the integer ambiguity between each receiver and the satellite ( $N_{A/B}^j$ ), the receiver clock bias for each receiver at epoch  $t$  ( $\delta_{A/B}(t)$ ), the frequency and wavelength of the satellite carrier signal ( $f^j$  and  $\lambda^j$ ) and the fractional phase at epoch  $t$  between each receiver and the satellite, expressed in cycles ( $\Phi_{A/B}^j(t)$ ) (Hofmann-Wellenhof et al., 2008). When differencing the two equations, the satellite clock bias cancels:

$$\Phi_B^j(t) - \Phi_A^j(t) = \frac{1}{\lambda^j} [\varrho_B^j(t) - \varrho_A^j(t)] + N_B^j - N_A^j + f^j [\delta_B(t) - \delta_A(t)]\tag{3.4}$$

By further calculating the double-difference, which is the difference between two single-differences from two different satellites at the same epoch, the receiver clock bias is cancelled. Double-differences is a widely used technique in relative positioning, partly due to the elimination of both clock biases. The double-differences can further be used in triple-differencing, where the difference between two double-differences from two different satellites at two epochs are calculated, and leads to an elimination of the unknown integer ambiguity (Hofmann-Wellenhof et al., 2008).

For static relative positioning, the coordinates of the unknown location are the same for all observed epochs, and the observations from both receivers to the same satellites over several epochs are used to estimate the integer ambiguity. The same approach is used for kinematic relative positioning, but with new unknown coordinates for each new epoch for the moving receiver.

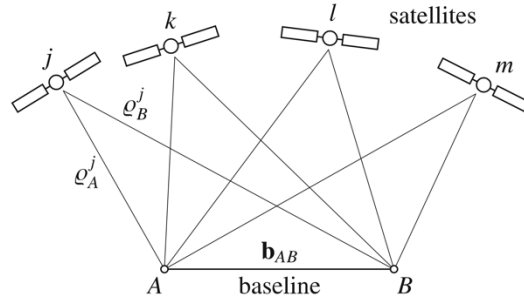


Figure 3.2. Illustration of relative positioning. The baseline between A and B is determined from simultaneous observations to the same satellites (Hofmann-Wellenhof et al., 2008)

Similar to PPP, the relative positioning technique can use a linear combination (LC) of the frequency bands to remove the influence of the ionosphere. Over short baselines, the influence of the ionosphere, as well as e.g. the tropospheric influence, is more or less the same for both stations, and cancels out in the differencing. For longer baselines, the ionospheric error cannot be expected to be the same at both stations, and forming LC is an effective way to remove this influence. But since the frequency-dependent error sources and noise are magnified when using the linear combination of the two frequency bands, it can be an advantage to use the frequency bands independently on short baselines (Kaplan and Hegarty, 2005; Herring et al., 2008).

To determine the unknown coordinates of the receiver, the integer ambiguities need to be solved, and Hofmann-Wellenhof et al. (2008) describes three major steps in ambiguity resolution. The first step is to define a search space of the potential integer ambiguity combinations between the unknown receiver and the satellites, and the second step identifies the correct combination of integer ambiguities often by using a least-squares adjustment. The latter technique often consists of three sub-steps: finding a float solution, an integer ambiguity estimation and a fixed solution. The last major step is to validate the determined ambiguities, often by evaluating the ambiguity success rate, i.e. the percentage of solved ambiguities.

Relative positioning can be used for a baseline between two receivers, as well as for a solution where several receivers are included in a network. The baselines within the network can be computed with a single-baseline solution or with a multipoint solution where all points in the network are considered at the same time, and the resulting vectors are adjusted using a least-square adjustment of the baselines (Hofmann-Wellenhof et al., 2008).

### 3.1.4 Satellite constellation and coverage

The GPS and GLONASS satellites have different configurations, which are reflected in their availability and location on the sky. GPS satellites orbit in six different planes with a  $60^\circ$

separation and  $55^\circ$  inclination from the equatorial plane, and the system has four satellites on each orbital plane as the baseline configuration (Kaplan and Hegarty, 2005). This compares to the three orbital planes with  $120^\circ$  separation and  $64.8^\circ$  inclination for GLONASS, with seven active satellites and one spare satellite on each orbital plane (Kaplan and Hegarty, 2005). The difference in inclination between the systems becomes evident when making observations to satellites from both systems, as illustrated in Figure 3.3. The polar hole without satellite coverage is larger for GPS than GLONASS, and this leads to a different geometric distribution of the satellites on the sky.

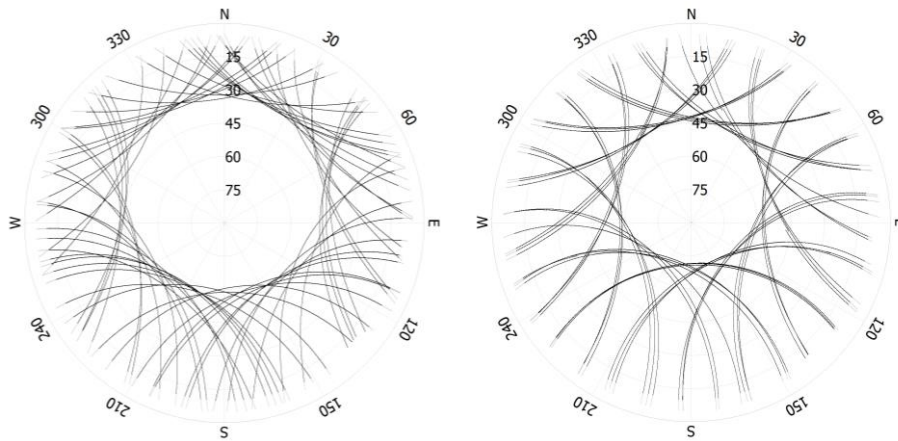


Figure 3.3. Skyplot of the available GPS- (left) and GLONASS (right) satellites at HDF1 on July 7<sup>th</sup> 2015. All angles of inclination and azimuths are in relation to the position of the antenna at HDF1. The elevation cut-off angle of  $10^\circ$  is illustrated by the transition to grey lines. The figure was made in RTKLIB.

The geometry of the satellites has an influence on the achievable precision in the trilateration process. Hofmann-Wellenhof et al. (2008) states that “*systematic errors or biases in the pseudoranges can be reduced or eliminated by differencing the measured pseudoranges either between satellites or between sites. However, no mode of differencing can overcome poor geometry*”. This geometrical consideration is an important concept within surveying, since the angles of intersecting measurements have an impact on the uncertainties of the resulting positions. From a pure geometrical point of view, two ranging measurements should ideally intersect at a perpendicular angle to minimize the combined bounds of uncertainty derived from the individual uncertainty of each range measurement. For other angles, the combined bounds of uncertainty, i.e. the dilution of precision (DOP) is larger (Kaplan and Hegarty, 2005).

For GNSS observations, the geometry of the satellites can be expressed by the numerical geometric dilution of precision (GDOP) value at given epoch, with improving geometry for decreasing GDOP values. In Figure 3.3, the GDOP values for both GPS satellites and the combination of GPS and GLONASS satellites are given for a 24-hour interval at the study site,

and it illustrates both the increased number of available satellites and lower GDOP values when combining the two satellite systems.

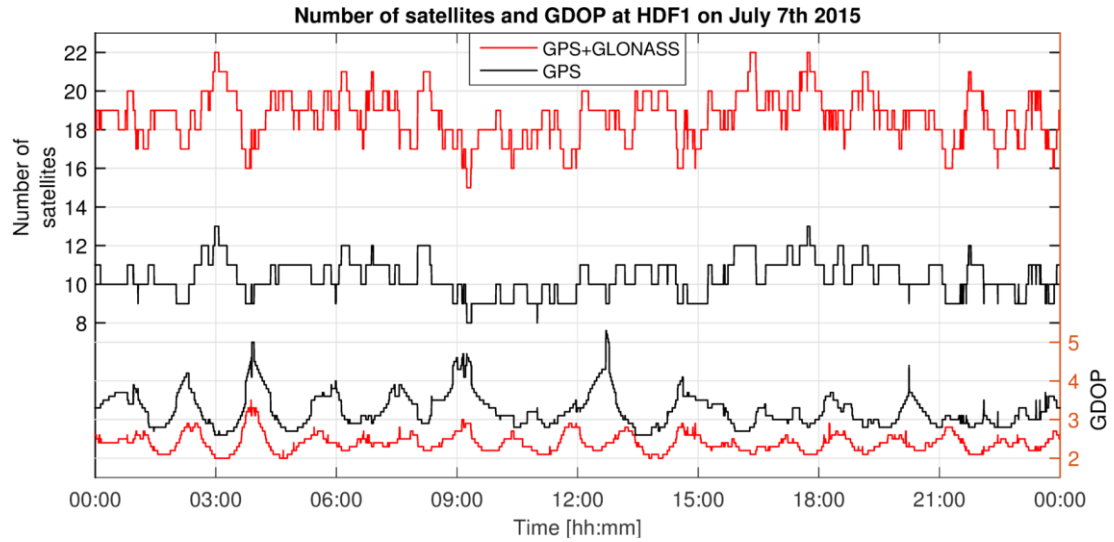


Figure 3.4. Combined plot of the number of available satellites and Geometric Dilution of Precision (GDOP) for both GPS and GLONASS, at the GNSS station HDF1 on July 7<sup>th</sup> 2015. A maximum of 22 satellites were available when using GPS+GLONASS, while the number of available GPS satellites reached a minimum of 8. The GDOP values show how the geometric constellation of the satellites can reduce the precision of the measurements, and has a maximum value above 5 for GPS when the distribution of satellites is the least favorable.

### 3.2 Glacier motion and dynamics

The movement of a glacier can be ascribed to the plastic deformation of the ice and the basal motion (also referred to as basal slip), where the latter includes both the sliding over the glacier bed and deformation of the glacier bed (Cuffey and Paterson, 2010). Direct measurements of basal slip are, for obvious reasons, challenging, but it is possible to observe the motion in accessible subglacial cavities and tunnels, as well as with down-borehole photography (Cuffey and Paterson, 2010). The motion related to plastic deformation of the ice, also referred to as internal deformation, can be directly measured through borehole tilt measurements (e.g. Gudmundsson et al., 1999).

For an arbitrary depth  $z$  along the vertical profile of a glacier, the total motion comprises both the basal slip  $u_b$  and the depth-dependent deformational velocity  $\frac{\partial u}{\partial z}$  (Cuffey and Paterson, 2010):

$$u(z) = u_b + \int_B^z \frac{\partial u}{\partial z} dz \quad (3.5)$$

where  $B$  to  $z$  is from the bed to a given depth/elevation along the vertical profile, respectively. Thus, the surface velocity is a combination of the total internal deformation over the entire vertical profile and the basal slip.

There are several factors that induce the glacier motion, and the time-scales for how they affect the motion are different. When considering the mass balance of a glacier, the net mass gain in the accumulation and the net mass loss in the ablation area are related to the mass balance gradient (Benn and Evans, 2010). The equilibrium line altitude (ELA) defines the altitude of the boundary between the accumulation and ablation zone for a given mass balance year (Cuffey and Paterson, 2010). In order to maintain a steady state of the glacier, the mass gained in the accumulation zone must be transferred down-glacier to replace the mass loss in the ablation zone (Benn and Evans, 2010). The balance velocities for a glacier are thus related to the ice motion that is required to balance the mass gained and lost. For a glacier with a steep mass balance gradient, i.e. high rates of both mass gain in the accumulation area and mass loss in the ablation area, the balance velocities are higher than for a glacier with a less steep mass balance gradient (Benn and Evans, 2010). The downward flow of ice in the accumulation zone, relative to the glacier surface, is referred to as the submergence velocity, while the opposite upward flow in the ablation zone is the emergence velocity (Cuffey and Paterson, 2010). The mass balance related motion described above can be categorized as a more long-term factor for the overall motion of a glacier and varies over an inter-annual time-scale.

The geometry of the glacier and constrictions impact the flow velocities. A glacier with a large accumulation area that drains into a narrow valley can require high balance velocities to maintain the equilibrium state of the glacier. The balance velocities can be further increased if the elevation difference between accumulation and ablation area is large, with high rates of precipitation in the accumulation area and large ablation rates near the terminus of the glacier (Benn and Evans, 2010).

The temperature regime of the glacier is an important factor for how they move. The motion of a cold-based glacier is limited to the internal deformation of the ice and the upper part of the bed (Benn and Evans, 2010). Temperate or warm-based glaciers with temperatures at the pressure-melting point are not frozen to the bed like the cold-based glaciers, and can experience significant bed sliding. The pressure-melting point is the temperature at which the ice melts for different pressures, but is also affected by the impurities in the ice (Cuffey and Paterson, 2010). If looking at a column of ice, the load of the overlying ice causes increasing pressures from the surface and down-wards, thus lowering the temperatures at which the ice can melt. Polythermal

glaciers are the combination of the two mentioned types above, with both cold- and warm-based areas. Most glaciers on Svalbard are polythermal (Hagen et al., 2003).

Basal sliding account for most of the intra-annual variation in the glacier motion and is closely related to the lubrication of the glacier bed at the pressure-melting point. While basal melt contributes to the lubrication of the glacier bed, it is normally the external inputs of water that causes the larger fluctuations in basal slip. How the input of water affects the basal slip depends on the properties of the subglacial hydrologic drainage system. If considering a rough bed, the down-glacier motion over bumps can cause cavities to form on the lee-side. These cavities can fill with water and connect to other cavities through narrow channels, called linked-cavity systems (Walder and Hallet, 1979; Fowler, 1987; Cuffey and Paterson, 2010). The size of the cavities are dependent on the sliding speed and melting of the cavity walls and roof, in addition to increases in the water pressure (Benn and Evans, 2010). With increasing input of water to the glacier bed, the effective pressure. i.e. the difference between the ice pressure due to the overlying ice and the water pressure, reduces and thus causing a decrease in the basal shear stress that promotes increased bed slip (Benn and Evans, 2010). The growing cavities thus leads to bed separation, where the ice is lifted from the glacier bed. Over the course of the melt season, the increases in meltwater input usually develop large well-connected cavities that gradually changes the subglacial hydrologic system into a more efficient drainage system with larger tunnels. As Benn and Evans (2010) points out, the existence of linked-cavity systems are most favorable for glaciers with a fast basal motion over a rough bed and with small rates of water input, a typical condition for some glaciers during winter.

The glacier ice is constantly being affected by external and internal forces, which lead to stress and strain that are unequally distributed along the horizontal and vertical planes of a glacier. While stress is a measure of the compression, stretching or twisting from an applied force, strain is a measure of the deformation caused by the stress (Benn and Evans, 2010). For glacier flow, two principle stresses are present: driving and resistive stress. The driving stress is the gravitational force pulling the glacier down in the vertical direction, and has a horizontal component when a sloping bed is present (Cuffey and Paterson, 2010). The resistive stresses include the external drag from the glacier boundaries and the internal stress from the ice viscosity (Benn and Evans, 2010).

Since the flow velocities of a glacier vary along the longitudinal, lateral and vertical directions of the glacier, their differences in magnitude cause strain in the ice. Ice is nearly incompressible, but it is for many applications considered as incompressible. This means that for a finite volume of

ice that is affected by strain in all perpendicular directions, the deformation can change the shape but not the absolute volume of the ice. This yields that the sum of the total strain in the longitudinal, lateral and vertical directions is zero. By assuming that ice is incompressible, the vertical strain rate  $\dot{\epsilon}_{zz}$  can be approximated with the continuity equation:

$$\dot{\epsilon}_{zz} = -(\dot{\epsilon}_{xx} + \dot{\epsilon}_{yy}) \quad (3.6)$$

where xx, yy and zz represent the longitudinal, lateral and vertical directions, respectively (Cuffey and Paterson, 2010; Andrews et al., 2014). Given a scenario where the lateral strain remains constant, this relation means that a compression due to longitudinal strain causes an equal extension in the vertical direction, and vice versa.

### 3.3 Glacier hydrology and surface mass balance

The connection between lubrication of glacier bed and glacier motion has been described in the previous section, where the glacier motion includes both the bed-parallel glacier sliding and vertical motion due to bed separation. In order to understand the motion of the glacier surface, it is thus useful to estimate the amount of water that can enter the subglacial hydrologic system of the glacier. This includes precipitation and surface melt of the glacier and from adjacent hillslopes (Cuffey and Paterson, 2010), which can drain to the glacier bed through the englacial drainage system, or get stored in supraglacial lakes on the surface. However, the effect of re-freezing and temporary storage of water englacially or in the firn layer are buffers that can temporarily reduce or delay the amount of water reaching the subglacial hydrologic system.

The surface mass balance  $\dot{b}_s$  of a glacier is determined by the mass exchange at the surface, and is given as

$$\dot{b}_s = \dot{a}_s + \dot{a}_a - \dot{m}_s + \dot{a}_r - \dot{s} + \dot{a}_w \quad (3.7)$$

representing snowfall ( $\dot{a}_s$ ), avalanche deposition ( $\dot{a}_a$ ), melt ( $\dot{m}_s$ ), refreezing of water ( $\dot{a}_r$ ), sublimation ( $\dot{s}$ ), and wind deposition ( $\dot{a}_w$ ) (Cuffey and Paterson, 2010). A model of the surface mass balance of a glacier includes an estimation of the different parameters in (3.7), and can thus quantify the runoff derived from melting of snow and ice. Van Pelt and Kohler (2015) modelled the surface mass balance of Høltedahlfonna and other adjacent glaciers between 1961-2012 by simulating mass- and energy exchange between the atmosphere, surface and subsurface, i.e. underlying snow, firn and/or ice. The surface mass balance model used the HIRLAM regional climate model with 11 km horizontal resolution at 3-hour intervals as meteorological forcing,

with air temperature, humidity, cloud cover, air pressure and precipitation as inputs to the model, and has a downscaled gridded output resolution of  $100 \times 100$  m. Since the surface mass balance model simulates the melt production and takes into account refreezing near the surface, it can thus give an estimate of the glacier runoff.

The surface mass balance does not include calving, which can be a considerable factor for mass loss on marine-terminating glaciers. Nuth et al. (2012) estimated a long-term calving flux for Høltedalsfonna/Kronebreen of -0.37 to -0.52 m w.e.  $\text{a}^{-1}$  between 1966-2007 (Van Pelt and Kohler, 2015). The estimated calving flux thus largely outweighed the modelled surface mass balance of 0.13 m w.e.  $\text{a}^{-1}$  by Van Pelt and Kohler (2015) for the period 1961-2012.



## 4 Methods

This chapter contains the methods applied in this study. The first section describes the fieldwork conducted in 2014 and 2015 and the setup of the GNSS stations. The following two sections will go through the GNSS post-processing and the glaciological computations. In the last section, the statistical methods and uncertainty calculations are presented.

### 4.1 Fieldwork

In order to perform relative positioning of the GNSS stations, a network of base stations on solid ground and rovers on the glacier was created. During the 2014 field season, a total of two stations (HDF1 and HDF3) were located on the glacier, and an additional station (HDF2) was installed during the field work in spring 2015. A base station (HAGN) was installed on a nunatak at the Kongsvegen glacier, approximately 12 km south-southwest of HDF1. In addition, the Norwegian Mapping Authorities has two permanent GNSS-station (NYA1) in Ny-Ålesund that runs continuously, making them suitable as base stations. NYA1 is located approximately 29 km west of HDF1 and 30 km northwest of HAGN. The locations of all the GNSS stations are marked in Figure 2.1.

The stations were designed to endure the tough arctic climate, and to be self-supplied with electricity during the entire year. The latter is of importance, since the access to the remote stations is at times difficult, and the need for maintenance is expensive and time-consuming. The design of the GNSS stations has continuously been tested and improved in the years prior to 2014 (Christopher Nuth, unpublished data), but due to several potential error sources, including meteorological conditions, data gaps due to depleted batteries and problems with the components still occur.

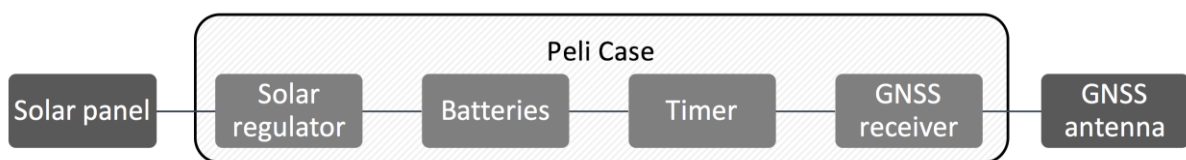


Figure 4.1. Overview of the general setup of all the GNSS stations. The solar regulator, batteries, timer and GNSS receiver is protected inside a durable box (Peli Case).

An overview of the setup of each GNSS station is illustrated in Figure 4.1. The solar panel delivers a maximum of 24 V, which subsequently is reduced to 12 V by the solar regulator before reaching the 12 V batteries. The batteries are charged whenever the light conditions are favorable

for the solar panels, and are thus naturally limited during the polar night (October 24<sup>th</sup> to February 18<sup>th</sup> in Ny-Ålesund (Yr, 2012)). It was thus necessary to minimize the power consumption of the system during the winter season, and a timer was added for this purpose. The timers were programmed to reduce the observation period from 24 hours to 2 hours per day, and the winter program was set to operate between ~September 1<sup>st</sup> to April 30<sup>th</sup>. The dimensions of the batteries (~180-240 Ah from 2-6 batteries) were chosen according to an estimation of solar input and battery consumption during the winter season (Christopher Nuth, personal communication, 2015).

For the stations on the glacier, HDF1-3, the GNSS antenna and solar panel were mounted on existing stakes from the NPI mass balance program (Figure 4.2), and the naming of each GNSS station is thus based on the name of the according mass balance stake. The stakes have a standardized length of 6 m, and are normally installed by drilling and freezing the stake into the ice. The bottom end of the stake, which is frozen into the ice, can be assumed to have a constant position independent of the seasonal accumulation and ablation on the glacier surface. However, it is possible for the stakes to melt further down into the ice during the summer season when the stake is exposed to higher temperatures and solar radiation, but this is considered as negligible in this study.



Figure 4.2. Left: the HDF3 station with the antenna and solar panel mounted on a mass balance stake. The picture was taken during fieldwork in fall 2015, and shows the ice surface without snow. Right: the HAGN base station located on a nunatak at the Kongsvegen glacier. The choke ring antenna was mounted directly to a bolt drilled and cemented into the bedrock. The antenna cable was covered with rocks to prevent foxes from chewing on the rubber insulation. The pictures were taken in fall (left) and spring (right) 2015 by the author.

During fieldwork in spring (April/May), at the end of the winter accumulation season, the snow reached far up on the mass balance stakes, and often reaching the bottom side of the solar panel. Thus, the height of the solar panel on the stake needed to be considered when installing the

station. The boxes containing the GNSS receiver, batteries, timer and solar regulator were located at the glacier ice surface, or often melted into the ice, and had to be dug out and lifted up to the snow surface. Observational data from the winter season were downloaded from the internal memory of the GNSS receiver, and necessary adjustments to the system were made. In spring, the fieldwork was conducted with snowmobiles, and the equipment was transported on sledges.

During fall, the mass balance stakes on the glacier and the HAGN base station were accessed by helicopter, due to the lack of snow in the terrain and large distances between Ny-Ålesund and the different field sites. Data from the summer season were downloaded and necessary adjustments on the components were made, similar to the spring fieldwork.

Table 4.1. GNSS stations in the period September 1<sup>st</sup> 2014 – August 31<sup>st</sup> 2015. NYAL and NYA1 are the official IGS names for these two stations. The GNSS stations on the glacier were limited to two hours of daily observations between September 2014-April 2015.

Stations	Sample int. [sec]	Receiver	Antenna	Sat. signal	Data gaps	Location
NYA1	1	Trimble NetR8	ASH701073.1	GPS+GLO		Ny-Ålesund
NYAL	1	Trimble NetRS	AOAD/M_B	GPS		
HAGN	5	Trimble NetR8	AOAD/M_T	GPS+GLO	Winter 2014/2015	Nunatak at Kongsvegen Glacier
HDF1	5	Trimble NetR8	TRM55971.00	GPS+GLO	2015: doy 126-174, 230-243	
HDF2*	5	Trimble NetR8	TRM55971.00	GPS+GLO		
HDF3	5	Trimble NetR8	TRM55971.00	GPS+GLO	2014: doy 331-365. 2015: doy 1-65	

\* HDF2 was installed at the end of April 2015. GLO = GLONASS. DOY=Day of year.

In addition to the installation and maintenance of the GNSS stations described above, a kinematic GNSS survey of the glacier snow surface and snow depth measurements were conducted during the fieldwork in spring 2015. The aim for this survey was to determine the elevation of the glacier ice surface in the areas around the GNSS stations, covering both their previous positions up-glacier and the predicted future positions down-glacier. However, the results from the kinematic survey have not been implemented in this study, but the details are included in Appendix 9.3.

## 4.2 GNSS post-processing

The GNSS receivers store the observations to all available satellites at each epoch in raw files, which need to be converted into an ASCII format readable for the GNSS post-processing

software. A standardized and commonly used format is The Receiver Independent Exchange Format (RINEX), which makes it possible for the software to handle observation files from multiple GNSS receivers (Gurtner and Estey, 2007). The RINEX file format includes the observation file, containing the code- and phase measurements to each satellite, the navigation file based on the broadcast navigation message and a meteorological file (Gurtner and Estey, 2007).

The number of epochs in each observation file is defined by the set sample interval of the GNSS receiver, which is either 1 or 5 s on the receivers in this setup (Table 4.1). With relative positioning, only the matching epochs from all the observation files are used, making the receiver with the lowest sample interval the deciding factor of the frequency of positions in a kinematic solution.

#### **4.2.1 Software**

For the post-processing, two different software packages and an online PPP service were used:

- RTKLIB 2.4.2
- GAMIT/TRACK 10.5
- CSRS PPP

RTKLIB is a free open source software that supports a variety of positioning methods for real-time and post-processing, including relative positioning and PPP (Takasu, 2013). It supports multiple satellite systems, including GPS and GLONASS, and can perform relative positioning between a base station and a rover, both for kinematic and static positioning (Takasu, 2013). RTKLIB has only been used for relative positioning in this study.

GAMIT is an academic software package developed at Massachusetts Institute of Technology (MIT), widely used (e.g. Manson et al., 2000; King, 2004; Williams et al., 2004) in studies using relative positioning for GPS observations. The software can perform static and kinematic positioning through the GAMIT and TRACK modules, respectively, and has the option of processing multiple static and kinematic stations in a network solution (Herring et al., 2015).

The Canadian Spatial Reference System precise point positioning (CSRS PPP) is an online service by Natural Resources Canada that allows the user to process in static- and kinematic mode both for GPS and GLONASS satellites (Mireault et al., 2008). The PPP service has the option for the user to provide corrections for ocean tidal loading, and a velocity grid takes accounts for crustal motion (CGS, 2015).

Precise satellite orbits were provided for all processing sessions in both GAMIT/TRACK and RTKLIB (IGS, 2009; CODE, 2015). OTL corrections for the study area were acquired from the Onsala Space Observatory (Bos and Scherneck, 2011). Correction files for the antenna phase variation center (PVC) was implemented in both software packages.

#### **4.2.2 Static positioning**

In order to use the GNSS station on the nunatak (HAGN) as a base station for the relative positioning, a precise coordinate of its location must be determined. The permanent GNSS stations in Ny-Ålesund (NYA1 and NYAL) run continuously with a 1-s sample interval, and can not only serve as base stations for the GNSS stations on the glacier, but also for determining the coordinates of the fixed position of HAGN. HAGN was processed in GAMIT with static relative positioning, using NYA1 as a base. The observation files were processed in 24-hour intervals over two weeks, centered on July 21<sup>st</sup> 2015, marking the midpoint of the summer season data with continuous, overlapping observations from all stations. The resulting baselines between NYA1 and HAGN were given in cartesian coordinates, and the HAGN coordinates were calculated relative to the ITRF08 coordinate of NYA1 on July 21<sup>st</sup>. The average of the 14 coordinates was later on used as the a priori coordinate of HAGN when including it as a base station in the relative positioning.

#### **4.2.3 Pseudo-static positioning**

To analyze motion of the GNSS stations, i.e. the glacier, a processing routine that allows movement of the GNSS station must be used. In general, static processing is used for stations at fixed locations, while kinematic is generally the preferred method when determining the location of a non-fixed moving station. The different modes of motion throughout the season must be taken into account when choosing a processing routine. While kinematic processing usually is the preferred choice when processing moving stations, it is also possible to use static processing if the displacements of the station within the processing interval are small enough. One challenge is therefore to choose an interval with a sufficient number of observations and also ensure that the displacements are small enough to not interfere in the ambiguity resolution. Critical threshold are the wavelengths of the GNSS signals, and displacements of these orders within the processed interval can possibly lead to integer shifts in the ambiguity resolution.

To examine the difference between the software packages, satellite systems and segment duration, the HDF1 station was processed with GAMIT (GPS), RTKLIB (GPS+GLONASS) and PPP (GPS+GLONASS) for 0.5-, 1-, 2- and 3-hour intervals. By choosing NYA1 as a base station for the processing in GAMIT and RTKLIB, the test can be used to determine the optimal method for processing the 2-hour observations per day during the winter season on HDF1 and HDF3. While GAMIT and RTKLIB have the option of choosing the number of epochs that are to be solved and the length of the output interval, this is not possible with the online CSRS PPP service. For the latter method, the observation files had to be divided into the desired interval length before submitting the data for processing, and this was conducted using RTKLIB.

When the observation files have original sample intervals shorter than 30 s, CSRS PPP processes the data at 30-s intervals for static mode. The service claims in the result files that this should not affect the position estimates, but it might have an effect when processing over shorter intervals (e.g. 0.5 hours), since it reduces the number of observations down to 1/6 of the original data with 5-s sampling interval.

Preliminary results of the motion of the GNSS stations were used to determine the timing of the test period, with a defined prerequisite of containing periods with horizontal surface velocities similar to those in winter and at the same time including events of acceleration and peak surface velocities. The duration of the test period was set to one week, which enables a thorough evaluation of both the sub- and inter-daily variation in the results.

#### **4.2.4 Kinematic positioning**

When using kinematic positioning in the post-processing, a position of each epoch is estimated, which for the data in this thesis is every five seconds. This leads to a high temporal resolution in the resulting coordinates, but with a larger spatial variation, when comparing to the potential of static processing. To evaluate the different software packages, satellite systems and setup of base stations, the GNSS observations were processed over the same test period as for the pseudo-static processing.

As stated previously, the RTKLIB software supports relative positioning with one rover and one base station. The observations of HDF1 on the glacier were processed with HAGN as base station, using observations to both GPS and GLONASS satellites. TRACK can only process GPS observations, but has the option of using several base stations and rovers in a network. To evaluate the effect of processing with single and multiple base stations, together with one or all

moving stations on the glacier, different combinations of these setups were processed in the TRACK software (Table 4.2).

Table 4.2. The different combinations of relative positioning conducted in TRACK.

Test	Base	Rovers	Search and analysis mode
1	NYA1	HAGN	LC
2	NYA1	NYAL	L1+L2
7	NYA1	HDF1	LC
8	NYAL	HDF1	LC
9	HAGN	HDF1	LC
10	HAGN, NYA1	HDF1	LC
11	HAGN, NYA1	HDF1, HDF2, HDF3	LC
12	HAGN	HDF1	L1+L2

*LC = Linear Combination of L1 and L2. L1+L2 = The two phase carriers treated as independent observables.*

When evaluating the precision of the estimated positions of the stations on the glacier, one must take into account the continuous horizontal and vertical displacement. The processing software estimates the internal accuracy of each measurement, but it is useful to evaluate if the given accuracies agree with the variation in the estimated positions of the stations on the glacier. By processing a stationary point in kinematic mode, one can evaluate the variation in each position estimate compared to the long-term mean or to a precise position estimate from long static sessions. In other words, by processing the HAGN station in kinematic mode using NYA1 as a base station, it is possible to analyze the variation in the horizontal and vertical coordinates of the kinematic solution from the long-term average position. Since HAGN and the stations on the glacier have distances to NYA1 and elevations that are within the same range, it is possible to evaluate the precision of the position estimates of the moving HDF1 station using the stationary HAGN station.

Due to the baseline of approximately 30 km from NYA1 to HAGN and HDF1/2/3, LC was used for most of the mentioned tests in Table 4.2. The exceptions are for test 2 and 12, which were processed using L1+L2. Since the baseline between NYAL and NYA1 is only a few meters, the atmospheric influence is the same at both stations, opposite to the longer baselines. By processing NYAL with NYA1 as base station, the aim is to show the achievable accuracy for short baselines using the L1+L2 technique, and how the results compare to the longer baselines. Additionally, the same technique was also used to process HDF1 with HAGN as base station, to see the effect of a ~12-km increase in baseline on the estimated positions.

Also included in the kinematic test are the results from PPP. Since the CSRS PPP service can process both GPS and GLONASS observations, it is possible to evaluate the effect of using both satellites systems compared to only using GPS or GLONASS. Since it is not possible to choose the satellite system in the CSRS PPP service, the RINEX observation files were divided into new files containing GPS and GLONASS observations separately. Unlike the static processing, CSRS PPP is able to process in kinematic mode with the original observation interval, yielding a 5-s interval between the estimated positions.

#### **4.2.5 Reference frames and coordinate system conversion**

The precise satellite orbits are referenced in the International Terrestrial Reference System (ITRS) with a realization in the International Terrestrial Reference Frame 2008 solution (ITRF08), and all resulting positions of the GNSS stations are thus given in the ITRF08 reference frame with cartesian equatorial coordinates  $(x, y, z)$ . ITRF is in general identical to the commonly used World Geodetic System revision 84 (WGS84) datum at one meter level, depending on the realization of both datums (IGN, 2013). IGN (2013) states that ITRF08 and the recent realization of WGS84 (G1674) are likely to agree at the centimeter level, and that no official transformation parameters have been established for this and the last few realizations. Thus, no transformation was conducted when collating the GNSS data with other data referenced to the WGS84 datum.

To convert the coordinates from a cartesian-  $(x, y, z)$  to a geodetic (latitude, longitude, height) coordinate system, the iterative algorithm from Bowring (1985) was used (Craymer, 2013). This algorithm uses the cartesian coordinates  $(x, y, z)$ , length of major semi-axis and eccentricity of the WGS84 ellipsoid as inputs. All geospatial data used in this thesis was projected to the Universal Transverse Mercator (UTM) conformal projection zone 33 N with heights above the WGS84 ellipsoid. Raster and vector data was projected in the Geographic Information System (GIS) framework ArcGIS (ESRI, 2015). The GNSS coordinates were converted in Matlab (MathWorks, 2014) using a function (Schimel, 2012) based on Snyder (1987). All subsequent computations of the GNSS positions were also conducted in Matlab (MathWorks, 2014). With GNSS positions given in UTM coordinates with meter as the unit of length, comparison of horizontal positions and calculation of displacements could be done directly.



### 4.3 Glaciological computations

Due to the background variation in the computed GNSS-coordinates, a direct velocity calculation between each coordinate from kinematic processing with 5-s intervals would give velocity values that does not reflect the true motion of the GNSS-station. It is thus necessary to calculate the velocity over larger time-spans, e.g. 1-, 3- or 24-hour intervals, where the length of the interval is depending on the accuracy of each coordinate and the displacement of the GNSS-station. To minimize the effect of background noise in the data, a running average was calculated for each coordinate before calculating the velocities. A running mean was also used to improve the visualization of the results in the time-series. The moving average was calculated for each coordinate along the entire time series:

$$\bar{x}_i = \frac{1}{2n+1} \sum_{j=i-n}^{i+n} x_j \quad (4.1)$$

representing the number of measurements in each direction in time for each coordinate ( $n$ ) and the time ( $i$ ) of the coordinate  $x_i$  that is to be calculated.

The (moving) averaged coordinates were used in the calculation of horizontal- and vertical surface velocities:

$$u_{h,n} = \frac{\sqrt{(\bar{x}_j - \bar{x}_i)^2 + (\bar{y}_j - \bar{y}_i)^2}}{(t_j - t_i)} \quad (4.2)$$

$$u_{v,n} = \frac{(\bar{h}_j - \bar{h}_i)}{(t_j - t_i)} \quad (4.3)$$

representing horizontal velocity ( $u_h$ ) and vertical velocity ( $u_v$ ) at a given time interval ( $n$ ), east-coordinate ( $x$ ), north-coordinate ( $y$ ), elevation ( $h$ ), time ( $t$ ), beginning ( $i$ ) and end ( $j$ ) of interval. The formula for the vertical surface velocity yields negative values when a station moves downwards.

Since the surface slope is different at each GNSS-station on the glacier, a direct comparison of the vertical coordinates is difficult. However, by de-trending the elevations for each station throughout the season, the independent changes at each station become more obvious. The trend calculation was based on a common background period of 14 days with continuous data for HDF1-3 when the horizontal vertical motion was more or less constant. The data was de-trended by least-squares fitting of a first degree polynomial (linear) to the initial background

period, and the calculated linear trends were used to remove the trend of the entire summer season data. A similar trend line was calculated by Iken et al. (1983) for the winter vertical displacement, but they presented the trend line together with the melt season data rather than de-trending the data. When de-trending the vertical motion of the summer season based on the first 14 days, it represents the relative changes in surface elevation from the initial trend, and must be evaluated accordingly.

### 4.3.1 Deformation and bed sliding velocity

The GNSS-stations measure the surface velocity of the respective locations on the glacier, but in order to understand the motion at the glacier bed, the horizontal velocity ( $u_b$ ) due to basal slip must be estimated. For calculating the deformation velocity and its relation to the surface- and bed sliding velocity, the following simplified relation was used (Cuffey and Paterson, 2010):

$$u_s = u_b + \frac{2A}{n+1} \tau_b^n H \quad (4.4)$$

representing the horizontal surface velocity ( $u_s$ ) and bed velocity ( $u_b$ ), the creep parameter ( $A$ ), the creep relation ( $n$ ) for ice, the basal shear stress ( $\tau_b$ ) and the ice thickness ( $H$ ). The creep relation ( $n$ ) is defined by Glen's Law, and most analyses of glacier dynamics assume a value of  $n=3$  (Cuffey and Paterson, 2010). Thus,  $n=3$  have been used in the calculation of the deformation velocity.

The driving stress ( $\tau_d$ ) is the effect of gravity pulling the ice in the downglacier direction, and is given by

$$\tau_d \approx \rho g H \alpha_s \quad (4.5)$$

representing the mean density of the ice ( $\rho$ ), the gravity constant ( $g$ ), the ice thickness ( $H$ ) and the surface slope ( $\alpha_s$ ) in radians (Cuffey and Paterson, 2010). The latter expression assumes small angles of bed- and surface slope, yielding  $\sin(\alpha_s) \approx \alpha_s$  (and  $\sin(\alpha_b) \approx \alpha_b$ ). The formula thus implies that the driving stress is determined by the surface slope, and that the bed slope is of minor importance (Cuffey and Paterson, 2010). The surface slope was calculated from the averaged surface elevations over a  $\sim 8 \text{ km}^2$  area centered 1.5 km upslope and downslope from HDF2, and the ice thickness was averaged over a  $\sim 8 \text{ km}^2$  area surrounding HDF2. This reduces the effects of small-scale variation on the surface and ice thicknesses, and is according to recommendations by Benn and Evans (2010) and Cuffey and Paterson (2010).

The basal shear stress ( $\tau_b$ ) is directly related to the driving stress ( $\tau_d$ ):

$$\tau_b = f' \tau_d \quad \text{where} \quad f' = \frac{A_r}{Hp^*} \quad (4.6)$$

where  $f'$  is the shape factor, determined by the the area of the glacier cross section ( $A_r$ ), the ice thickness ( $H$ ) and the “glacierized perimeter” of the cross section ( $p^*$ ) (Benn and Evans, 2010). The shape factor thus expresses the geometry of the glacier in a simplified way. While ice far from lateral boundaries would has a value of  $f'=1$ , valley glaciers normally have a value ranging between 0.5-0.9 (Benn and Evans, 2010; Cuffey and Paterson, 2010). For the middle part of Høltedalsfonna, the calculation of the shape factor is not straightforward with the given formula, since the glacier is close to the lateral boundary on the southeast side and borders to Kongsbreen on the northwest side. No bed map for Kongsbreen is available, and the dynamics in the interaction between the two glaciers is not known. Given the proximity to the lateral boundary on the southeast side, the shape factor is assumed to have a value of  $f'<1$ . A calculation of the shape factor for the profile in Figure 4.3 was conducted. A glacierized perimeter only measured along the glacier bottom and not taking into account the northwestern margin yields  $f'=0.67$ . If considering the northwestern margin as static and as a part of the glacierized perimeter, the shape factor reduces to  $f'=0.6$ . A suggested value of  $f'$  would then lie somewhere between 0.60 and 1. A sensitivity analysis of the changes in deformation velocity for different values of  $f'$  was made, together with different values for the creep parameter  $A$ , as further explained below.

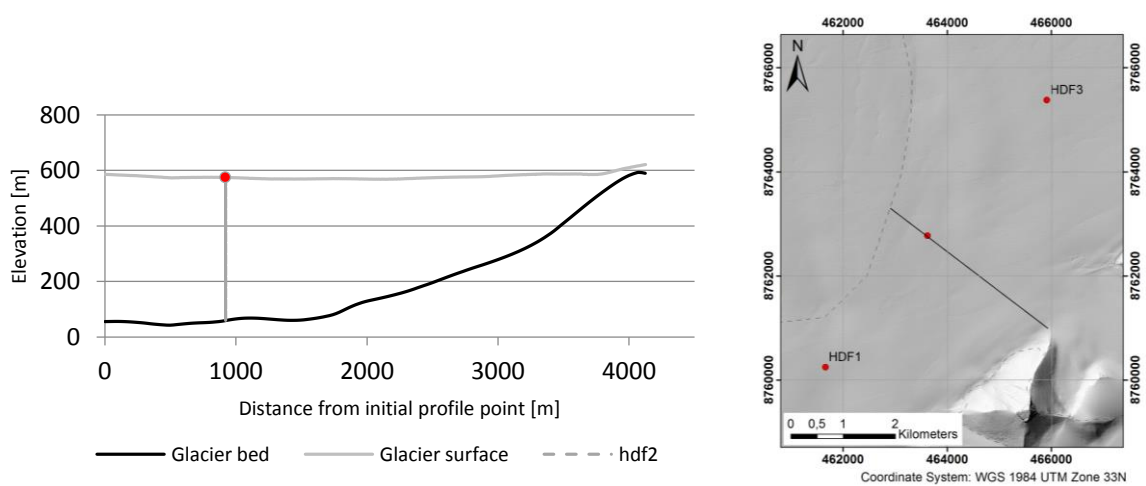


Figure 4.3. Left: Vertical profile of the glacier along a lateral transect from the glacier margin on the southeast side and to the border to Kongsbreen, and intersecting HDF2. The bed topography is from GPR measurements (J. Kohler, unpublished data) and the surface elevation is from a DEM (NPI, 2014). Right: The horizontal path of the lateral transect. The shaded relief is derived from a DEM (NPI, 2014) and the dashed glacier outline is from GLIMS (König et al., 2014).

The creep parameter  $A$  is treated as a constant in Equation 4.4, which is not true for the entire column of ice due to a variation in e.g. temperature and water content (Cuffey and Paterson, 2010). However, since the temperature regime of the ice below HDF2 is unknown, a qualitative assessment of an  $A$ -value must be made, and viewing it as a column depth average is thus useful. A general assumption of the temperature regime below HDF2, which is located below the ELA, is that a cold ice layer ranges from the surface and down to a given depth, before transitioning into temperate reaching all the way to the glacier bed. This pattern has been observed in several studies of the area below the ELA on sub-polar polythermal glaciers (e.g. Björnsson et al., 1996; Jania et al., 1996).

The temperature regime of parts of the neighbouring glacier Kongsvegen was analyzed by Björnsson et al. (1996). By measuring the temperatures along a borehole right below the ELA, they found a basal layer of temperate ice overlain by a  $\sim 100$  m thick cold layer of ice. Kongsvegen is currently in a quiescent phase, and the dynamics are very different compared to Høltedahlfonna, with surface velocities of only a few meters per year in the middle part. However, it is adjacent to HDF, giving a similar climate, and has a considerable ice thickness ( $\sim 365$  m) where the temperatures were measured. Also, little or no bed sliding is assumed for that part of the glacier, since velocities of  $\sim 2$ -3 m/year have been observed (Melvold and Hagen, 1998). By calculating a value of  $A$  from Equation 4.4, based on the surface slope and ice thickness at the location of the borehole in Björnsson et al. (1996), and assuming no bed sliding, it provides a comparison for the conditions on Høltedahlfonna. The calculated value of  $A = 1.0 \times 10^{-24} \text{ s}^{-1} \text{ Pa}^{-3}$  relates to an ice temperature between  $-5^\circ\text{C}$  and  $-2^\circ\text{C}$  for the recommended base values of creep parameter  $A$  in Cuffey and Paterson (2010). A calculation of the depth-averaged ice temperature for the entire temperature profile (K1) from (Björnsson et al., 1996) gives  $\bar{T} \approx -0.8^\circ\text{C}$ . By using the recommended base values for  $A$ , together with the calculated  $A$  from Kongsvegen, a sensitivity analysis of the deformation velocity was made.

### 4.3.2 Strain rate

The vertical strain rate  $\dot{\epsilon}_{zz}$  can be approximated with the continuity equation (Equation 3.6). Since all the GNSS receivers were located along the same flow line of the glacier, it is not possible to derive the lateral strain from the GNSS measurements. This means that only the longitudinal strain can be calculated. By assuming the lateral strain as zero and uniform distribution of the vertical strain, the vertical strain rate between two GNSS-stations can be estimated by

$$\dot{\epsilon}_{zz} = -\dot{\epsilon}_{xx} = -\frac{1}{l_0} \frac{\Delta l}{\Delta t} \quad (4.7)$$

representing the initial baseline between the stations ( $l_0$ ) at the beginning of a given time interval ( $\Delta t$ ) and the change in distance ( $\Delta l$ ) over the given time interval (Hoffman et al., 2011; Andrews et al., 2014).

Following the method from Anderson et al. (2004), the changes in ice elevation associated with longitudinal strain can be calculated by assuming a uniform distribution of the vertical strain and incompressible ice:

$$D_{\dot{\epsilon}} = -H_i \left( \frac{\Delta \bar{D}_x}{\Delta x} \right) = -H_i \left( \frac{\bar{D}_{x_{i+1}} - \bar{D}_{x_{i-1}}}{x_{i+1} - x_{i-1}} \right) \quad (4.8)$$

representing the mean horizontal displacement of a column of ice ( $\Delta \bar{D}_x$ ) covering a distance ( $\Delta x$ ) and the displacement of adjacent sites ( $\bar{D}_{x_{i\pm 1}}$ ) at their respective locations ( $x_{i\pm 1}$ ). This equation follows the continuity equation, and is used to calculate the changes in elevation at HDF2 due to lateral strain between HDF1 and HDF3.

### 4.3.3 Bed separation

The vertical motion  $w_s$  of the GNSS station includes the vertical component of the bed sliding, vertical changes due to ice strain and bed separation, and their relation is described in several studies (Hooke et al., 1989; Harper et al., 2007; Hoffman et al., 2011; Andrews et al., 2014):

$$w_s = u_b \tan(\alpha_b) + \dot{\epsilon}_{zz} H + \dot{c} \quad (4.9)$$

representing the horizontal bed sliding velocity ( $u_b$ ), the bed slope ( $\alpha_b$ ), the ice thickness at the GNSS station ( $H$ ), the rate of bed separation ( $\dot{c}$ ) including till dilation. From the assessment of the deformation velocity, the horizontal bed sliding velocity  $u_b$  was estimated. By using the calculated change in ice elevation due to ice strain ( $D_{\dot{\epsilon}}$ ), this gives the following relation for bed separation rate:

$$\dot{c} = w_s - (u_b \tan(\alpha_b) + D_{\dot{\epsilon}}) \quad (4.10)$$

The bed separation can be considered as cumulative, i.e. the level of bed separation from the previous interval is the starting level for the following interval.

As Hoffman et al. (2011) indicates, values for the glacier bed slope derived from ground-penetrating radar (GPR) measurements varies over different length-scales and the proper length

scale at which the bed slope is to be measured is not clear. Hoffman et al. (2011) used an approach where a background period with steady motion was used to calculate the bed slope, assuming zero bed separation and that the vertical motion due to bed-parallel motion and changes in surface elevation due to vertical strain was constant.

A similar approach as Hoffman et al. (2011) was used for these calculations. By defining a 7-day background period, where the horizontal and vertical surface velocities and the strain rates were steady, and assuming zero bed separation during this period, the bed slope was calculated from Equation 4.10 by using the mean values for  $w_s$ ,  $u_s$  and  $D_\varepsilon$  over this 7-day period. This approach is valid if the estimated changes in elevation due to vertical strain are reasonable. When using the estimates of the changes in elevation due to vertical strain between HDF1 and HDF3, this yielded unlikely estimates of bed separation. By adjusting the changes in elevation due to vertical strain  $D_\varepsilon$  to the level of the background period, i.e.  $\overline{D_\varepsilon} \approx 0$  in this period, the bed slope was calculated as above but using the adjusted value for  $D_\varepsilon$ . The estimated bed separation must be considered as indicative, due to the uncertainties of the bed slope and strain-related changes in elevation.

#### 4.3.4 Glacier runoff

In order to estimate the runoff on Holtedahlfonna, results from a re-run of the surface mass balance model from Van Pelt and Kohler (2015) was implemented in this study (W. Van Pelt, unpublished data). The simulated surface mass balance model in Van Pelt and Kohler (2015) had minor deviations from the observed stake mass balance, and the implemented subsurface routine made it possible to account for refreezing and firn water storage. One can thus expect the model to give reasonable estimates of the amount of meltwater not being temporarily stored in the subsurface, i.e. runoff. An estimation of the runoff rate every 3 hours makes it possible to compare the motion of the GNSS stations to the amount of water that can drain to the glacier bed.

The original model used meteorological data from the HIRLAM regional climate model as climate forcing, but since the latter data was unavailable for the current year (2015), meteorological data from a station in Ny-Ålesund provided climate forcing to the model (W. Van Pelt, personal communication, 2015). The re-run of the climate model must be regarded as an experiment, compared to the original model in Van Pelt and Kohler (2015), and the change in forcing creates a larger uncertainty in the outputs of the surface mass balance model, including the cumulative runoff. To create a smooth transition between the regional climate model time-

series and the Ny-Ålesund data, biases were corrected at sea level (Van Pelt, personal communication, 2015). The absolute accuracy is thus uncertain over a mass balance year. However, it can be assumed that the relative temporal variations in the runoff are good enough for this study.

The model simulates the runoff for  $100 \text{ m} \times 100 \text{ m}$  grid cells on the entire glacier, with a unit of  $\text{m w.e. m}^{-2} 3\text{h}^{-1}$ . The total runoff was calculated for all areas above the elevation of station HDF1 on Høltedahlfonna (Figure 4.4), with a unit of  $\text{km}^3 3\text{h}^{-1}$  (Appendix 9.1). The estimated runoff values are supplemented with observations of precipitation and air temperature in Ny-Ålesund (eKlima, 2015) and air temperature from the AWS at HDF2 on Høltedahlfonna (J. Kohler, unpublished data).

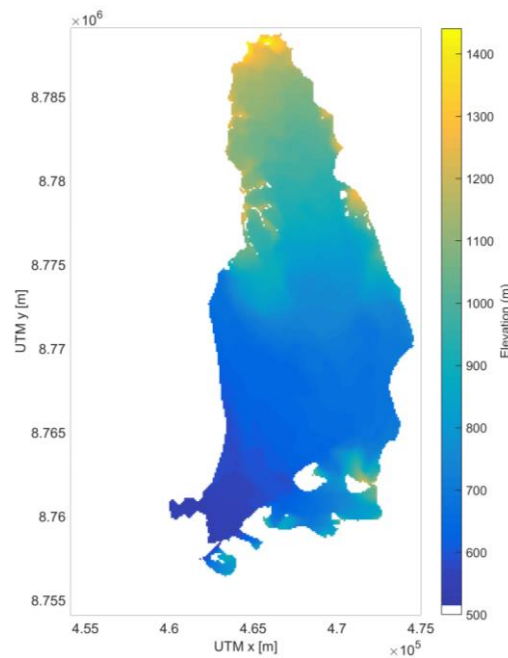


Figure 4.4. Elevations above HDF1 on Høltedahlfonna. The DEM is from NPI (2014).

#### 4.3.5 Identification and quantification of supraglacial lake

The surface mass balance model estimates the melt-water production on the glacier, but does not take into account supraglacial flow-routing and lake formation. To evaluate the changes in the surface hydrology, panchromatic scenes from the Landsat 8 satellite from the summer melt season were manually inspected (NASA/USGS, 2015). The panchromatic scenes have a spatial resolution of  $15 \times 15 \text{ m}$ . Minor shifts between the images were corrected using a georeferencing tool in ArcMap (ESRI, 2015), with stable ground as control points, before digitizing the lake outlines at the different dates.

A 5×5 m resolution DEM from aerial photography from 2009 (NPI, 2014) is available for this area, and was used to estimate the volume of a prominent supraglacial lake. The elevation values from the DEM were extracted along the lake outlines, and the mean elevation value  $\pm 1$  standard deviation, in addition to the mode of elevation values using 0.25 m bin width were calculated. The volume of the lake was calculated by multiplying the pixel resolution with the vertical distance from the determined lake surface level to each pixel on the glacier surface and by adding each resulting pixel value for the entire lake area. Since this was done for both the mean,  $\pm 1$  standard deviation and the mode of elevation values, the range of volumes illustrate the uncertainties of the estimates.

#### 4.4 Statistics and uncertainty

The variability in the estimated positions can be assessed by calculating the standard deviation (Kreyszig, 2010):

$$\sigma = \sqrt{\frac{1}{n} \sum_{j=1}^n (x_j - \bar{x})^2} \quad (4.11)$$

representing the number of measurements ( $n$ ), the value of each coordinate ( $x_j$ ) and the mean value of all measurements ( $\bar{x}$ ). To analyze the variation in the kinematic positions from a moving average, the moving standard deviation windowed around each coordinate  $x_i$  was computed by

$$\sigma_i = \frac{1}{2n+1} \left[ \sum_{j=i-n}^{i+n} x_j^2 - \frac{1}{2n+1} \left( \sum_{j=i-n}^{i+n} x_j \right)^2 \right]^{\frac{1}{2}} \quad (4.12)$$

representing the number of measurements in each direction in time for each coordinate ( $n$ ) and the time ( $i$ ) of the coordinate  $x_i$  that is to be calculated (Scholkmann et al., 2010). To compare the overall variation of each method, the mean running standard deviation was calculated for the different time-series. The resulting mean values supplement the qualitative comparison of the results, and are just a simple measure of the variation from the respective running average.

The uncertainty of the static position of HAGN, averaged over the 14 daily solutions, was calculated with the standard error (Devore and Berk, 2007):



$$SE = \frac{\sigma}{\sqrt{n}} \quad (4.13)$$

representing the standard deviation of the daily solutions ( $\sigma$ ) and the number of daily solution ( $n$ ). Since a certain correlation between the daily solutions is assumed (Hollenstein et al., 2003), the value for  $SE$  can be expected to be optimistic.

In order to give an estimate of the uncertainty of an estimated kinematic position averaged over an interval length of 1, 2, 3 or 24 hours, one must consider the correlation between the kinematic solutions, since they are dependent over a certain period (Hofmann-Wellenhof et al., 2008).

Also, the constant motion of the glacier means that no constant reference point or long-term mean position can be used. However, by using the kinematic solutions of the fixed HAGN station, using NYA1 as a base station, uncertainties of the moving average filtered position time-series for the stations on the glacier can be estimated.

The HAGN solution from the 7-day test period was separated into discrete 1-, 2-, 3- and 4-hour intervals, and mean values for the horizontal and vertical positions of each discrete interval were calculated. To find the variation in mean values of the discrete intervals from the 7-day average value, the standard deviations of the mean values of each interval length were calculated. The resulting values can thus be used as an estimate of the uncertainty for a given point on the moving average filtered position time-series. The horizontal uncertainty is calculated by combining the vectors of the standard deviations for the north ( $N$ ) and east ( $E$ ) components:

$$\sigma_{hor} = \sqrt{\sigma_N^2 + \sigma_E^2} \quad (4.14)$$

To better illustrate the differences between the results in the test-period, a combined three-dimensional vector of the internal accuracies given by the software was calculated by

$$\sigma_{3D} = \sqrt{\sigma_N^2 + \sigma_E^2 + \sigma_U^2} \quad (4.15)$$

representing the north ( $N$ ), east ( $E$ ) and vertical ( $U$ ) components.

## 5 Results

The results are presented in two main sections:

1. The results from the GNSS post-processing of the test period
2. The glacier motion during the entire study period for all stations on the glacier, derived from the preferred GNSS post-processing routine. The section focuses both on the long-term seasonal development and short-term events of interest, and includes meteorological data, estimated runoff from the surface mass balance model and observed changes in the surface hydrology for the interpretation of the GPS-derived glacier motion.

### 5.1 Comparison of GPS/GNSS post-processing methods and software

Preliminary results of the motion of the GNSS stations were used to determine the timing of the test period, with a set prerequisite of containing periods with horizontal surface velocities similar to those in winter and at the same time including events of acceleration and peak surface velocities. The period July 7-13 2015 was thus chosen, since it fulfills the prerequisite, covering steady low surface velocities in the beginning of the period, together with large horizontal- and vertical displacements towards the end. The large range of displacements enables the suitability of each method to be evaluated. This is especially true for the pseudo-static processing, since the displacement of the GNSS station on the glacier increases together with the interval observation length, and this can lead to problems in the ambiguity resolution during the post-processing.

The estimated mean coordinates of HAGN are given in Table 5.1. The uncertainties of the averaged coordinates are expressed by the standard error, but show an optimistic uncertainty since a certain correlation between the daily solutions can be expected (Hollenstein et al., 2003).

Table 5.1. Cartesian coordinates of HAGN and NYA1

Station	Cartesian coordinates [m]			Uncertainty [m]		
	x	y	z	$\sigma_x$	$\sigma_y$	$\sigma_z$
HAGN	1210601.5893	281761.0852	6235436.2160	0.0006*	0.0002*	0.0022*
NYA1	1202433.6930	252632.3680	6237772.7070	0.0010	0.0010	0.0010

\* The uncertainties of HAGN are from the calculated standard error of the 14-day average (4.13). All coordinates are given in Appendix 9.2.

The baselines have an average length of 30342.312 m with a standard deviation of 0.6 mm, and the mean internal accuracy of each measurement given by the software was 2.0 mm, 1.6 mm, 9.4

mm and 1.6 mm for the x, y, z and length component, respectively. A detailed overview of the averaged coordinates and statistics is given in the Appendix 9.2.

The two next sections will compare the results from both kinematic and pseudo-static post-processing, for the different software packages, methods, satellite systems and network configurations. The results from the test period were subsequently used to determine the optimal technique for processing the winter and summer data.

### 5.1.1 Pseudo-static

The results from the static processing of HDF1 (Figure 5.1) show the effect of reducing the observation time from 3 hours down to 30 minutes using GPS+GLONASS for relative positioning (RTKLIB) and PPP, and only GPS using relative positioning (GAMIT). The test period includes an event of sudden rise in the elevation values, together with larger horizontal displacements, i.e. higher surface velocities, starting on July 11<sup>th</sup>. In relation to this event, it can also be observed a change in the horizontal trajectory, where the GNSS station takes a more southerly path before returning to the ‘long-term’ southwesterly path. This pattern is visible in all results from the pseudo-static processing, and as we can see in the next section, it can also be observed for the kinematic processing. Thus, the variation of the vertical positions needs to be assessed qualitatively.

For all used methods, the variation in horizontal and vertical positions increases as the interval length decreases from 3 hours to 30 minutes. The method that has the smallest lateral variation in the horizontal positions for all interval lengths are the results from RTKLIB, using both GPS and GLONASS satellites. At least one occasion of processing artifacts is evident both on the 1- and 0.5-hour interval, but not for the 2- and 3-hour interval, for RTKLIB on July 12<sup>th</sup>. RTKLIB has the smallest increase in variation in the vertical positions when decreasing the interval lengths from 3 hours to 1 hour, and have roughly the same vertical variation as the PPP solution on the 30-minute interval. The deviation from the original horizontal path gets solved differently depending on the interval length and processing method. The GAMIT solutions, only based on GPS satellites, have rather small variations in the horizontal and vertical for the 3- and 2-hour intervals, but the variation increases significantly when reducing the interval lengths to 1 hour and especially 30 minutes. Similar to the GAMIT solution, the results from PPP show significantly larger variation when reducing the interval length to 1- and 0.5 hours. Common for all results is that the 2-hour intervals seem to be the optimal result when considering the

variation of the measurements and its potential to capture the short-term changes in the horizontal and vertical displacements.

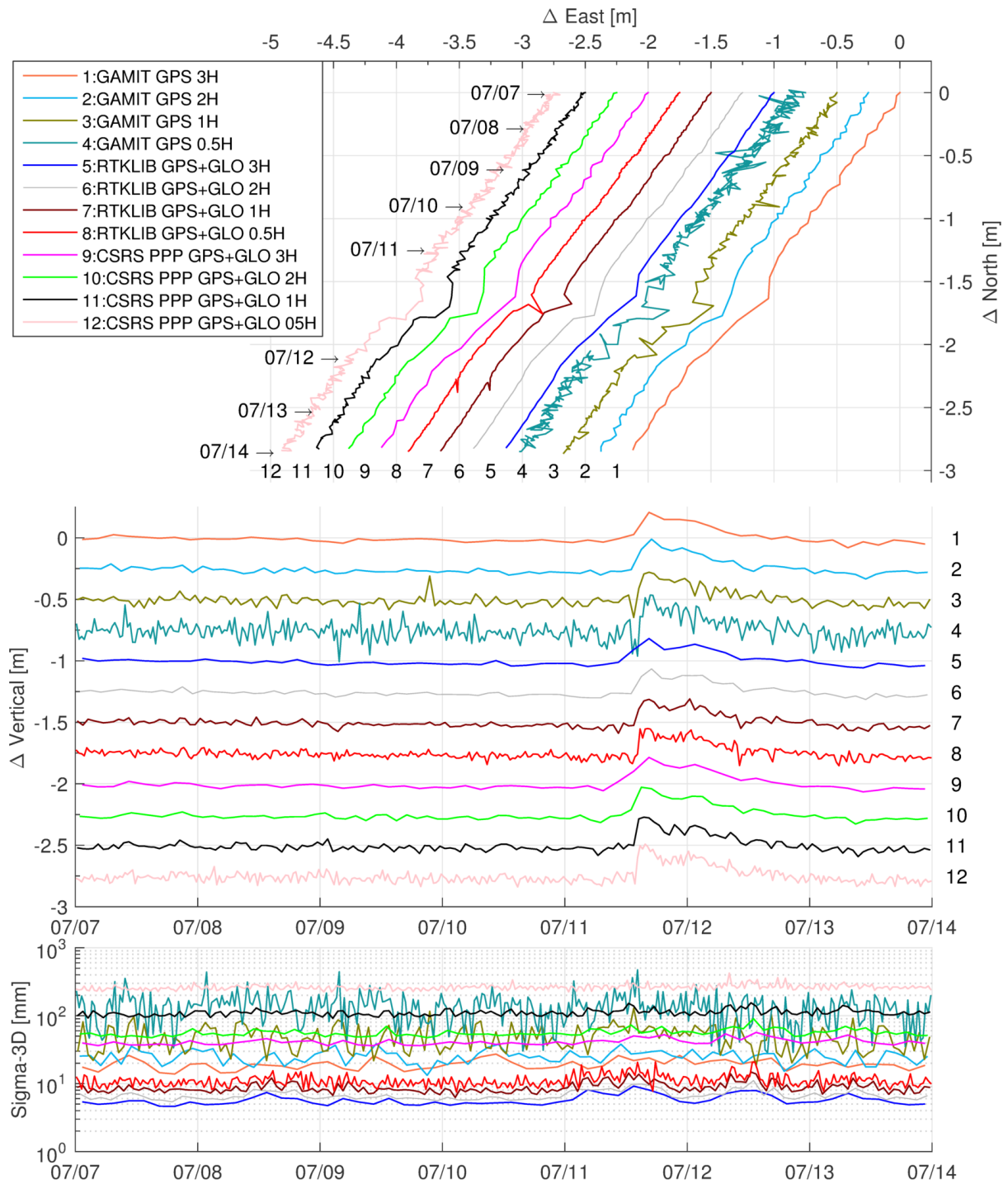


Figure 5.1. Combined plot of the pseudo-static horizontal and vertical positions and the internal accuracy given by the respective software ( $\Sigma$ -3D). The legend refers to the color and number of each interval and software.

The variation in the three-dimensional vector of the internal accuracies given by the software was large for the different results, and ranges between  $\sim 2.5$  mm for the RTKLIB 3-hour solution and  $\sim 173$  mm for the GAMIT 0.5-hour solution.

### 5.1.2 Kinematic

The comparison between kinematic relative positioning in RTKLIB and TRACK and kinematic PPP is presented in Figure 5.3. For a quantitative comparison of the short-term variation in the vertical positions of the different results from a 3-hour running average, the mean 3-hour moving standard deviation for the entire period is included in Figure 5.2.

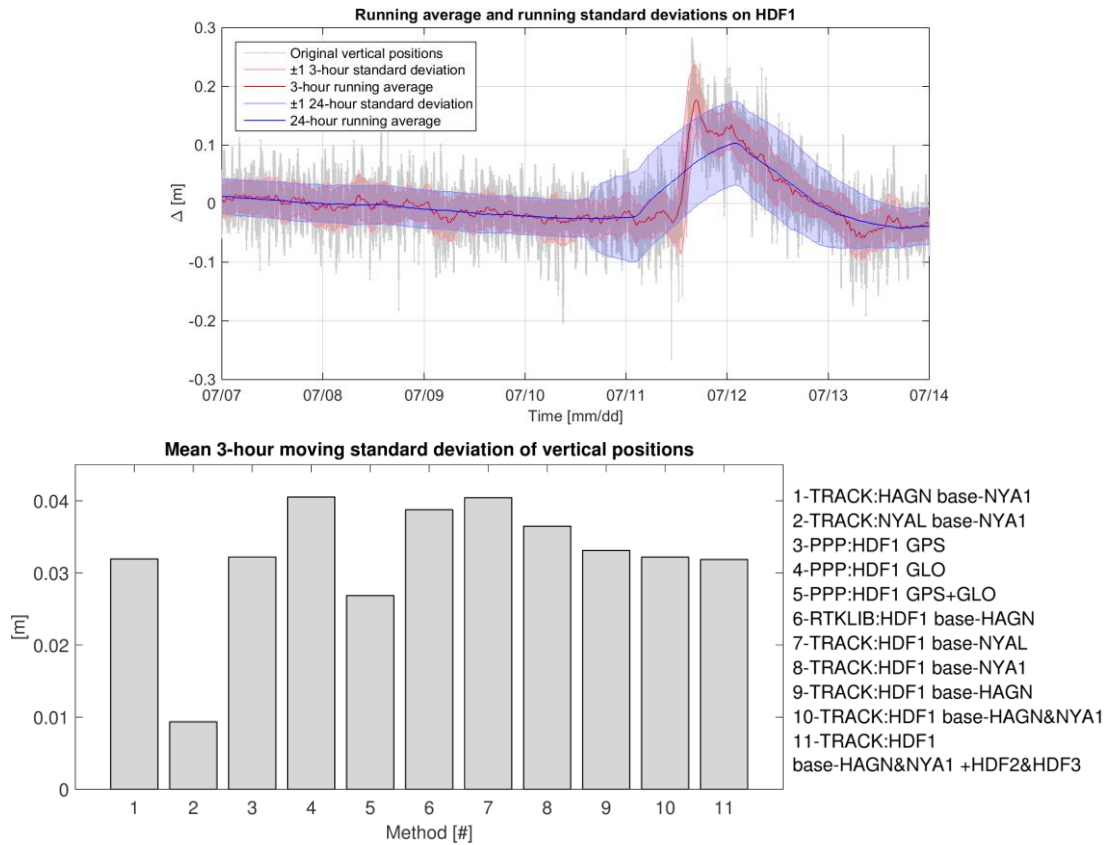


Figure 5.2. Upper: 3- and 24-hour running average and  $\pm 1$  3- and 24-hour running standard deviation of vertical position of HDF1 from the network solution in TRACK (test 11). The plot illustrates how the length of the interval affects the running standard deviation. Lower: Mean 3-hour running standard deviation over the entire test period for the methods presented in the legend and in Figure 5.3.

In TRACK, the different setups using single and multiple base stations, together with one or more rovers on the glacier, resulted in slightly different results. The estimated positions of HAGN, processed in kinematic mode using NYA1 as a base station (test 1), illustrates the horizontal and vertical variation for a fixed location. The estimated vertical positions of HAGN has a mean 3-hour running standard deviation of  $\sim 3.1$  cm. This is the observed variation in the vertical positions processed in kinematic mode when using relative positioning for GPS only with a single base station at a  $\sim 30$  km distance and 470 m difference in elevation. The results from this test can be compared with the results from using NYA1 or NYAL as a single base station when processing HDF1 on the glacier. The results from using NYA1 and NYAL as a

base stations (test 7 and 8 in Figure 5.3) are similar, but the solution using NYAL shows a larger variation and possible artifacts during July 11<sup>th</sup>, and has a slightly larger mean 3-hour running standard deviation. When using HAGN as a base, the solutions has a smaller variation from the running mean and less outliers are present. When including NYA1 as a second base station, the variation gets reduced even more. The best result from TRACK, in terms of the vertical variation from the 3-hour running mean, is achieved by processing in network using HAGN and NYA1 as base stations, with all three stations on the glacier as rovers.

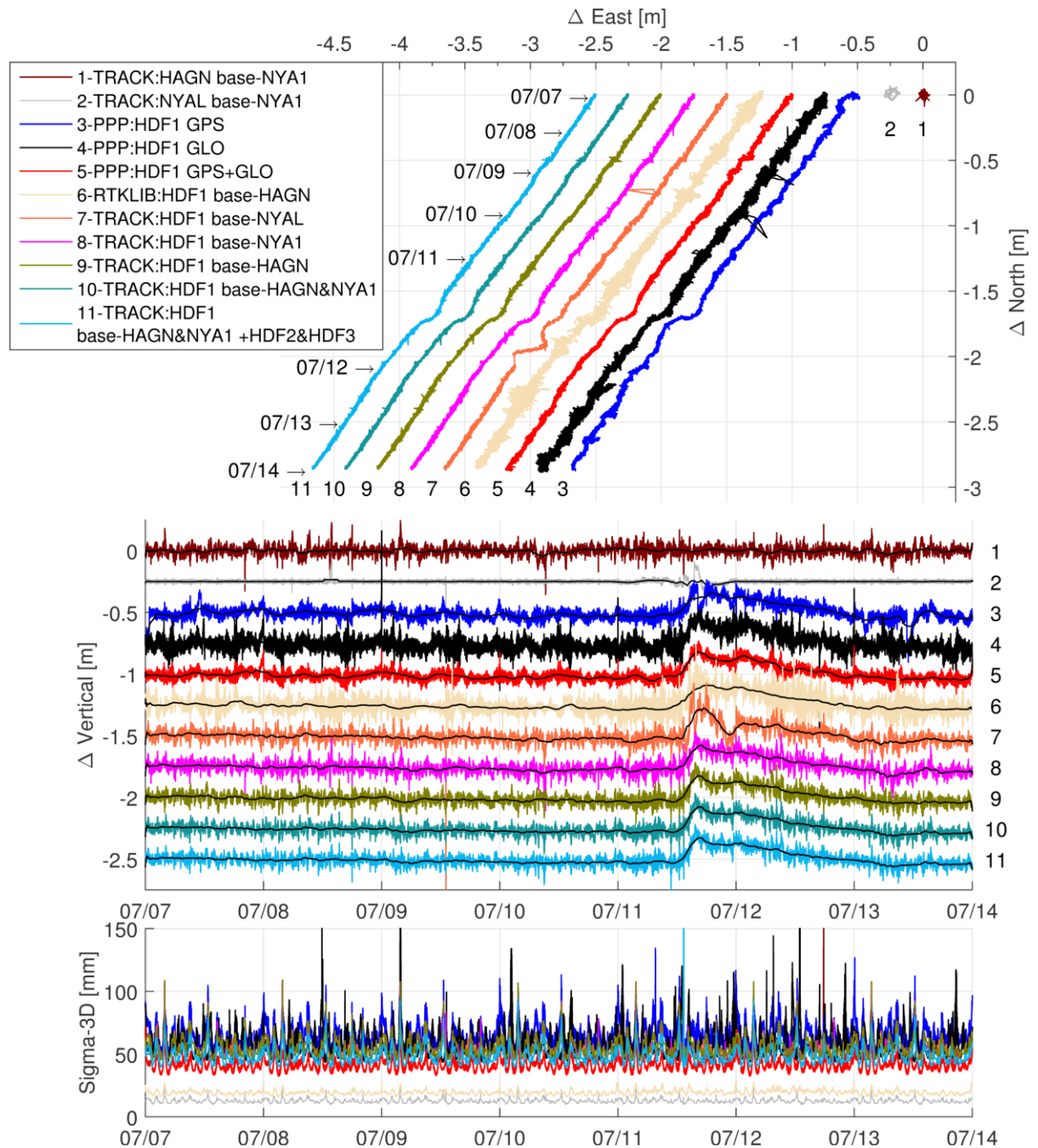


Figure 5.3. Combined plot of the horizontal and vertical positions and the internal accuracy given by the respective software ( $\Sigma$ igma-3D). The legend refers to the color and number of each method and software. Test 2 used the L1+L2 technique for the NYA1-NYAL baseline.

The estimated positions from PPP using only GLONASS satellites have large variations and considerable outliers both in the horizontal and vertical direction. The results from using only GPS satellites has less variation, but the best is achieved by using both GPS and GLONASS satellites. The latter solution has the smallest mean 3-hour running standard deviation of all the test results of HDF1. However, as illustrated in Figure 5.3, an undulating pattern in the vertical positions is visible in all PPP solutions. The same pattern is not visible to the same degree in the solution from relative positioning. It was discovered in the CSRS PPP result files that the processing sessions rejected the provided OTL corrections in the BLQ format (Bos and Scherneck, 2011). By acquiring a new set of OTL corrections with the HARPOS format (Bos and Scherneck, 2011), the data was re-processed. The difference between the solutions with and without the OTL corrections were up to 1 cm, but did not match the scale of the observed undulations observed in Figure 5.3.

The RTKLIB solution shows large variations in both horizontal and vertical direction, with large outliers and also several epochs with float solution where the software was unsuccessful in fixing the ambiguities. The float solutions are removed in the final test results (Figure 5.3). The mean 3-hour running standard deviation is, however, similar to the results from relative positioning in TRACK using NYAL as a base station.

The results for the NYA1-NYAL baseline (test 2 in Figure 5.3) from relative positioning in TRACK using the L1+L2 technique show a very low variation in the vertical positions, except for a major artifact on July 11<sup>th</sup>. This method has the lowest mean running standard deviation of all the test results (Figure 5.2). When applying the same technique on HDF1 with HAGN as base station, the estimated positions had far larger variation and a significant amount of outliers. The results for this test have not been included in Figure 5.3, due to the large spread in estimated positions.

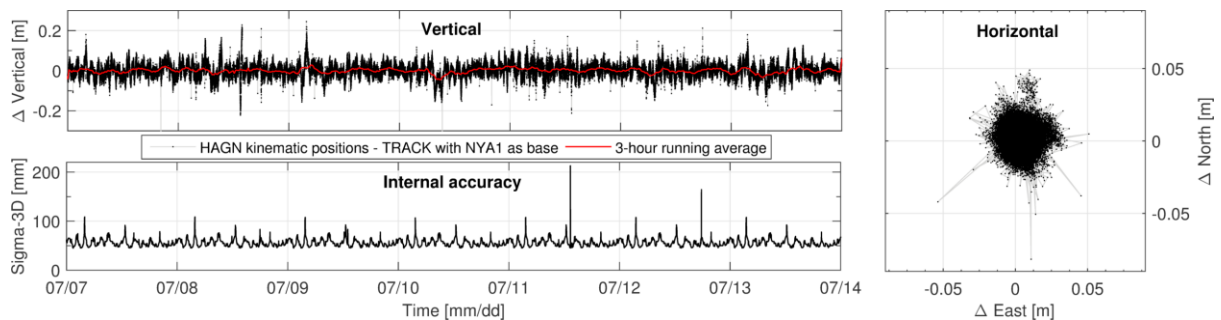


Figure 5.4. 24-hour solutions over 7 days in the test period, for HAGN using NYA1 as base station (TRACK). The combined plot shows the vertical and horizontal positions, as well as the internal accuracy given by the software.

The 1210960 estimated positions in the 7-day time-series for HAGN (Figure 5.4) have standard deviations of 9 mm and 35 mm in the horizontal and vertical directions, respectively. In other words, 95% of the positions were in the range of  $\pm 17.6$  mm and  $\pm 68.6$  mm from the overall mean in the horizontal and vertical directions, respectively. The calculated uncertainties for HAGN was then used as an approximation of the uncertainties of the GNSS station on the glacier. The average internal accuracy given by TRACK for the HAGN solution was 19 mm and 52 mm in the horizontal and vertical directions, respectively. This compares to 17 mm and 46 mm for the HDF1 network solution (HAGN, NYA1, HDF1, HDF2 and HDF3), respectively.

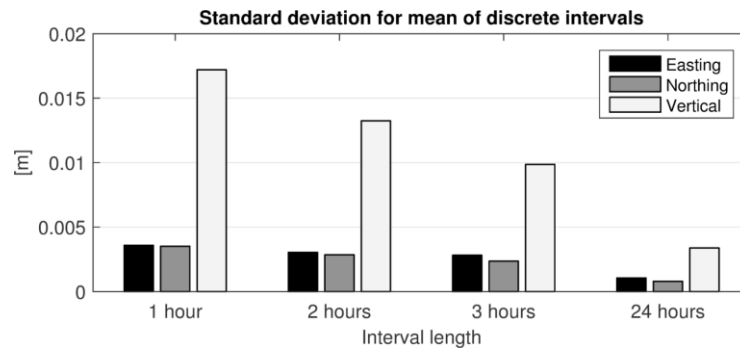


Figure 5.5. Standard deviation for the mean northing, easting and vertical coordinates for discrete intervals of 1-, 2-, 3- and 24-hour lengths, over the entire 7-day test period. The bar plot illustrates how the variation around the over mean decreases when averaging over longer intervals.

The standard deviation of the mean of discrete intervals of the kinematic HAGN solution (Figure 5.5) show that the variation between the discrete intervals decrease when the interval length increases. The combined horizontal components from Figure 5.5 are given in Table 5.2

Table 5.2. The estimated uncertainties for running average filtered position time-series at given time intervals.

	1 hour	2 hours	3 hours	24 hours
Horizontal [mm]	5	4	4	1
Vertical [mm]	17	13	10	3

## 5.2 Glacier motion

Based on all results from the test period, the solution in TRACK using HAGN and NYA1 as base stations in network with all stations on the glaciers, was found to be the solution that can most precisely estimate the true horizontal and vertical motion of the GNSS stations on the glacier. When comparing to the pseudo-static solutions, the method was also the preferred choice when trying to evaluate the short-term changes occurring during the summer season, exemplified with July 11<sup>th</sup> in the test period. Thus, the network setup in TRACK was used to process the entire summer season for HDF1-2-3, as presented in this next section.



Based on the pseudo-static test results, RTKLIB would be the preferred method when processing 2 hours of data in static mode, which is the observation interval during winter for HDF1 and HDF3. However, when evaluating the results from RTKLIB pseudo-static and TRACK kinematic, both using NYA1 as a base station, the 2-hour average of the TRACK solution has less variation and outliers in both the horizontal and vertical (Figure 5.6) positions. Thus, TRACK was also the preferred method when processing the winter data, and the estimated positions were averaged over the daily 2-hour observation interval.

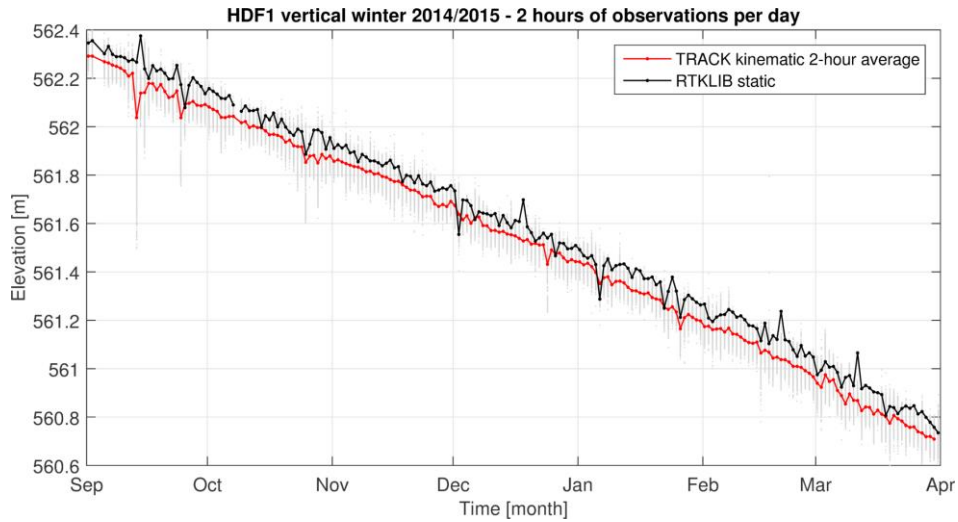


Figure 5.6. The grey dots show the original kinematic solution from TRACK, with the red dotted line marking the mean vertical value of the 2-hour daily intervals. The black dotted line is the static RTKLIB solution, and shows a large variation than the average values from TRACK.

For the internal deformation at HDF2, the sensitivity analysis shows how various values for the creep parameter ( $A$ ) and shape factor ( $f'$ ) affects the estimates of the deformation velocity (Figure 5.7). With the assumption of a similar temperature regime at HDF2 and K1 (Björnsson et al., 1996), both located below the ELA, and a shape factor of  $f'=0.9$ , this yields a deformation velocity of approximately 3 mm/day. Given a larger creep factor  $A$ , i.e. the mean ice temperature is expected to be higher at HDF2 than K1, the deformation velocity increases to approximately 5 mm/day (with  $f'=0.9$ ,  $A=1.7E-24$ ). Thus, based on an observed background surface velocity at HDF2 of around 170 mm/day (presented in the next section), the deformation velocity is comparatively small due to the small surface slope, and changing the  $A$  and  $f'$  factors have minor effects on the deformation velocity. The deformation velocity was thus considered as negligible when assessing the bed sliding velocity, yielding  $u_s \approx u_b$  in the bed separation calculation (4.10).

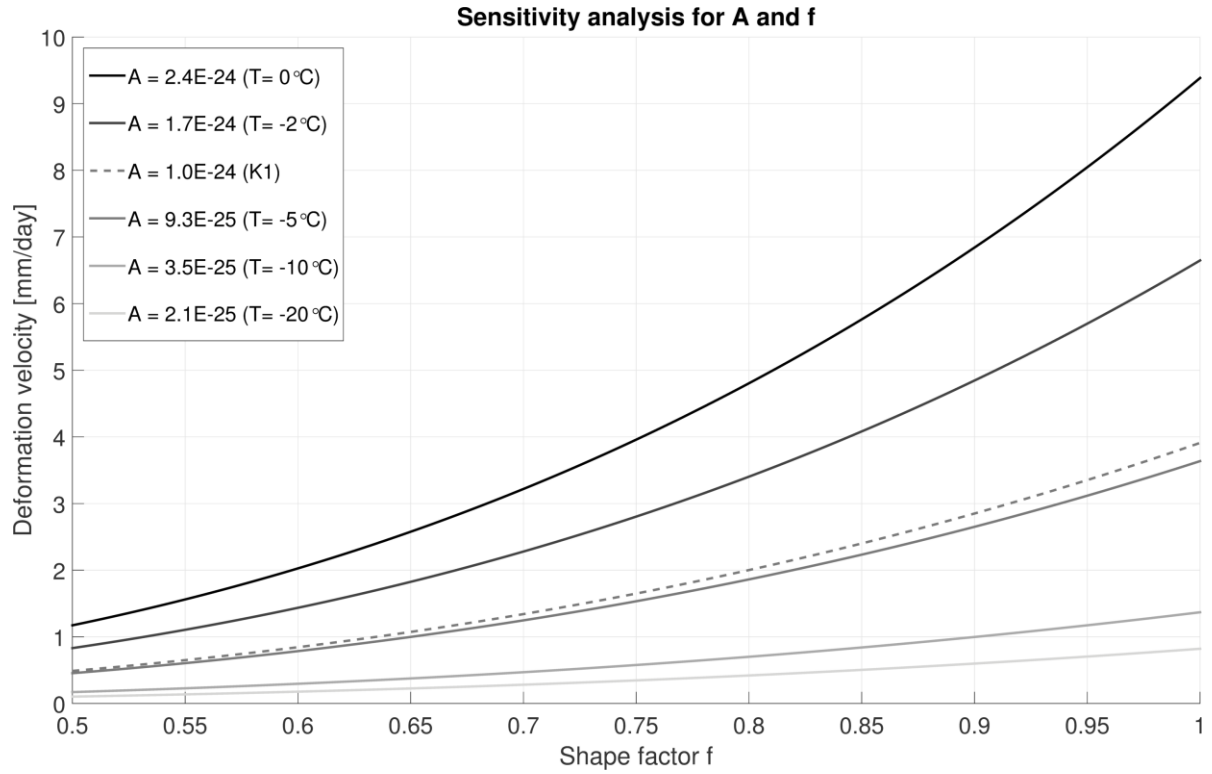


Figure 5.7. Sensitivity analysis for deformation velocities at HDF2 for different values of the creep parameter  $A$  and the shape factor  $f$ . Included parameters in the calculation were  $n=3$ ,  $\rho=917 \text{ kg m}^{-3}$ ,  $\bar{H}=511 \text{ m}$ ,  $\bar{\alpha}_s=0.7^\circ$  in Equation 4.4. K1 denotes the  $A$  value calculated from the surface slope and ice thickness at the borehole K1 at Kongsvegen (Björnsson et al., 1996), assuming no bed sliding.

### 5.2.1 Winter and summer season 2015

While HDF1 made observations during the entire winter season, HDF3 experienced a data gap between the end of November to the beginning of March, after which the station automatically turned back on and started logging. Thus, the data gap during the polar night was probably related to depleted batteries. As Figure 5.8 illustrates, the estimated positions from the daily 2-hour intervals during winter show a larger inter-daily variation with more outliers, when comparing to the summer results. This variation in the horizontal positions thus leads to a larger spread in the daily horizontal surface velocities, and possible short-term changes in the glacier motion are harder to identify.

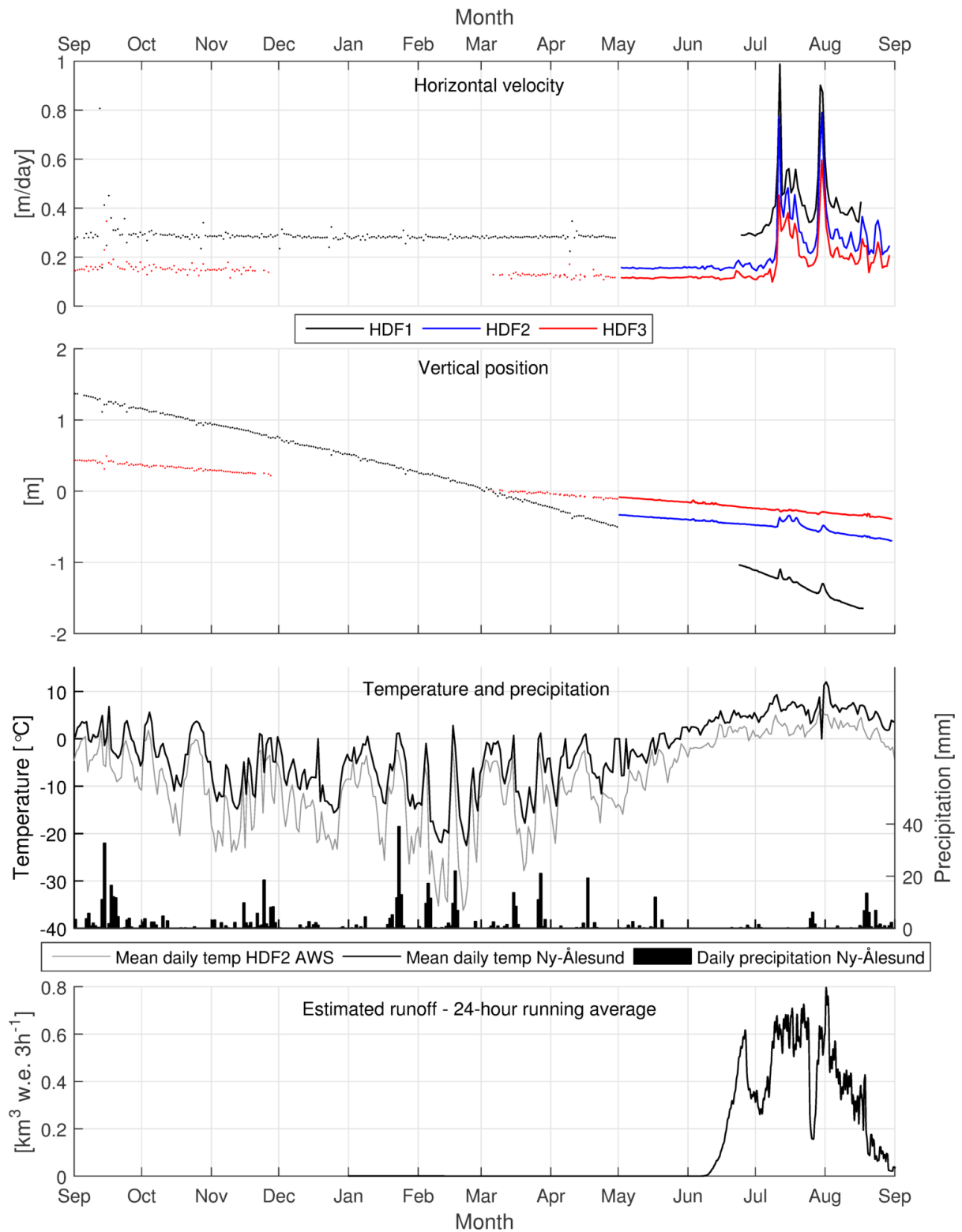


Figure 5.8. Combined plot of the glacier motion, temperature, precipitation and estimated cumulative runoff, between September 2014 – September 2015. The 24-hour running average vertical positions have been normalized to better compare the results from the different stations. The horizontal velocities are calculated from 24-hour intervals. The color of the markers (dots) for the horizontal velocity and vertical positions during winter correspond to the summer results (lines) for each station. The runoff is estimated from January 1<sup>st</sup> 2015. Meteorological data from Ny-Ålesund (eKlima, 2015) and temperature from HDF2 AWS (J. Kohler, unpublished data).

During the winter of 2014/2015, an overall background velocity for HDF1 of  $\sim 0.28$  m/day can be observed. During September 2014, significant variation in the positions of HDF1 can be observed, leading to large horizontal variations. For HDF3, the daily velocities from September to the end of November 2014 ( $\sim 0.15$  m/day) are slightly higher than in March and April 2015 ( $\sim 0.12$  m/day), after the data gap.

In May, when the mean daily temperatures are below zero degrees at the AWS at HDF2 and the surface mass balance model estimated no runoff from the area above HDF1, the horizontal surface velocities and vertical motion remained almost constant. During the first half of June, the surface mass balance model estimates the onset of the summer melt water production, and the motion of the two observing GNSS stations started showing slight variations. As the HDF1 started to make observations after the data gap in May and most of June, the horizontal surface velocities start to gradually increase before a rapid acceleration in the horizontal surface velocities at all three stations and elevated vertical positions at HDF1 and HDF2 can be observed.

### **5.2.2 Summer season 2015**

Due to the data gap for HDF1, all stations on the glacier only had continuous overlapping observations in the period July 24<sup>th</sup> – August 17<sup>th</sup>. All calculations related to strain rates and bed separation have thus been calculated for this period.

As illustrated in Figure 5.9, there are two major speed-up events during the summer season. The horizontal surface velocities and vertical motion of all three stations are relatively constant in the period leading up to the first event, initiated on July 11<sup>th</sup>, with slightly increasing horizontal surface velocities for HDF1. On July 11<sup>th</sup>, a sudden acceleration in the horizontal surface velocities occurred simultaneously on this time-scale at all stations, with increasing values from HDF3, HDF2 and HDF1, respectively. Increases in the vertical positions were initiated simultaneously with the acceleration at HDF1 and HDF2, while HDF3 initially show slightly elevated before experiencing a lowering in the vertical positions (when comparing to the trend prior to the event). The elevated positions were sustained over a two-week period for HDF1 and HDF2, and while HDF1 experienced the largest increase in the elevations during the initial hour of the event, HDF2 sustained the largest elevated values during the two-week period.

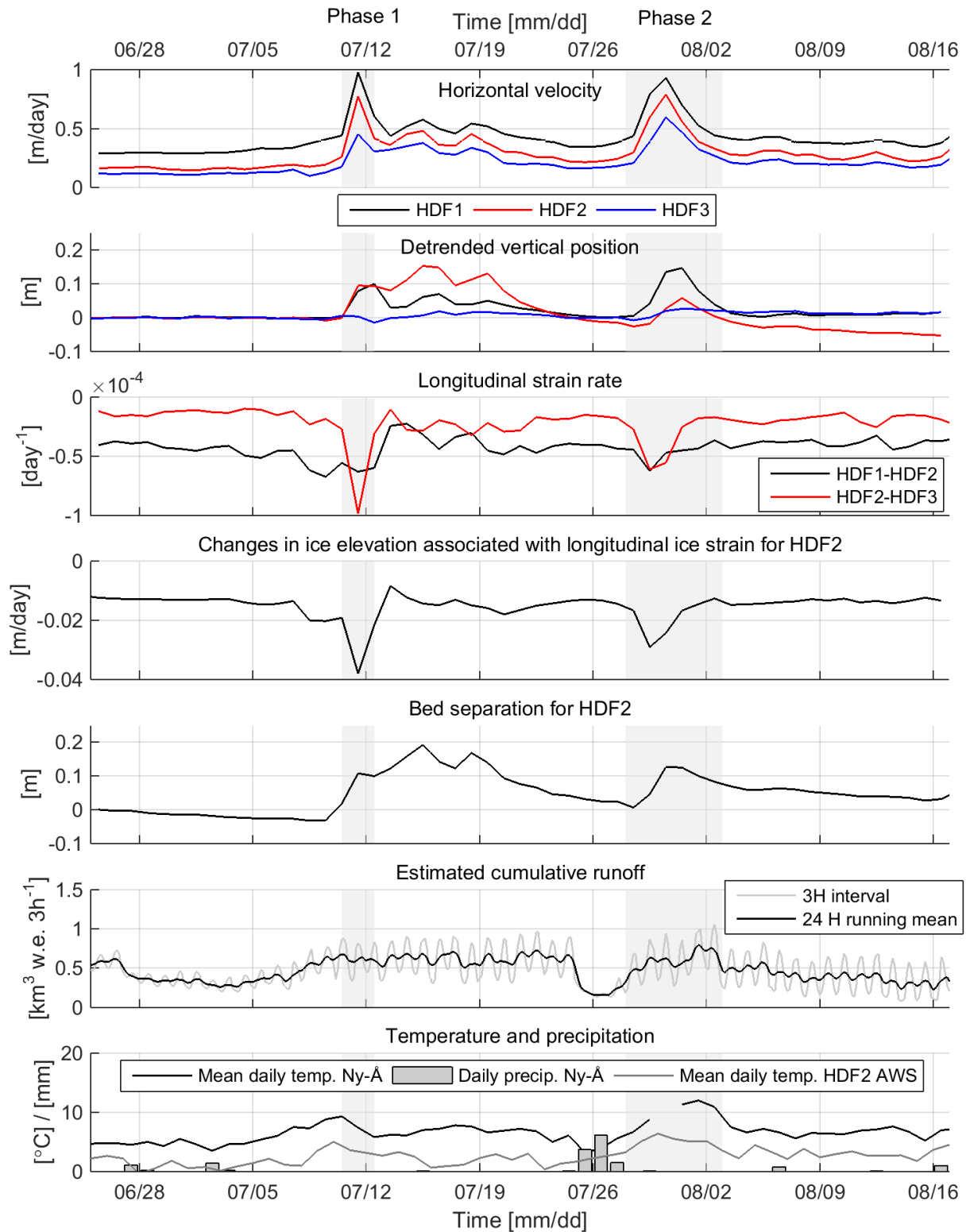


Figure 5.9. A combined plot for the summer season data. The horizontal velocity, de-trended vertical positions, longitudinal strain rate, changes in elevation for HDF2 due to vertical strain (derived from the longitudinal strain between HDF1 and HDF3) and the estimated bed separation are calculated at 24-hour intervals. The estimated runoff is summed over the all elevations above HDF1. Meteorological data from Ny-Ålesund (eKlima, 2015) and temperature from HDF2 AWS (J. Kohler, unpublished data).

The second major event was initiated on July 27<sup>th</sup>, with more or less simultaneous increases in surface velocities at all stations followed by elevated vertical positions. The acceleration and

deceleration phase is different from the first major event, with a more gradual increase and later on decrease in both the horizontal surface velocities and change in vertical positions. As Figure 5.9 illustrates, the de-trended vertical positions of HDF1 and HDF3 follows the trend line from the initial 14 days of the period, while HDF2 ends up below the initial trend.

Overall negative longitudinal strain rates can be observed between HDF1-HDF2 and HDF2-HDF3 during the entire period, and is due to the constant difference in horizontal surface velocities. Thus, the most negative longitudinal strain rates are found between HDF1-HDF2, since the difference in velocity is largest between these two stations. This means that all additional longitudinal strain rates related to the events during summer must be evaluated from these negative background levels. Prior to the first major event, the slightly increasing horizontal velocities at HDF1 led to larger negative strain rates between HDF1-HDF2, since the velocities at HDF2 did not increase with the same rate. At the onset of the first event, the initial acceleration at HDF2 led to large positive longitudinal strain rates before the acceleration at HDF1 also was initiated. As the velocities increased significantly at HDF1, the longitudinal strain experienced an opposite shift, with large negative values. For HDF2-HDF3, the large increase in horizontal velocities at HDF2, compared to the smaller increase at HDF3, led to negative longitudinal strain rates, and occurred simultaneously as the vertical lowering at HDF3.

In the period after the first major event, the longitudinal strain rates experiences various smaller variations between both station pairs, due to the variable surface velocities at all three stations. The strain rates are more or less back to the background level before the second major event. During this period, the largest and second largest increases in velocities can be observed at HDF1 and HDF2, respectively, leading to the negative strain rates between both HDF1-HDF2 and HDF2-HDF3.

Since HDF2 is in between HDF1 and HDF3, it is possible to estimate the changes in elevation at HDF2 related to the longitudinal strain between HDF1 and HDF3 Equation 4.8. As described above, the increasing horizontal surface velocities down-glacier from HDF3 leads to a constant negative longitudinal strain, indicating a constant dynamic lowering at HDF2. During both events, the derived longitudinal strain rates indicate a considerable lowering of HDF2, with the largest magnitude during the first major event.

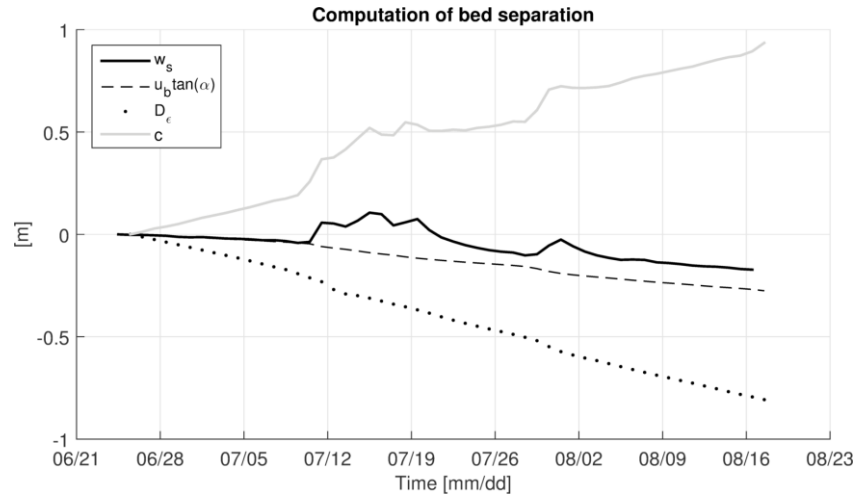


Figure 5.10. Plot of the observed vertical motion  $w_s$ , the vertical component of bed sliding  $u_b \tan(\alpha_b)$ , the change in elevation due to vertical strain  $D_\epsilon$  and the bed separation  $\dot{c}$ . The plot illustrates how the estimated changes in  $D_\epsilon$  leads to unlikely estimates bed separation. The bed slope is here estimated to  $1^\circ$ , which is in the mid-range of the measured distance-dependent values for the bed slope around HDF2.

The estimated bed separation presented in Figure 5.9 are based on the adjusted values for the change in elevation due to vertical strain, and can thus be considered as indicative. The estimated bed separation is slightly negative prior to phase 1, before a rapid uplift is estimated at the onset of phase 1. The bed separation reaches a maximum value of  $\sim 20$  cm in the following week, before gradually declining. During phase 2, the estimated bed separation reaches a level of  $\sim 12$  cm. Figure 5.10 illustrates the estimated bed separation from using the original estimated changes in elevation due to vertical strain and a measured bed slope of  $1^\circ$  (facing downglacier). Due to the large rate of estimated lowering of the surface at HDF2, the resulting bed separation is estimated to increase up to a level of  $\sim 1$  m at the end of the summer season. The estimated bed separation deviates significantly from the observed vertical motion of HDF2.

The surface mass balance model indicates that the melt water production has already started at the beginning of the period in Figure 5.9, with steady low values for the first week. With increasing temperatures in Ny-Ålesund in the following week, leading up to temperatures  $5^\circ\text{C}$  higher than the week before, the model estimates a significant increase in runoff. While the surface velocities and vertical position remain more or less constant during the first week, the slight increase in surface velocity at HDF1 and variation in the velocities at HDF2 and HDF3 indicates that the glacier is starting to react to the estimated increased melt water production. The estimated runoff peaks out around July 10<sup>th</sup> and remains on a constant high level until July 25<sup>th</sup>, when a drop in temperature and precipitation can be observed in Ny-Ålesund. July 26<sup>th</sup> has the minimum estimated runoff for the entire period, and the horizontal surface velocities and vertical motion for all three stations in the days before and after this date are similar to the conditions during the first week of the entire period. Following is a week of significant increases

in temperature, which results in a fourfold increase in estimated runoff between July 26<sup>th</sup>-August 1<sup>st</sup>. The second major event was initiated 3 days after the minimum estimated runoff, thus occurring during the period of large increases in the estimated runoff.

The two next sections will zoom in on the two major events to present the dynamics during these periods in more detail.

### 5.2.3 Phase 1

By decreasing the interval length for the running mean of the positions, velocity- and strain rate calculations, a more detailed analysis of the changes during the first major event can be conducted. For the time-scale of this event, a 1-hour interval for the velocity- and strain rate calculations and 3-hour running mean for the vertical positions was found to be the best trade-off between the estimated displacements and variation/noise in the data.

The period of increased surface velocities lasted approximately 30 hours, from the initial acceleration at HDF3 right after midnight on July 10<sup>th</sup>, to the velocity of HDF1 normalized to the values prior to the event around 06.00 on the morning of July 12<sup>th</sup>. The overall event had a wave-like progression initiating at HDF3 with increased horizontal velocities and slightly elevated positions, before being overlapped by a large acceleration and significant increases in the vertical positions at HDF2 and later on HDF1. The horizontal velocities of HDF3 experienced a fivefold increase up the maximum hourly displacement with a unit of  $\sim 1$  m/day. This is the largest horizontal surface velocity observed for HDF3 over the entire year, and is also the only observation of a period where HDF3 has the largest horizontal velocity of the three stations. During the following hour, the horizontal velocities abruptly decreased to a value close to  $\sim 0.35$  m/day before once again reaching a velocity of 1 m/day.



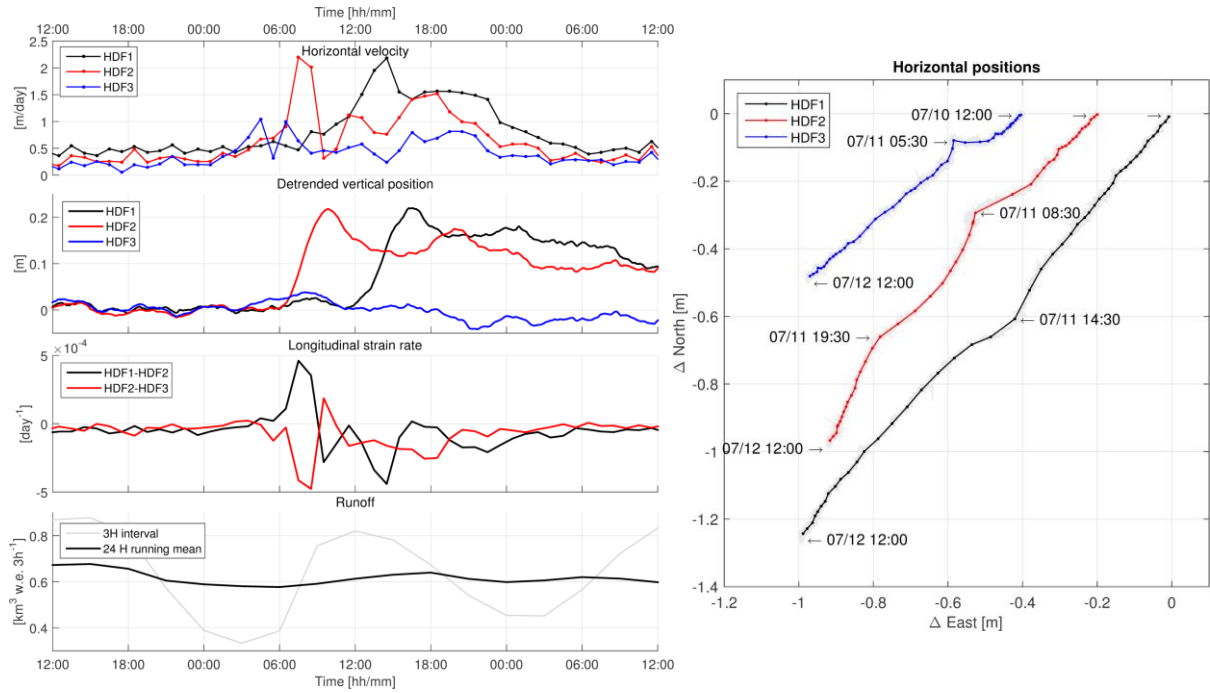


Figure 5.11. Plot of phase 1 in the period July 10-12<sup>th</sup>. Left: The combined plot shows horizontal velocity and strain rates for hourly intervals. The de-trended vertical positions are 3-hour moving averages. The estimated runoff is given for 3-hour intervals and a 24-hour running mean. Right: The horizontal positions for 1-hour intervals.

This pulse-like variation in the horizontal velocities can also be observed in the following acceleration at HDF2, where the velocity catches up with that of HDF3 before rapidly increasing to a level of 2.25 m/day, marking a ninefold increase compared to values at the beginning of the event. While the vertical positions of HDF3 only experienced slightly elevated values during the period of increased velocities, the situation was different at HDF2. The vertical positions of HDF2 started to rapidly increase when the surface velocities reached a value of  $\sim 1$  m/day and continued to increase to a maximum level of  $\sim 22$  cm above the initial trend. This maximum elevation was reached at the same time as the horizontal velocity suddenly dropped down to a temporary level of 0.35 m/day. From this temporary minimum in horizontal velocity, a second acceleration phase was initiated, while the vertical positions of the station slightly decreased. After reaching a horizontal velocity of  $\sim 1.1$  m/day, a slight deceleration can be observed before the third and last acceleration phase for HDF2 increased the horizontal velocities up to a level of 1.5 m/day. Similar to the first phase, the vertical positions reached a temporary maximum elevation after the peak horizontal velocities, before gradually decreasing but still maintaining the elevated positions.

The first acceleration phase for HDF1 was initiated around 5 hours later than HDF2 and HDF3, with more gradual increases in the horizontal velocity. The peak horizontal velocity can be observed 7 hours after the peak at HDF2. The vertical positions show a sudden increase in elevation as the horizontal velocities passes 1 m/day, peaks out and starts a gentle lowering right

when the horizontal motion has decelerated and the velocities reaches a temporary minimum just below 1.5 m/day. A slight increase followed by steady horizontal velocities of  $\sim 1.5$  m/day over a 5-hour period can be observed, before the horizontal velocities of HDF1 and the two other stations starts settling towards the condition prior to the event.

The difference in timing of the horizontal acceleration at each station have large impacts on the calculated longitudinal strain rates, and leads to significant contraction between HDF1-HDF2 and extension between HDF2-HDF3 when HDF2 experiences the rapid increase in horizontal velocity. When the velocity at HDF2 later drops below the level of both HDF1 and HDF3, the situation is the opposite, with extension between HDF1-HDF2 and contraction between HDF2-HDF3. As the horizontal velocity of HDF1 continues to increase from the second phase peak velocity of HDF2, the largely negative longitudinal strain rates show significant extension between these two stations.

The horizontal motion during phase one shows temporary lateral shifts from the long-term path during at all three stations during phase 1. The timing of the lateral shifts coincided with the observed initial rapid horizontal acceleration and elevated vertical position at the respective stations. The largest lateral variation in the horizontal positions can be observed for HDF2, with two major shifts in the northwest direction coinciding with the two observed velocity peaks, and is the station with the most evident non-linear path for this period. The initial temporary shift in the northwest direction at HDF3 transitions to a path that slightly deviates from the initial path prior to the shift. HDF1 has the most linear path overall, and experienced a shift in the southeast direction, opposite to the two other stations. Although the observed shifts are small in magnitude, they can be important for the glaciological interpretation of the short-term changes in the motion.

For the time-scale of phase 1, the estimated runoff values follow the diurnal variation, mainly controlled by the diurnal variation in temperature. The largest increase in the estimated runoff occurred in the days prior to phase 1, with a peak value at the onset of phase 1, and shows a slightly negative trend throughout the period. The rapid increase in motion of HDF2 and HDF3 occur early in the morning when the estimated runoff values are at the lowest level of the day.

#### **5.2.4 Phase 2**

During the second phase, the increases in horizontal velocities are initiated almost simultaneously at all three stations, and the acceleration and deceleration phase over the four consecutive days are similar but different in size (Figure 5.12). The vertical positions of HDF1

starts to elevate right before the initiated increase in horizontal velocities, and peaks at a level of  $\sim 20$  cm above the initial trend before lowering at the same approximate rate as the elevating rate. HDF2 starts to elevate later and with a magnitude half of what is observed at HDF1. HDF3 shows slight increases in elevation, but these are small compared to those of HDF2 and especially HDF1.

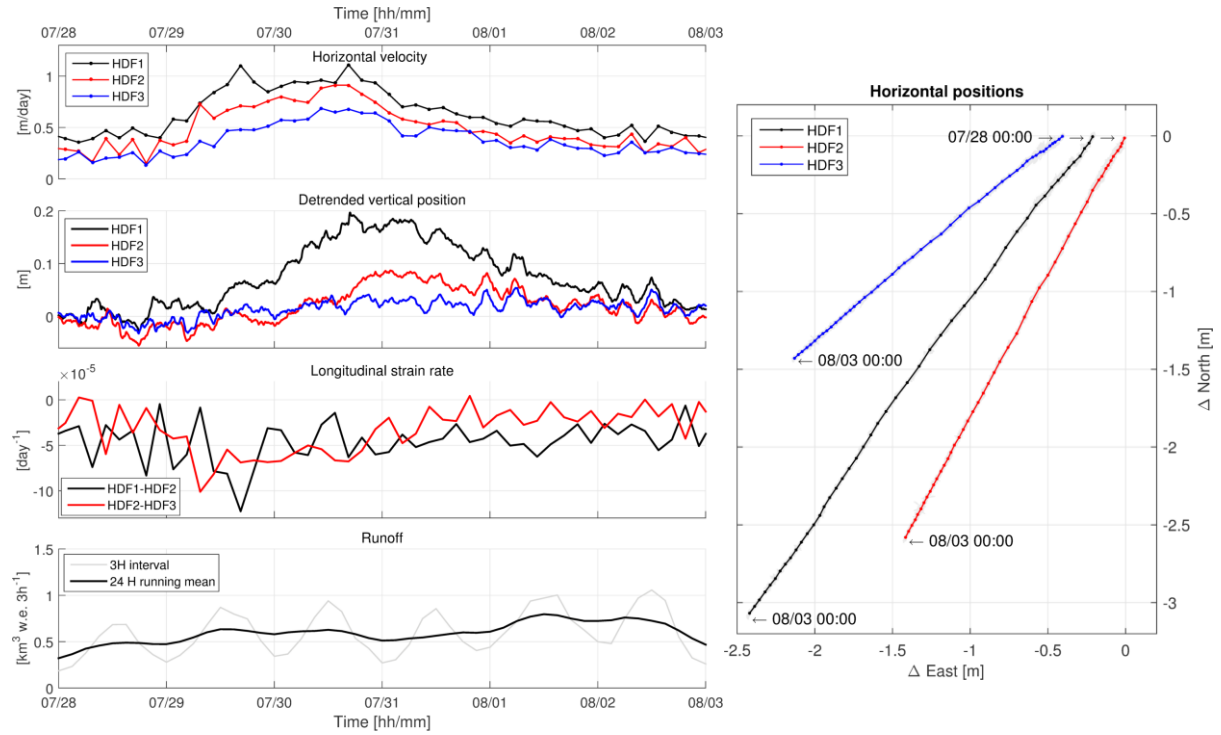


Figure 5.12. Plot of phase 2 in the period July 28<sup>th</sup>-August 3<sup>rd</sup>. Left: The combined plot shows horizontal velocity and strain rates for 3-hour intervals. The de-trended vertical positions are 3-hour moving averages. The estimated runoff is given for 3-hour intervals and a 24-hour running mean. Right: The horizontal positions for 3-hour intervals.

The longitudinal strain rates are overall smaller in magnitude compared to the first event, due to the more simultaneous acceleration and deceleration at all three stations. The largest negative longitudinal strain rates between HDF1-HDF2 can be observed during at the largest peak velocity for HDF1, indicating extension between these two stations. The horizontal motion for all three stations are different from phase 1, but the difference in interval length must be taken into account when comparing directly. All three stations follow an almost linear path in slightly different directions, and do not have any significant lateral shifts for the 3-hour interval length.

The estimated runoff values prior to phase 2 reached a temporary low level before increasing towards the onset and throughout phase 2. The maximum level of estimated runoff was reached towards the end of the period, and this is not reflected in the observed evolution of the horizontal surface velocities and vertical positions throughout the period.

### 5.2.5 Supraglacial meltwater and lake drainage

From the manual inspection of the Landsat 8 satellite images, clear changes in the glacier surface hydrology could be observed over the summer season. The first cloud-free scene with signs of supraglacial meltwater was captured on June 21<sup>st</sup>, and was limited to a few small lakes, including one at the southwest foot of Exilfjellet. On July 5<sup>th</sup>, the number of supraglacial lakes had increased and a few rivers were visible. The increasing presence of meltwater could be observed until the end of the July, when large parts of the lower and middle part of the glacier was snow-free and lakes and water channels were less visible on the satellite images.

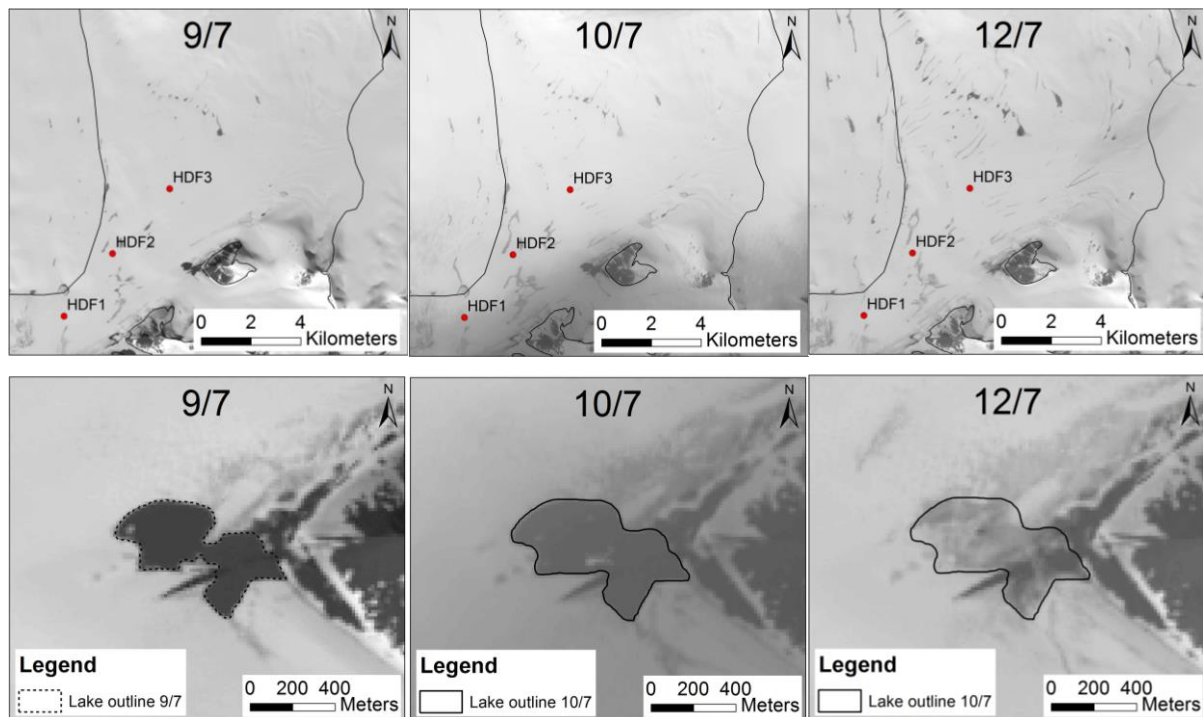


Figure 5.13. Landsat 8 scenes (NASA/USGS, 2015) from July 9<sup>th</sup>, 10<sup>th</sup> and 12<sup>th</sup>. Upper row: Overview of the central and lower part of Holtedahlfonna. The number of supraglacial lakes and rivers increases over the 3-day period. Lower row: The most prominent supraglacial lake, and its development over the three days. The lake reached an extent of 0.24 km<sup>2</sup> on July 10<sup>th</sup> before it drained sometime before the image was captured on July 12<sup>th</sup>.

Although there were several lakes that grew in size and later drained, the one at the foot of Exilfjellet stood out in terms of growth rate and later drainage. Since it was first visible on June 21<sup>st</sup>, it continued to grow between July 5-9<sup>th</sup> and to its observed maximum extent on July 10<sup>th</sup>. The area of the lake increased from 0.19 km<sup>2</sup> on the July 9<sup>th</sup> to 0.24 km<sup>2</sup> on July 10<sup>th</sup>, before the lake had disappeared on the scene from July 12<sup>th</sup> (Figure 5.13). This implies that the lake drained sometime between the July 10<sup>th</sup> 12:52 and July 12<sup>th</sup> 12:40 (Central European Time), when the respective satellite images were captured.

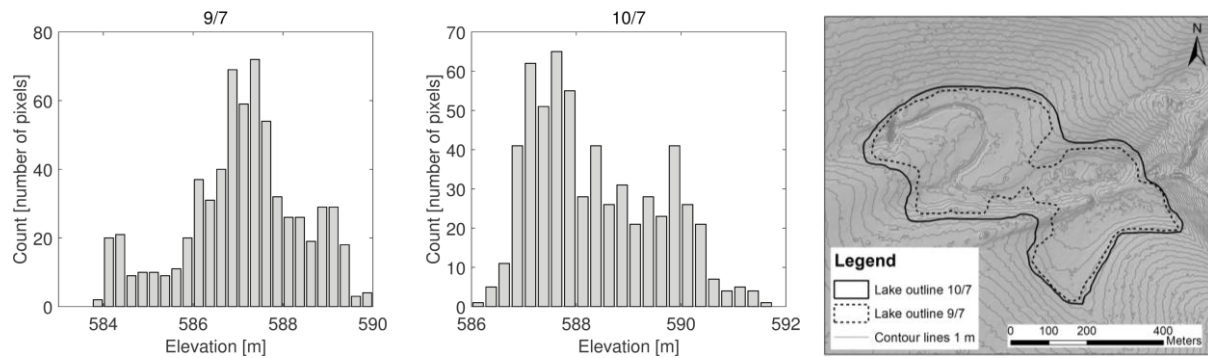


Figure 5.14. Histograms (left and middle) of elevation values along the lake outlines (right) at the two given dates, divided into 0.25 m bins. The middle plot, representing the elevation values for the outline on July 10<sup>th</sup>, shows a skewed distribution, while the values for July 9<sup>th</sup> (left) are more or less normally distributed. The shaded relief and contour lines are derived from a DEM (NPI, 2014).

The extracted elevation values along the digitized lake outlines from July 9<sup>th</sup> and 10<sup>th</sup> have different distributions on, as illustrated in Figure 5.14. On July 9<sup>th</sup>, the elevation values are more or less normally distributed, while a skewed distribution can be observed for the values from July 10<sup>th</sup>. The volume estimates of the lake on July 9<sup>th</sup> and 10<sup>th</sup> are given in Table 5.3, and include the range of volumes for  $\pm 1$  standard deviation and the mode of elevation values along the lake outlines. By using the mode of elevation values for both days, the volume of the lake increased with  $\sim 50\,000\text{ m}^3$  between July 9-10<sup>th</sup>, and had an observed maximum volume of  $390\,000\text{ m}^3$  before the drainage event. The latter volume compares to an estimated peak runoff of  $\sim 0.85\text{ km}^3$  w.e.  $3\text{h}^{-1}$  for the entire area above HDF1 at the onset of phase 1.

Table 5.3. Estimates of the volume of the supraglacial lake on July 9<sup>th</sup> and 10<sup>th</sup>. The different volume estimates relate to the different elevation values from the DEM along the lake outlines.

Date	Mean elevation	Volume [ $10^{-4}\text{ km}^3$ ]		
		+1 STD	-1 STD	Mode
July 9 <sup>th</sup>	2.9	5.9	1.0	3.4
July 10 <sup>th</sup>	5.6	8.8	3.1	3.9

The lake was located at a 3 km distance from HDF2 and HDF3, and 5.3 km from HDF1. By inspecting the bed topography, a ridge is present on the east-southeast side of the lake footprint on the glacier bed (Figure 5.15). A subglacial valley can be observed southeast of the flow line between HDF2 and HDF3, and local deepenings are present both above and below HDF2 (Figure 5.15).

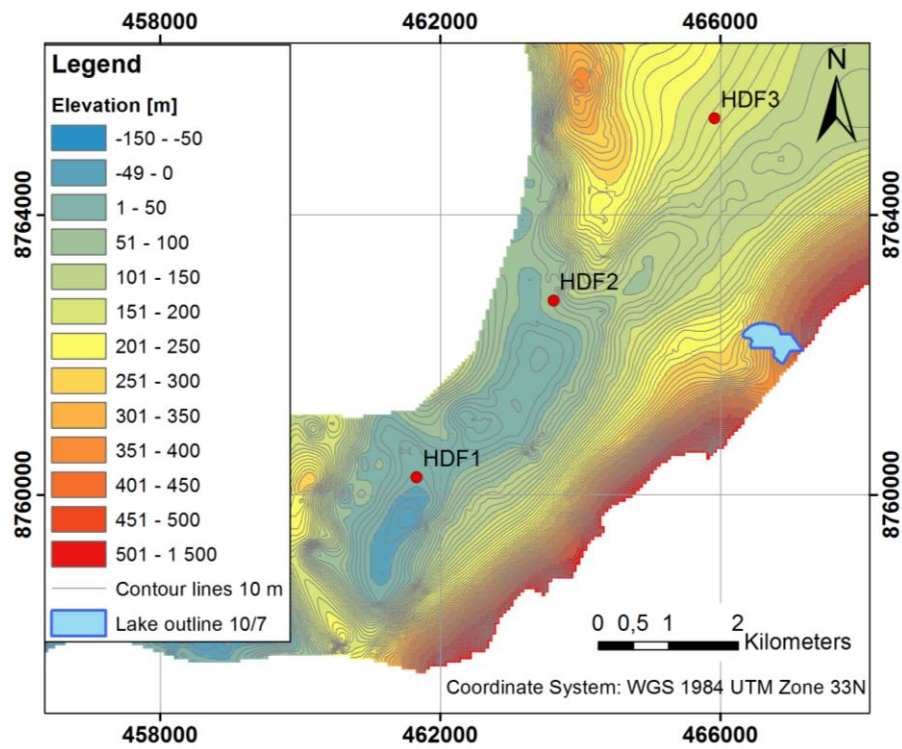


Figure 5.15. Bed topography of Holtedahlfonna (J. Kohler, unpublished data). The given locations for the GPS-stations are referring to their position at August 1<sup>st</sup> 2015.

## 6 Discussion

### 6.1 GNSS setup and post-processing results

The setup of the GNSS stations proved to work well, but with some observed problems both during winter and summer. Malfunction of the components can occur, and even though each station has been tested thoroughly before deploying the equipment into the field, one cannot be certain that each component performs as planned. For the HDF3 station during winter, the three-month data gap can probably be related to depletion of the batteries. This means that there is room for improvement regarding the dimensioning- and type of batteries, as well as minimization of power consumption and the length of the programmed observation interval during winter. However, since the HDF1 worked as expected during winter and had a similar setup, the malfunction on HDF3 can probably be assigned to the batteries. Another possible explanation is that the solar panel was covered with snow in the period before the shut-down, and since the GNSS receiver is programmed to shut-off if the voltage of the batteries is below a certain limit, the voltage could have been reduced before entering the dark season. The data gap on HDF1 during summer can have been related either to the batteries or the solar panel, and a potential explanation for the latter is that it was snow-covered over a period.

The GNSS antenna is mounted on top of a 6 m long mass balance stake, with approximately 4 m exposed length above the ice. This means that the antenna not only measures the motion of the bottom end of the stake, but also how the upper end is affected by changes in the wind speed and direction. Since the solar panel is mounted on the same stake, it has a larger direction-dependent area on which the forces of the wind can act as a variable load. This potential variability will mostly affect the horizontal position, but also has an increasing vertical component as the magnitude of the displacements in the horizontal plane increases. This type of setup certainly has room for improvement, and one could consider mounting the solar panel on a separate stake to reduce the potential wind-affected area of the stake with the GNSS antenna. Another option is to install a more stable platform for the antenna, e.g. by using a tripod mount, as seen in Anderson et al. (2004). However, the possible variation in the estimated positions due to wind gets reduced when averaging over longer intervals. Since the AWS at HDF2 also measures the wind speed and direction, future work would include an analysis of the relationship between wind speed, wind direction and the variation in the estimated positions.

Multipath is one of the error sources that is not reduced or cancelled through the relative positioning and PPP, and can have significant contributions to the uncertainties of the estimated positions. At HAGN, a choke ring antenna was mounted, which is designed to reduce the

amount of incoming reflected signals more effectively than normal GNSS antennas (Hofmann-Wellenhof et al., 2008). For the stations on the glacier, there are no nearby artificial objects that can reflect the signals, except the AWS at HDF2. What is changing on the glacier, however, is the surface below the antenna, with snow cover of different heights, glacier ice and different hydrologic properties on the respective surfaces. Larson et al. (2009) found that the multipath reflections, given by the signal-to-noise ratio (SNR) from GPS observations, varies with the changing snow surface on the ground surrounding the antenna, and used this inversely to estimate snow depths. Another study (Larson et al., 2008) used a similar approach to measure the fluctuations in the surrounding soil moisture. As Hofmann-Wellenhof et al. (2008) points out, signals received from satellites at low elevations, which is the case for the area in this study (Figure 3.3), are more likely to multipath than from higher elevations. Thus, since the elevation cut-off was set to an angle of  $10^\circ$  in this study, the effect of multipath from these lowermost satellites was avoided. Though the effect of multipath to the variation in the estimated positions has not been quantified in this study, its presence is acknowledged and that it probably varies throughout the season with the changing surface properties. To further decrease the uncertainties in the position estimates for these glacier-related applications, analyses and modelling of multipath could be included in future work.

When it comes to the length of baselines, the results from the test period show that the mean running standard deviation is larger for the single baseline between NYA1-HDF1 than for HAGN-HDF1. While some of this difference can be related to the elevation difference between HAGN and NYA1, the length of the baseline is probably an important factor for the observed differences. Therefore, it would be preferable to reduce this baseline even further by installing base stations closer to the stations on the glacier. This especially has an effect if the baselines are reduced to a level where the L1+L2 technique can be used, rather than the LC, which proved to be a very precise technique for the NYAL-NYA1 baseline (Figure 5.3). However, due to the size of the glacier, the minimum distances between the stations and the glacier margin are  $\sim 2.2$  km, and it is not given that the L1+L2 technique would produce better results than LC at these distances. When processing the baseline HAGN-HDF1 with the same L1+L2 technique (not included in the results), the estimated positions had a large variation and outliers. This is most likely related to the increasing influence of ionosphere as the baseline increases, and illustrates the need for LC.

From a network perspective, the results from the test period show that the variation in the results was reduced by processing all the receivers in a network. By further increasing the number of base stations with a favorable geometric distribution located as close to the stations



on the glacier as possible, one can assume that a slightly higher precision can be achieved. For the example of Høltedahlfonna, a more extensive network of surrounding base stations would be logistically difficult and resource-demanding, and efforts are probably better spent at improving the methods in the post-processing stage.

A quantitative evaluation of the results from the test period is challenging, since the true motion of the glacier remains unknown. When calculating a running average over a given interval, and the running standard deviation over the same interval, this results in a measure of the variation of each coordinate averaged over the given interval length. Since the kinematic positions are correlated over time and that the running averages and standard deviations overlap for each consecutive position in the time-series, this must be considered when evaluating the results. The length of the interval will affect the resulting values, since the variation can be interval-length dependent, as seen for the slightly undulating pattern in the PPP solution. Also, the motion during the test period, especially visible for the elevated values starting on July 11<sup>th</sup>, affect the values for the calculated running standard deviations. However, by assuming that these observed displacements affect the calculated running standard deviations in a similar way for all the methods, the mean values for each method would reflect the overall variation in the different results. It is important to acknowledge the limitations of this quantitative comparison of the results, and that it must be combined with a qualitative assessment.

For the PPP solutions processed in kinematic mode, improved precision of the estimated positions was achieved when using both GPS and GLONASS satellites, compared to only using either of the systems. The increased number of available satellites and the improved geometry of the combined satellite constellation, illustrated by the lower GDOP values (Figure 3.4), therefore had an improving effect for this method. Although the variation in the estimated vertical positions for HDF1 was found to be the lowest for the kinematic PPP solution for the chosen 3-hour interval, it shows an undulating pattern in the vertical solution with a frequency that is larger than the 3-hour interval. Since the vertical positions are important for the interpretation of the glacier motion, the PPP solution would then suggest a vertical motion that is not present in the other solutions from relative positioning. Some lateral deviations from the long-term horizontal path are also visible. This would lead to incorrect horizontal velocities with magnitudes depending on the interval-length of the running average over which they are calculated. Thus, the results indicate that relative positioning using TRACK is the best method for estimating the true motion of the glacier, which is one of the aims of this study. However, the precision achieved with PPP makes it an interesting method to pursue in further work. The logistical advantage of not having to use base stations is large, and with further investigations on

how the periodic variation in the PPP solution can be reduced, the potential of this method for analyzing short-term changes of glacier dynamics can be increased even further.

The results from the pseudo-static positioning in Figure 5.1 show that there are significant variation between the estimated positions from the different methods, both between PPP and relative positioning, and also between the software packages GAMIT and RTKLIB using relative positioning. Since both the PPP and the RTKLIB solutions are based on the combination of GPS and GLONASS satellites, the observed variation in the estimated positions reflect the difference between the positioning methods. When decreasing the observation interval down to 1- and 0.5 hours, the solution from RTKLIB clearly has less variation in the horizontal direction. In the vertical direction, however, the variation is of the same magnitude as for the PPP solution of the same interval. This relation is unexpected and difficult to explain directly. The GAMIT solutions have the largest increases in variation in the vertical and horizontal positions when decreasing the observations length. This indicates clear limitations with this technique when processing over short intervals and using GPS satellites only. Thus, if the pseudo-static technique is to be applied for the purpose of estimating short-term glacier motion, these results indicate the importance of combining the two satellite systems.

The observed variation or error in the original GNSS time-series can be defined as white noise, which is time-independent, and time-correlated colored noise (Mao et al., 1999). Several studies have analyzed the noise components of GNSS estimated positions and how these can be filtered (e.g. Mao et al., 1999; Williams et al., 2004; Montillet et al., 2013). It is beyond the scope of this thesis to do an analysis of the noise components in the estimated positions. However, it is useful to consider the different noise components, and how filtering techniques could be applied to further improve the time-series of positions in future work. A first step could be to estimate and filter the white noise, as seen in Montillet et al. (2013).

## **6.2 Glaciological interpretation**

This study highlights some of the major events, and interprets these in relation to the observed and/or modelled changes in the surface hydrology and meteorology. It is important to acknowledge the complexity of the combined data from all stations on the glacier, which makes it demanding to interpret and understand all processes occurring during the entire observed period and particularly during summer. From a glaciological perspective, there are probably more events and processes related to glacier dynamics that have not been covered or commented here.

The high temporal resolution and continuous data during the summer months enables the analyses of both long-term changes with longer averaging-intervals (e.g. 24 hours) and also changes on an hourly basis. When defining the appropriate averaging intervals, they depend on the variation and noise in the estimated positions. Since the vertical component of the positions has the largest uncertainty, it is the limiting factor when deciding the length of these intervals.

Due to outliers and inter-daily variation between the estimated positions during winter, it is difficult to identify possible short-term changes in the velocities and vertical positions with certainty. A possible explanation for the observed variation in the horizontal and vertical positions at HDF1 and HDF3 during September 2014 is a temporary snow cover on the antennas, due to the observed increases in precipitation in that period. While HDF1 had a rather steady background velocity during winter, HDF3 shows slightly higher horizontal surface velocities during fall 2014 than in March/April 2015. Without the data gap at HDF3, it would be possible to observe the continuous development of the horizontal surface throughout the winter season, as for HDF1. A possible explanation for the higher horizontal velocity during fall 2014 could be that the glacier dynamically adjusted back to an equilibrium state after periods of increased motion downglacier during the summer season of 2014. A recent study (Christianson et al., 2015) observed water storage in a perennial firn aquifer on the upper parts of Høltedahlfonna, and they suggested that the aquifer is able to provide input to the englacial hydrology system. The observed motion during winter can thus be induced both by basal melt and the input from this firn aquifer on the upper parts of the glacier.

The vertical positions of HDF1 and HDF3 at the end of the summer season are in line with the linear trend from the initial period prior to the first major event (Figure 5.9). HDF2, however, has vertical positions at the end of summer that are lower than the initial trend. This could be due to changes in the surface topography, since the bed topography changes significantly in the surrounding area below HDF2. By including the results from the kinematic field survey, the surface topography around HDF2 can be examined in future work. Another explanation is that the assumption of steady motion in the background period was incorrect, and that the linear trend was based on a period where HDF2 experienced a gradual uplift. Also, since the observed vertical positions at HDF2 sustained over a two-week period after the first major event, the indicated local water storage at the bed can have led to increasing rates of basal melting.

When calculating the strain rates, it is assumed that the direct distance between the stations represent the distance along the flow line. However, with increasing distances, the distance along the flow line can deviate from the direct distance, and this is possibly the case when calculating

the longitudinal strain between HDF1 and HDF3. When evaluating the horizontal motion of each station, slightly different directions of the paths can be observed (Figure 5.12). Thus, when calculating the changes in elevation between HDF1 and HDF3 due to longitudinal strain, these estimates are biased by deviations in distance from the flow line. This bias can be reduced by decreasing the distances between the stations, but also by estimating the true distances along the flow line. The latter can be done by deploying more GNSS stations along the flow line to more accurately determine the direction of flow. Alternatively, optical or radar satellite imagery can be used to analyze the surface velocity fields, as seen in Kääb et al. (2005) and Lefauconnier et al. (2001), but the resolution of these flow fields might be too coarse for a direct comparison to the GNSS data. A simple sensitivity analysis that considers the magnitude of the change in the strain rates when using a simple geometric estimate of the distance along the flow line could also be applied in future work.

Since the calculations only are based on the longitudinal strain, the presence of and changes in lateral strain can possibly be a contributor to the changes in elevation. While some studies make the assumption of negligible lateral strain (e.g. Anderson et al., 2004), other studies have either measured the lateral strain (e.g. Hoffman et al., 2011; Andrews et al., 2014) or approximated the lateral strain from the glacier geometry (e.g. Howat et al., 2008). The latter option is difficult for the example of Holtedahlfonna due to the gradual transition to the bordering glacier Kongsvegen on the west side (Figure 2.1). Thus, for future work, it would be beneficial to install additional GNSS stations in the lateral direction of the flow line.

The assumption of constant vertical strain is also a factor that can bias the results, since the vertical strain has been observed to vary with depth (Sugiyama and Gudmundsson, 2003). As discussed by Howat et al. (2008), observed decreases in vertical strain with depth lead to an overestimation of the mean vertical strain. This means that the changes in elevation due to vertical strain also gets overestimated, and this can be a part of the explanation why the calculated changes in elevation at HDF2 due to vertical strain are possibly too large in magnitude.

For the bed separation, the uncertainties regarding the determination of the bed slope below HDF2 and the calculated changes in elevation due to vertical strain causes a significant uncertainty in the calculated bed separation, and it must therefore be considered as indicative. Due to the significant changes in the bed topography in the area below HDF2, it is not obvious at which length scales the bed slope is to be calculated. By using the approach from Hoffman et al. (2011), the bed slope was calculated from the adjusted values for changes in elevation due to

vertical strain in the background period. The relative magnitude of the change in elevation due to vertical strain thus causes a bias in the calculated bed separation throughout the summer, and can possibly explain why the bed separation ends up with positive values at the end of the summer.

The calculated changes in elevation for HDF2 due to vertical strain, derived from the longitudinal strain rates between HDF1 and HDF3, do not capture the local changes in strain in between HDF1 and HDF3. This is illustrated in Figure 5.11, where the initial rapid increase in horizontal surface velocities at HDF2 causes a significant compression between HDF1 and HDF2 and extension between HDF2 and HDF3. The rapid acceleration in horizontal surface velocities at HDF2 thus leads to increased elevations between HDF2 and HDF1 due to vertical strain, which cannot be observed when only evaluating the longitudinal strain between HDF1 and HDF3 over the same time-interval. This illustrates the advantage of having three or more GNSS stations along the same flow line. The sustained elevated positions of HDF2 in the two-week period following the rapid speed-up event on July 11<sup>th</sup> can be interpreted as local water storage at the glacier bed. This observation further supports the use of several GNSS stations, since this assumed local water storage could not have been captured from the observations of HDF1 and HDF3. Thus, the results from this study were significantly enriched by installing the additional GNSS receiver at HDF2. For future work, this emphasizes the benefits of installing even more GNSS stations on the glacier, both in the longitudinal and lateral direction, as discussed above.

By increasing the number of GNSS stations on the glacier and further investigating the strain components, it would be possible to get more precise and spatially distributed estimates of the bed separation. Since the bed separation is caused by the hydraulic jacking from the increasing input of meltwater, it could also be possible to use these spatially distributed estimates of bed separation to estimate the water discharge below the glacier by examining the GNSS data only.

Since the surface mass balance model estimated a more negative mass balance than what was observed in the mass balance measurements by NPI (J. Kohler and W. Van Pelt, personal communication, 2015), the absolute values of the estimated runoff from the surface mass balance model could be exaggerated. However, by looking at the relative changes in the estimated runoff, the potential biases in the absolute values are less important. It is also important to have in mind what the estimated runoff values in the results represent. Since they are summed over the entire area above HDF1, they illustrate the amount of water that can drain

supraglacially or englacially down to the glacier bed. No flow routing is considered in the estimated runoff values, and this could certainly be the focus in future work.

The observed and modelled changes in the surface hydrology correlate well with the observed changes in glacier motion. Prior to both major events, the estimated runoff increased significantly. In the period between the two events, the sudden drop in estimated runoff coincides with low horizontal surface velocities and steady vertical motion. The observed formation of supraglacial lakes and melt channels in the Landsat 8 images show how periods of high meltwater production lead to temporary storage of water at the glacier surface (Figure 5.13). Although the observed supraglacial lake in the Landsat images was the largest of in the inspected period, there were several smaller lakes that were visible. To increase our understanding of the influence of lake drainage on glacier motion, a next step of this study would be to include a more extensive mapping of the supraglacial lakes, both in terms of area, volume and timing of drainage. Hoffman et al. (2011) used Landsat images to count the number of lakes filling and draining within a proximity of 5 km from each GPS station, and compared these observations to the GPS-derived glacier motion at each station. Georgiou et al. (2009) used the optical ASTER satellite images to estimate supraglacial lake volume from the optical reflectance of the lake. It is also possible to use radar satellite imagery to identify supraglacial lakes (Johansson and Brown, 2011).

Since the high resolution DEM over Holtedahlfonna from 2009 is available and the high temporal resolution of Landsat 8 scenes over the area enables frequent observations of the surface features, the combination of these can be further enhanced in future work. A first step could be to adjust the DEM to the horizontal motion and vertical changes of the glacier since 2009, so that the observed outlines of supraglacial lakes have closer relations to the elevation contours on the DEM. The supraglacial lake in this study was located at the intersection between Diadembreen and Holtedahlfonna, and the shape of the glacier surface is likely to have been distorted in the 6-year period. This makes the fitting of the lake outline to the elevation contours more difficult. With an adjusted DEM, and by using a similar approach as Hoffman et al. (2011), but with volume estimates, the influence of widespread supraglacial lake drainage can be examined further.

The timing and location of observed lake drainage indicates a relation to the observed rapid changes in glacier motion. However, it cannot be concluded whether the observed lake drainage caused the rapid horizontal acceleration and uplift, or if the observed motion was induced by other inputs of melt water and caused the observed lake drainage. It is also possible that the two

events occurred independently. If assuming that the lake drainage was the triggering factor, the induced motion probably caused other smaller lakes and englacially stored water to drain to the glacier bed and further enhance the motion. HDF2 experienced a ninefold increase in the horizontal surface velocities, lateral translation and an uplift of approximately 20 cm during the first event. The drainage of a ~2 km diameter supraglacial lake on the Greenland Ice Sheet was observed by Das et al. (2008), and coincided with surface velocities of ~10 times the background velocity and 1.2 m uplift and 0.8 m lateral translation of a GPS station located 0.5 km from the lake margin. The size of the lake and the magnitude of observed motion were larger than what was observed in this study, but the relative patterns are comparable. Hoffman et al. (2011) observed increases of 4-5 times the background velocity during the largest lake drainage events, but no lateral translation. In their study, they emphasize how the condition of the basal drainage system controls how the glacier motion is affected by lake drainage events, and also how an increasing distance from the observing GNSS stations and the supraglacial lakes lead to muted responses in the observed glacier motion.

The observed increases in temperature and precipitation over the last decades are significant (Table 2.1), and climate projections for the 21<sup>st</sup> century indicate future warming of the Svalbard region three times stronger than the trend from the last decade (Førland et al., 2012). By the end of the century, it is projected an increase of 10 °C in the average winter air temperature in Longyearbyen (Førland et al., 2012). Due to the large observed fluctuations in the air temperature during winter (Figure 2.3), the projected warming indicates that temperatures above 0 °C can occur more often during winter on Holtedahlfonna. These changes will influence the surface hydrology during winter and can possibly affect the glacier motion if meltwater or rain is transported to the glacier bed. The summer temperatures are also projected to further increase, and this indicates that the observed meltwater-induced glacier motion in this study is likely to increase throughout the century. However, the relation between long-term increases in the meltwater production, a developing hydrologic drainage system and induced bed sliding needs to be investigated further.

## 7 Conclusions

In this study, kinematic relative positioning in a network using two base stations and the three receivers on the glacier was found to be the method with best combination of precision and ability to capture the true motion and short-term changes of the glacier. The stationary GNSS stations were used to approximate conservative uncertainties for each estimated position on the glacier of  $\pm 18$  mm and  $\pm 69$  mm (95% confidence level) in the horizontal and vertical directions, respectively.

During the winter months, the lowermost GNSS station HDF1 had a steady horizontal surface velocity of  $\sim 0.28$  m/day, while the uppermost station HDF3 had mean winter velocity of  $\sim 0.15$  m/day but with slightly larger velocities during fall 2014 than in late spring 2015. From the sensitivity analysis, the deformation velocity at HDF2 was found to be less than 10 mm/day. A rapid transition from steady horizontal and vertical motion to significant acceleration in horizontal surface velocities and vertical uplift was observed at all three stations during the first event in mid-July. Horizontal translations from the long-term trajectories coincided with the rapid changes in surface velocities and vertical uplift. The observed wave-like motion and horizontal translation during the first major event indicates hydraulic jacking caused by a pulse of water at the glacier bed. Both the lower-most and middle station (HDF1 and HDF2 respectively) sustained elevated positions over the following two-week period, with the largest magnitude at HDF2, and temporary storage of sub-glacial water is a possible explanation for this observation. The second major event had a more gradual progression, with increasing surface velocities and elevated vertical positions.

During the two major events, significant variations in the longitudinal strain was observed, with both compression and extension between the three stations. The estimated lowering of the surface due to vertical strain for HDF2 was significantly larger than the observed downward motion of the GNSS station, and indicates an overestimation of the magnitude of the vertical strain. A bed separation of up to  $\sim 20$  cm was estimated by adjusting the changes due to vertical strain, but the absolute magnitude of the bed separation must be considered as indicative due to the uncertainties in the bed slope and the vertical strain.

The estimated increases in meltwater production from the surface mass balance model prior to and during the major events indicates that the changes in the surface hydrology had large influences on the glacier motion. The evolution of the motion during the two events indicates a difference in the condition of the basal and englacial hydrologic drainage system at the onset of each event. Prior to the first event, the increasing rates of surface meltwater did not affect the



glacier motion significantly before the rapid transition. The location and timing of a supraglacial lake drainage in the period of the first major event indicates that it may have contributed to hydraulic jacking and enhanced basal motion, although the estimated volume of the lake was small compared to the total estimated runoff above HDF1. The gradual increases in surface velocities and vertical positions during the second event indicates that the englacial and basal hydrologic drainage system had developed since the first event.

The results from this study show the potential of high resolution GNSS measurements for analyzing glacier dynamics and the influence of melt-water. The complexity of glacier mechanics leads to uncertainties in the estimated strain-related deformations of the ice, and additional field-measurements and modelling would certainly contribute to a better understanding of glacier strain and improve the assumptions made in this study. Although this study has several limitations, it demonstrates some of the dynamic processes that occur on Høltedalsfonna over the course of a year, and has provided knowledge that can be further developed and applied on other glaciers.

## 8 References

- Anderson, R. S., Anderson, S. P., MacGregor, K. R., Waddington, E. D., O'Neel, S., Riihimäki, C. A., Loso, M. G., 2004. Strong feedbacks between hydrology and sliding of a small alpine glacier. *Journal of Geophysical Research: Earth Surface*, Vol. 109, No. F3, F03005. doi: 10.1029/2004JF000120.
- Andrews, L. C., Catania, G. A., Hoffman, M. J., Gulley, J. D., Luthi, M. P., Ryser, C., Hawley, R. L., Neumann, T. A., 2014. Direct observations of evolving subglacial drainage beneath the Greenland Ice Sheet. *Nature*, Vol. 514, No. 7520, 80-83. doi: 10.1038/nature13796.
- Awange, J. L., 2012. *Environmental Monitoring using GNSS: Global Navigation Satellite Systems*. Springer-Verlag Berlin Heidelberg. 382 pp.
- Bartholomew, I., Nienow, P., Mair, D., Hubbard, A., King, M. A., Sole, A., 2010. Seasonal evolution of subglacial drainage and acceleration in a Greenland outlet glacier. *Nature Geosci*, Vol. 3, No. 6, 408-411.
- Battle, W., 1951. Glacier movement in north-east Greenland, 1949: with a note on some subglacial observations. *Journal of Glaciology*, Vol. 1, 559-563.
- Benn, D. I., Evans, D. J. A., 2010. *Glaciers & glaciation*. Hodder Education. 2. edition. 802 pp.
- Björnsson, H., Gjessing, Y., Hamran, S.-E., Hagen, J. O., Liestøl, O., Pálsson, F., Erlingsson, B., 1996. The thermal regime of sub-polar glaciers mapped by multi-frequency radio-echo sounding. *Journal of Glaciology*, Vol. 42, No. 140, 23-32.
- Bos, M., Scherneck, H., 2011. *Free ocean tide loading provider*. Onsala Space Observatory. <http://holt.oso.chalmers.se/loading/>
- Bowring, B. R., 1985. The accuracy of geodetic latitude and height equations. *Survey Review*, Vol. 28, No. 218, 202-206. doi: doi:10.1179/sre.1985.28.218.202.
- CGS, 2015. *Tools and applications (CSRS PPP)*. Natural Resources Canada / Canadian Geodetic Survey (CGS). Available at <http://www.nrcan.gc.ca/earth-sciences/geomatics/geodetic-reference-systems/tools-applications/10925#ppp> (Visited 28.11.2015).
- Christianson, K., Kohler, J., Alley, R. B., Nuth, C., van Pelt, W. J. J., 2015. Dynamic perennial firn aquifer on an Arctic glacier. *Geophysical Research Letters*, Vol. 42, No. 5, 1418-1426. doi: 10.1002/2014GL062806.
- CODE, 2015. *Satellite orbits and clocks (15 min;\*.sp3)* Center for Orbit Determination in Europe (CODE). <ftp://cddis.gsfc.nasa.gov/pub/gps/products/mgex/>
- Craymer, M., 2013. *Geodetic Toolbox, xyz2ell2(X,Y,Z,a,e2) Version 2.97*. Mike Craymer / Matlab Central. <http://www.mathworks.com/matlabcentral/fileexchange/15285-geodetic-toolbox/content/geodetic/xyz2ell2.m>
- Cuffey, K., Paterson, W., 2010. *The Physics of Glaciers*. Butterworth-Heinemann/Elsevier. 704 pp.
- Das, S. B., Joughin, I., Behn, M. D., Howat, I. M., King, M. A., Lizarralde, D., Bhatia, M. P., 2008. Fracture Propagation to the Base of the Greenland Ice Sheet During Supraglacial Lake Drainage. *Science*, Vol. 320, No. 5877, 778-781. doi: 10.1126/science.1153360.
- Devore, J. L., Berk, K. N., 2007. *Modern mathematical statistics with applications*. Thomson Brooks/Cole. 838 pp.
- eKlima, 2015. *Free access to weather- and climate data from Norwegian Meteorological Institute from historical data to real time observations*. eKlima / Norwegian Meteorological Institute. [www.eklima.no](http://www.eklima.no)
- ESRI, 2015. *ArcGIS Desktop: Release 10.3*. Redlands, CA: Environmental Systems Research Institute.
- Førland, E. J., Benestad, R., Hanssen-Bauer, I., Haugen, J. E., Skaugen, T. E., 2012. Temperature and precipitation development at Svalbard 1900–2100. *Advances in Meteorology*, Vol. 2011, 255-267.
- Fowler, A., 1987. Sliding with cavity formation. *J. Glaciol*, Vol. 33, No. 115, 255-267.
- Georgiou, S., Shepherd, A., McMillan, M., Nienow, P., 2009. Seasonal evolution of supraglacial lake volume from ASTER imagery. *Annals of Glaciology*, Vol. 50, No. 52, 95-100. doi: 10.3189/172756409789624328.

- Gudmundsson, G. H., Bauder, A., Lüthi, M., Fischer, U. H., Funk, M., 1999. Estimating rates of basal motion and internal ice deformation from continuous tilt measurements. *Annals of Glaciology*, Vol. 28, No. 1, 247-252. doi: 10.3189/172756499781821751.
- Gurtner, W., Estey, L., 2007. RINEX-The Receiver Independent Exchange Format-Version 3.00. *Astronomical Institute, University of Bern and UNAVCO, Boulder, Colorado.*
- Hagen, J. O., Kohler, J., Melvold, K., Winther, J.-G., 2003. Glaciers in Svalbard: mass balance, runoff and freshwater flux. *Polar Research*, Vol. 22, No. 2, 145-159. doi: 10.1111/j.1751-8369.2003.tb00104.x.
- Hanssen-Bauer, I., Solås, M. K., Steffensen, E., 1990. Climate of Spitsbergen. *DNMI KLIMA Report*, No. 39/90,
- Harper, J. T., Humphrey, N. F., Pfeffer, W. T., Lazar, B., 2007. Two modes of accelerated glacier sliding related to water. *Geophysical research letters*, Vol. 34, No. 12,
- Herring, T., King, R., McClusky, S., 2008. *Introduction to Gamit/Globk*. Massachusetts Institute of Technology, Cambridge. 36 pp.
- Herring, T., King, R., McClusky, S., 2015. GAMIT reference manual. *GPS Analysis at MIT, release 10.6*, 168 pp.
- Hinze, H., Seeber, G., 1988. Ice-motion determination by means of satellite positioning systems. *Annals of Glaciology*, Vol. 11, 36-41.
- Hoffman, M., Catania, G., Neumann, T., Andrews, L., Rumrill, J., 2011. Links between acceleration, melting, and supraglacial lake drainage of the western Greenland Ice Sheet. *Journal of Geophysical Research: Earth Surface* (2003–2012), Vol. 116, No. F4,
- Hofmann-Wellenhof, B., Lichtenegger, H., Wasle, E., 2008. *GNSS – Global Navigation Satellite Systems: GPS, GLONASS, Galileo, and more*. Springer-Verlag Wien. 516 pp.
- Hollenstein, C., Kahle, H. G., Geiger, A., Jenny, S., Goes, S., Giardini, D., 2003. New GPS constraints on the Africa-Eurasia plate boundary zone in southern Italy. *Geophysical Research Letters*, Vol. 30, No. 18, n/a-n/a. doi: 10.1029/2003GL017554.
- Hooke, R. L., Calla, P., Holmlund, P., Nilsson, M., Stroeven, A., 1989. A 3 year record of seasonal variations in surface velocity, Storglaciären, Sweden. *Journal of Glaciology*, Vol. 35, No. 120, 235-247.
- Howat, I. M., Tulaczyk, S., Waddington, E., Björnsson, H., 2008. Dynamic controls on glacier basal motion inferred from surface ice motion. *Journal of Geophysical Research: Earth Surface*, Vol. 113, No. F3, n/a-n/a. doi: 10.1029/2007JF000925.
- IGN, 2013. *ITRS and WGS84*. The International Terrestrial Reference Frame (ITRF)/Institut Géographique National (IGN). Available at <ftp://itrf.ensg.ign.fr/pub/itrf/WGS84.TXT> (Visited 03.12.2015).
- IGS, 2009. *IGS products*. IGS/NASA. Available at <https://igsb.jpl.nasa.gov/components/prods.html> (Visited 28.11.2015).
- Iken, A., Röthlisberger, H., Flotron, A., Haeberli, W., 1983. The uplift of Unteraargletscher at the beginning of the melt season—a consequence of water storage at the bed. *Journal of Glaciology*, Vol. 29, No. 101, 28-47.
- Jania, J., Mochnacki, D., Gadek, B., 1996. The thermal structure of Hansbreen, a tidewater glacier in southern Spitsbergen, Svalbard. *Polar Research*, Vol. 15, No. 1, 53-66. doi: 10.1111/j.1751-8369.1996.tb00458.x.
- Johansson, A. M., Brown, I. A., 2011. Observations of supra-glacial lakes in west Greenland using winter wide swath Synthetic Aperture Radar. *Remote Sensing Letters*, Vol. 3, No. 6, 531-539. doi: 10.1080/01431161.2011.637527.
- Kääb, A., Lefauconnier, B., Melvold, K., 2005. Flow field of Kronebreen, Svalbard, using repeated Landsat 7 and ASTER data. *Annals of Glaciology, Vol 42, 2005*, Vol. 42, 7-13. doi: 10.3189/172756405781812916.
- Kaplan, E., Hegarty, C., 2005. *Understanding GPS: Principles and Applications, Second Edition*. Artech House. 707 pp.

- King, M., 2004. Rigorous GPS data-processing strategies for glaciological applications. *Journal of Glaciology*, Vol. 50, No. 171, 601-607. doi: 10.3189/172756504781829747.
- Kohler, J., Neumann, T. A., Robbins, J. W., Tronstad, S., Melland, G., 2013. ICESat Elevations in Antarctica Along the 2007-09 Norway-USA Traverse: Validation With Ground-Based GPS. *Geoscience and Remote Sensing, IEEE Transactions on*, Vol. 51, No. 3, 1578-1587. doi: 10.1109/TGRS.2012.2207963.
- König, M., Nuth, C., Kohler, J., Moholdt, G., Pettersen, R., 2014. A digital glacier database for svalbard. *Global Land Ice Measurements from Space*, Springer Berlin Heidelberg. 229-239.
- Kreyszig, E., 2010. *Advanced Engineering Mathematics, 10th edition*. John Wiley & Sons. 1264 pp.
- Larson, K., Small, E., Gutmann, E., Bilich, A., Axelrad, P., Braun, J., 2008. Using GPS multipath to measure soil moisture fluctuations: initial results. *GPS Solutions*, Vol. 12, No. 3, 173-177. doi: 10.1007/s10291-007-0076-6.
- Larson, K. M., Gutmann, E. D., Zavorotny, V. U., Braun, J. J., Williams, M. W., Nievinski, F. G., 2009. Can we measure snow depth with GPS receivers? *Geophysical Research Letters*, Vol. 36, No. 17, n/a-n/a. doi: 10.1029/2009GL039430.
- Lefauconnier, B., Hagen, J. O., Rudant, J. P., 1994. Flow speed and calving rate of Kongsbreen glacier, Svalbard, using SPOT images. *Polar Research*, Vol. 13, No. 1, 59-65. doi: 10.1111/j.1751-8369.1994.tb00437.x.
- Lefauconnier, B., Massonnet, D., Anker, G., 2001. Determination of ice flow velocity in Svalbard from ERS-1 interferometric observations. *Memoirs of National Institute of Polar Research. Special issue*, Vol. 54, 279-290.
- Liestøl, O., 1988. The glaciers in the Kongsfjorden area, Spitsbergen. *Norsk Geografisk Tidsskrift-Norwegian Journal of Geography*, Vol. 42, No. 4, 231-238.
- Luckman, A., Benn, D. I., Cottier, F., Bevan, S., Nilsen, F., Inall, M., 2015. Calving rates at tidewater glaciers vary strongly with ocean temperature. *Nat Commun*, Vol. 6, doi: 10.1038/ncomms9566.
- Manolakis, D. E., 1996. Efficient solution and performance analysis of 3-D position estimation by trilateration. *Aerospace and Electronic Systems, IEEE Transactions on*, Vol. 32, No. 4, 1239-1248. doi: 10.1109/7.543845.
- Manson, R., Coleman, R., Morgan, P., King, M., 2000. Ice velocities of the Lambert Glacier from static GPS observations. *Earth, Planets and Space*, Vol. 52, No. 11, 1031-1036. doi: 10.1186/BF03352326.
- Mao, A., Harrison, C. G. A., Dixon, T. H., 1999. Noise in GPS coordinate time series. *Journal of Geophysical Research: Solid Earth*, Vol. 104, No. B2, 2797-2816. doi: 10.1029/1998JB900033.
- MathWorks, 2014. *Matlab 8.4.0 R2014b*. The MathWorks, Inc., Natick, Massachusetts, United States.
- Melvold, K., Hagen, J. O., 1998. Evolution of a surge-type glacier in its quiescent phase: Kongsvegen, Spitsbergen, 1964-95. *Journal of Glaciology*, Vol. 44, No. 147, 394-404.
- Mireault, Y., Tétreault, P., Lahaye, F., Héroux, P., Kouba, J., 2008. Online Precise Point Positioning. *GPS World, Sep*, 59-64.
- Montillet, J.-P., Tregoning, P., McClusky, S., Yu, K., 2013. Extracting white noise statistics in GPS coordinate time series. *Geoscience and Remote Sensing Letters, IEEE*, Vol. 10, No. 3, 563-567.
- NASA/USGS, 2015. *Landsat 8 (L8 OLI/TIRS)*. Path 215-222, row 2-4, doy 158-213. The National Aeronautics and Space Administration (NASA) and The United States Geological Survey (USGS). <http://earthexplorer.usgs.gov/>
- NPI, 2014. *Terrengmodell Svalbard (S0 Terrengmodell)*. Tromsø, Norway: Norwegian Polar Institute. <https://data.npolar.no/dataset/dce53a47-c726-4845-85c3-a65b46fe2fea>

- NPI, 2015. *NP\_Basiskart\_Svalbard\_WMTS\_25833*. Norwegian Polar Institute.  
[http://geodata.npolar.no/arcgis/rest/services/Basisdata/NP\\_Basiskart\\_Svalbard\\_WMTS\\_25833/MapServer?f=jsapi](http://geodata.npolar.no/arcgis/rest/services/Basisdata/NP_Basiskart_Svalbard_WMTS_25833/MapServer?f=jsapi)
- Nuth, C., Schuler, T. V., Kohler, J., Altena, B., Hagen, J. O., 2012. Estimating the long-term calving flux of Kronebreen, Svalbard, from geodetic elevation changes and mass-balance modelling. *Journal of Glaciology*, Vol. 58, No. 207, 119-133. doi: 10.3189/2012JoG11J036.
- Rolstad, C., Norland, R., 2009. Ground-based interferometric radar for velocity and calving-rate measurements of the tidewater glacier at Kronebreen, Svalbard. *Annals of Glaciology*, Vol. 50, No. 50, 47-54.
- Schimel, A., 2012. *wgs2utm (version 2)*. Alexandre Schimel / Matlab Central.  
<http://www.mathworks.com/matlabcentral/fileexchange/14804-wgs2utm--version-2-/content/wgs2utm.m>
- Scholkmann, F., Spichtig, S., Muehleemann, T., Wolf, M., 2010. How to detect and reduce movement artifacts in near-infrared imaging using moving standard deviation and spline interpolation. *Physiological Measurement*, Vol. 31, No. 5, 649.
- Shepherd, A., Hubbard, A., Nienow, P., King, M., McMillan, M., Joughin, I., 2009. Greenland ice sheet motion coupled with daily melting in late summer. *Geophysical Research Letters*, Vol. 36, No. 1,
- Snyder, J. P., 1987. *Map Projections - A Working Manual*. U.S. Geological Survey professional paper 1395. U.S. Government Printing Office. 385 pp.
- Sugiyama, S., Bauder, A., Huss, M., Riesen, P., Funk, M., 2008. Triggering and drainage mechanisms of the 2004 glacier - dammed lake outburst in Gornergletscher, Switzerland. *Journal of Geophysical Research: Earth Surface (2003 -2012)*, Vol. 113, No. F4,
- Sugiyama, S., Gudmundsson, G. H., 2003. Diurnal variations in vertical strain observed in a temperate valley glacier. *Geophysical Research Letters*, Vol. 30, No. 2, n/a-n/a. doi: 10.1029/2002GL016160.
- Svendsen, H., Beszczynska-Møller, A., Hagen, J. O., Lefauconnier, B., Tverberg, V., Gerland, S., Ørbæk, J. B., Bischof, K., Papucci, C., Zajaczkowski, M., Azzolini, R., Bruland, O., Wiencke, C., Winther, J.-G., Dallmann, W., 2002. The physical environment of Kongsfjorden–Krossfjorden, an Arctic fjord system in Svalbard. *Polar Research*, Vol. 21, No. 1, 133-166. doi: 10.1111/j.1751-8369.2002.tb00072.x.
- Takasu, T., 2013. RTKLIB ver. 2.4.2 Manual. 2013 ed. *Tokyo University of Marine Science and Technology*. Available at [http://www.rtklib.com/prog/manual\\_2.4.2.pdf](http://www.rtklib.com/prog/manual_2.4.2.pdf)
- Van Pelt, W., Kohler, J., 2015. Modelling the long-term mass balance and firn evolution of glaciers around Kongsfjorden, Svalbard. *Journal of Glaciology*, Vol. 61, No. 228, 731-744. doi: 10.3189/2015JoG14J223.
- Walder, J., Hallet, B., 1979. Geometry of former subglacial water channels and cavities. *Journal of Glaciology*, Vol. 23, No. 89, 335-346.
- Williams, S. D. P., Bock, Y., Fang, P., Jamason, P., Nikolaidis, R. M., Prawirodirdjo, L., Miller, M., Johnson, D. J., 2004. Error analysis of continuous GPS position time series. *Journal of Geophysical Research: Solid Earth*, Vol. 109, No. B3, n/a-n/a. doi: 10.1029/2003JB002741.
- Willis, I. C., 1995. Intra-annual variations in glacier motion: a review. *Progress in Physical Geography*, Vol. 19, No. 1, 61-106. doi: 10.1177/030913339501900104.
- Yr, 2012. *Polar nights and midnight sun*. Yr. Available at <http://om.yr.no/about/midnight-sun/> (Visited 27.10.2015).
- Zwally, H. J., Abdalati, W., Herring, T., Larson, K., Saba, J., Steffen, K., 2002. Surface Melt-Induced Acceleration of Greenland Ice-Sheet Flow. *Science*, Vol. 297, No. 5579, 218-222. doi: 10.1126/science.1072708.

## 9 Appendices

### 9.1 Runoff calculation

The output from the surface mass balance model gives the runoff in a  $100 \text{ m} \times 100 \text{ m}$  grid covering the entire glacier, with a pixel unit of  $\text{m w.e. m}^{-2} 3\text{h}^{-1}$ . After defining the area (i.e. the pixels) over which the runoff is to be calculated, the total runoff for this respective area was calculated by

$$\bar{Q} = \frac{1}{n} \times \sum_{i=1}^n r_i \text{ [m w.e. m}^{-2} 3\text{h}^{-1}] \text{ or [m}^3 \text{ w.e. 3h}^{-1}]$$

$$a_{tot} = n \times a_{pix} \text{ [m}^2]$$

$$Q = \bar{Q} \times a_{tot} \times \frac{10^{-9} \text{ km}^3}{1 \text{ m}^3} \text{ [km}^3 \text{ w.e. 3h}^{-1}]$$

representing the total runoff ( $Q$ ), the mean runoff for each pixel ( $\bar{Q}$ ), the number of pixels ( $n$ ) with a runoff value, runoff value for each pixel ( $r_i$ ) with a unit  $\text{m w.e. m}^{-2} 3\text{h}^{-1}$ , area of each pixel ( $a_{pix}$ ) and the entire area ( $a_{tot}$ ) in  $\text{m}^2$ .

### 9.2 Coordinate of HAGN base station with static processing

ITRF08 Epoch	Cartesian coordinate [m]			Standard deviations [m]			Velocity [m/year]			
	doy 2015	x	y	z	$\sigma_x$	$\sigma_y$	$\sigma_z$	$v_x$	$v_y$	$v_z$
NYA1	202	1202433.6930	252632.3680	6237772.7070	0.0010	0.0010	0.0010	-0.0143	0.0075	0.0110

Gamit doy 2015	Baseline vector HAGN-NYA1 [m]				Sigma [m]				Coordinate HAGN relative to NYA1 [m]		
	$\Delta x$	$\Delta y$	$\Delta z$	length	$\sigma_{\Delta x}$	$\sigma_{\Delta y}$	$\sigma_{\Delta z}$	$\sigma_{\text{length}}$	x	y	z
195	-8167.8933	-29128.7180	2336.4949	30342.3120	0.0014	0.0012	0.0075	0.0012	1210601.5863	281761.0860	6235436.2121
196	-8167.8966	-29128.7178	2336.4873	30342.3121	0.0021	0.0016	0.0100	0.0017	1210601.5896	281761.0858	6235436.2198
197	-8167.8912	-29128.7168	2336.5166	30342.3120	0.0022	0.0017	0.0105	0.0018	1210601.5842	281761.0848	6235436.1904
198	-8167.8973	-29128.7166	2336.4837	30342.3109	0.0022	0.0018	0.0109	0.0019	1210601.5903	281761.0846	6235436.2233
199	-8167.8937	-29128.7168	2336.5040	30342.3117	0.0022	0.0017	0.0105	0.0018	1210601.5867	281761.0848	6235436.2030
200	-8167.8962	-29128.7174	2336.4861	30342.3115	0.0021	0.0017	0.0101	0.0018	1210601.5892	281761.0854	6235436.2209
201	-8167.8948	-29128.7184	2336.4893	30342.3124	0.0021	0.0017	0.0106	0.0018	1210601.5878	281761.0864	6235436.2177
202	-8167.8961	-29128.7180	2336.4888	30342.3123	0.0021	0.0017	0.0102	0.0018	1210601.5891	281761.0860	6235436.2182
203	-8167.8970	-29128.7177	2336.4884	30342.3122	0.0020	0.0017	0.0095	0.0017	1210601.5900	281761.0857	6235436.2186
204	-8167.8994	-29128.7157	2336.4888	30342.3111	0.0020	0.0017	0.0101	0.0018	1210601.5924	281761.0837	6235436.2182
205	-8167.8980	-29128.7163	2336.4858	30342.3110	0.0023	0.0018	0.0105	0.0018	1210601.5910	281761.0843	6235436.2212
206	-8167.8979	-29128.7165	2336.4861	30342.3112	0.0014	0.0013	0.0071	0.0013	1210601.5909	281761.0845	6235436.2209
207	-8167.8996	-29128.7175	2336.4874	30342.3127	0.0016	0.0012	0.0074	0.0013	1210601.5926	281761.0855	6235436.2196
208	-8167.8979	-29128.7173	2336.4878	30342.3121	0.0017	0.0012	0.0071	0.0013	1210601.5909	281761.0853	6235436.2193
Average	-8167.8963	-29128.7172	2336.4910	30342.3118	0.0020	0.0016	0.0094	0.0016	1210601.5893	281761.0852	6235436.2160
Std.dev	0.0023	0.0007	0.0086	0.0006					0.0023	0.0007	0.0086

### 9.3 Kinematic field survey

The kinematic survey was conducted during the fieldwork in spring 2015. A GNSS antenna was mounted on the sledge behind a snowmobile, and the snow surface up-glacier and down-glacier of HDF1, HDF2 and HD3 was surveyed (Figure 9.1). By using two separate snowmobiles with the same setup, a dense grid of measurements was achieved. In order to get the actual glacier ice surface, the snow depths were measured at 25-m intervals along the flow line, in addition to lateral measurements (Figure 9.2). The data have not been included in this study, but can be implemented in future work.

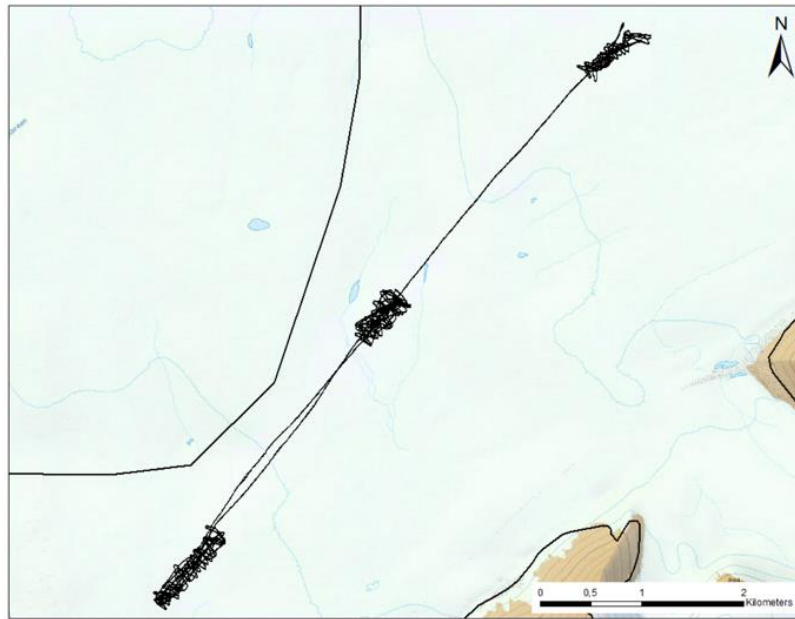


Figure 9.1. Horizontal track of the kinematic field survey. Basemap from NPI (2015).

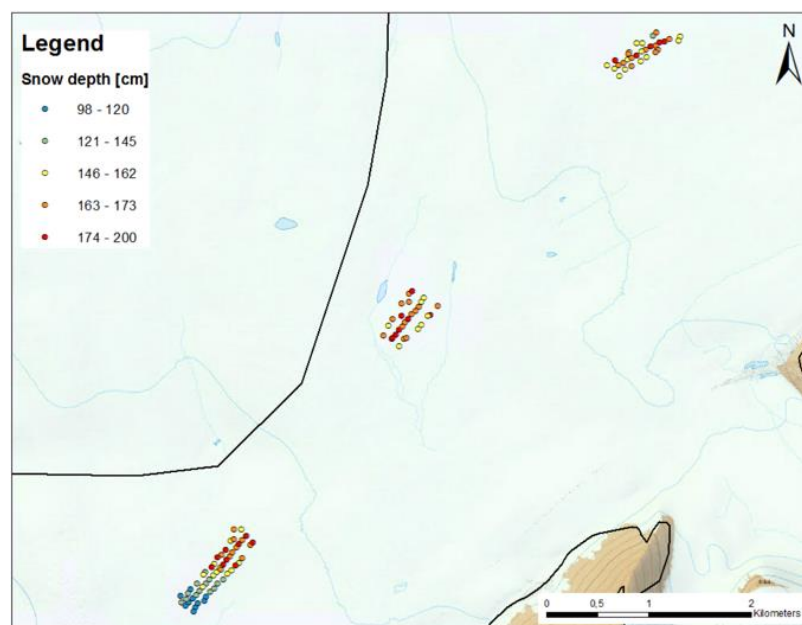


Figure 9.2. Snow depth measurements above and below all three stakes. Basemap from NPI (2015).